Advances in Water Resources 206 (2025) 105099

Contents lists available at ScienceDirect

Advances in Water Resources

journal homepage: www.elsevier.com/locate/advwatres

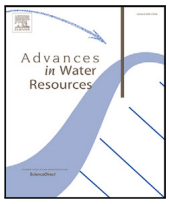

# Semi-analytical solutions for nonequilibrium transport and transformation of PFAS and other solutes in heterogeneous vadose zones with structured porous media

Sidian Chen [a,b], Bo Guo [a,*]

[a] Department of Hydrology & Atmospheric Sciences, University of Arizona, Tucson, AZ, USA
[b] Department of Energy Science & Engineering, Stanford University, Stanford, CA, USA

ARTICLE INFO

*Keywords:*
Perfluoroalkyl acids (PFAAs) and precursors
Heterogeneity
Rate-limited adsorption
Transformation
Experimental validation
Soil screening

ABSTRACT

We present screening-type semi-analytical models for quantifying the fate and transport of PFAS, including perfluoroalkyl acids (PFAAs) and their precursors (i.e., polyfluoroalkyl substances that can transform to PFAAs), in a heterogeneous vadose zone. The models employ one-dimensional multi-continuum representations with varying complexities (dual-porosity, dual-permeability, or triple-porosity). They account for PFAS-specific transport processes, including multi-site rate-limited adsorption at solid–water and air–water interfaces, and first-order biochemical transformation. Assuming steady-state infiltration, we derive semi-analytical solutions for all models under arbitrary initial and boundary conditions. We validate these new solutions using literature experimental breakthrough curves of PFAS and other solutes for various soils and wetting conditions. Furthermore, we demonstrate the models' capability by analyzing the long-term leaching and mass discharge of two example PFAS (PFOS and a precursor PFOSB) in a heterogeneous vadose zone beneath a model PFAS-contaminated site. The results demonstrate that the precursor undergoes significant transformation and adds additional PFOS mass discharge to groundwater. Additionally, the simulations suggest that, due to strong retention in the vadose zone (i.e., large residence time), the PFAS in the high- and low-conductivity transport pathways can be considered as in equilibrium. Taking advantage of this result, we illustrate that the multi-continuum models may be simplified to an effective single-porosity model for simulating the transport of longer-chain PFAS in a heterogeneous vadose zone. Overall, the semi-analytical models provide practical tools for assessing long-term fate and transport of PFAS in the vadose zone and mass discharge to groundwater in the presence of precursor transformations.

## 1. Introduction

Per- and poly-fluoroalkyl substances (PFAS)—including both perfluoroalkyl acids (PFAAs) and precursors (i.e., polyfluoroalkyl substances that can transform to PFAAs)—are emerging contaminants that have accumulated significantly in the vadose zone at contaminated sites, posing long-term threats to soil health and groundwater quality (e.g., Anderson et al., 2019; Brusseau et al., 2020). Characterizing and quantifying PFAS fate and transport in the vadose zone are particularly challenging due to their surfactant-like interfacially-active properties. After entering the vadose zone, PFAS accumulate at air–water interfaces in the unsaturated soil pore spaces (e.g., Lyu et al., 2018; Costanza et al., 2019). They can also adsorb on solid surfaces by hydrophobic and electrochemical interactions (e.g., Higgins and Luthy, 2006; Wei et al., 2017; Van Glubt et al., 2021). Some PFAS may be volatilized, taken by plant roots, or transformed by biochemical reactions (Choi et al., 2022; Dong et al., 2023; Brusseau and Guo, 2024). These processes may be heterogeneous and rate-limited (e.g., Chen and Guo, 2023; Stults et al., 2024a,b), leading to significant retention and nonequilibrium transport phenomena of PFAS in the vadose zone. Representing these PFAS-specific transport processes in the vadose zone is critical for assessing contamination risks and developing effective remediation strategies.

Additionally, the transport and leaching of PFAS are strongly influenced by preferential flow pathways generated by physical heterogeneities of structured porous media (i.e., macropores, fractures, and soil aggregates) in the vadose zone (e.g., Zeng and Guo, 2021, 2023). Characterization and modeling of preferential flow and non-PFAS solute transport in structured porous media have been extensively studied for several decades (e.g., Clay and Stott, 1973; Rao et al., 1974; Beven and Germann, 1982; Flury et al., 1994; Flury, 1996; Leij et al.,

* Corresponding author.
*E-mail address:* boguo@arizona.edu (B. Guo).

https://doi.org/10.1016/j.advwatres.2025.105099
Received 25 April 2025; Received in revised form 6 August 2025; Accepted 27 August 2025
Available online 12 September 2025

2012; Sharma et al., 2021). A series of dual-continuum model formulations in the forms of dual-porosity or dual-permeability models have been developed, parameterized, and tested against laboratory and field observations (e.g., Skopp et al., 1981; Gerke and van Genuchten, 1993; Pot et al., 2005; Gärdenäs et al., 2006). While advanced numerical models that account for a range of PFAS-specific transport mechanisms have been developed (e.g., Guo et al., 2020; Silva et al., 2020; Zeng and Guo, 2021; Zeng et al., 2021; Wallis et al., 2022; Zeng and Guo, 2023), none have represented preferential flow and transport in dual-continuum formulations. Zeng and Guo (2021, 2023) examined the impact of preferential flow and heterogeneity on PFAS transport in the vadose zone, where the heterogeneity was explicitly represented in a single-continuum formulation using a multi-dimensional model.

Compared to advanced numerical models, simpler analytical or semi-analytical models are often preferable for practical applications such as screen-type analysis (e.g., contamination site characterization, risk assessment, design of remedial actions, sensitivity analysis, and uncertainty quantification). To date, numerous analytical/semi-analytical models have been developed for the nonequilibrium transport of sorbing and reactive non-PFAS solutes in porous media (e.g., Lindstorm and Narasimham, 1973; Toride et al., 1993; Chen et al., 2019; Sharma et al., 2021). Most studies coupled one-site or two-site kinetic models for the rate-limited adsorption at solid–water interfaces and biochemical transformation processes with advection–dispersion-type models for the physical transport processes. These include single-porosity models that represent the solute transport in a single mobile domain (e.g., Lindstorm and Narasimham, 1973), dual-porosity models that represent the solute transport in a mobile domain and an immobile domain (e.g., Toride et al., 1993), and triple-porosity models that represent solute transport in a fast mobile domain, a slow mobile domain, and an immobile domain (e.g., Sharma et al., 2021).

Few analytical/semi-analytical models account for PFAS-specific transport processes in the vadose zone. Guo et al. (2022) developed an analytical model for PFAS transport in homogeneous vadose zones assuming instantaneous air–water interfacial adsorption and two-site rate-limited solid–water interfacial adsorption (referred to as "solid-phase adsorption" hereafter). Precursor transformation processes were not considered. The analytical model was later coupled with a groundwater dilution model to derive soil screening levels for PFAS-contaminated sites (Smith et al., 2024; Ma et al., 2025). In the present study, we develop a comprehensive set of models that incorporate multi-site rate-limited solid-phase and air–water interfacial adsorption, and first-order transformation in multi-continuum modeling frameworks including dual-porosity, dual-permeability, and triple-porosity representations. We derive semi-analytical solutions for all the new models and evaluate them for various solutes, soil types, soil heterogeneity, and wetting conditions using experimentally measured breakthrough curves. We then apply the semi-analytical solutions to simulate the retention and leaching of PFAS at a model heterogeneous contaminated site and discuss strategies to select the appropriate level of model complexity for a given contaminated site. To our knowledge, these multi-continuum models and the semi-analytical solutions are the first that account for multi-site rate-limited interfacial adsorption and first-order transformation processes in dual-porosity, dual-permeability, and triple-porosity formalisms.

## 2. Conceptual and mathematical models

We develop the conceptual representations for the nonequilibrium transport of PFAS in a heterogeneous vadose zone that consists of structured porous media. Following that, we present the mathematical models and derive the semi-analytical solutions for the models, including dual-porosity, dual-permeability, and triple-porosity formulations that couple multi-site rate-limited interfacial adsorption and first-order transformation.

### 2.1. Conceptual model

We consider a heterogeneous vadose zone containing structured soils (see Fig. 1a). As discussed in Section 1, structured soils contain high-conductivity channels (e.g., macropores and fractures) and soil aggregates. When infiltration occurs, water may rapidly travel through high-conductivity channels and, in the meantime, gradually enter soil aggregates. Water in the soil aggregates may exchange mass with the high-conductivity channels and/or directly flow from one aggregate to another. A portion of the water in the soil aggregates may be trapped (e.g., in small and/or dead-end pores) and become stagnant. PFAS dissolved in water can be transported via advection and dispersion along the high-conductivity channels and soil aggregates, as well as between them. PFAS dissolved in the stagnant water in the soil aggregates can exchange mass with the mobile water in the soil aggregates via molecular diffusion.

We assume that the structured soils are uniformly distributed across the vadose zone, and represent the vadose zone by a one-dimensional continuum with two overlapping domains (see Fig. 1b), following the classic dual-continuum conceptualization (e.g., Skopp et al., 1981). One domain represents high-conductivity channels (referred to as "fracture domain" hereafter), while the other represents soil aggregates (referred to as "matrix domain" hereafter). The matrix domain is further divided into two overlapping domains—a "mobile" domain containing only flowing water and an "immobile" domain containing only stagnant water. Additionally, we assume no direct mass exchange between the fracture and immobile matrix domains, i.e., the mass transfer with the fracture domain can only occur through the mobile matrix domain. The above conceptualization leads to the so-called "triple-porosity" (fracture, mobile matrix, and immobile matrix) model (e.g., Pot et al., 2005). Here, we generalize the "triple-porosity" to represent water flow and PFAS-specific retention and transport mechanisms in the three domains of a heterogeneous vadose zone. In each domain, PFAS can be in the aqueous phase or adsorbed at solid–water and air–water interfaces. The adsorption and desorption can occur instantaneously or kinetically. PFAS in the aqueous phase may undergo biochemical transformation.

We also present conceptualizations that simplify from the triple-porosity representation under certain conditions following the multi-continuum modeling literature (e.g., van Genuchten and Wierenga, 1976; Gerke and van Genuchten, 1993). When pore spaces in the soil aggregates are all well-connected and no stagnant water is present, we remove the immobile matrix domain and obtain the so-called "dual-permeability" model (e.g., Barenblatt et al., 1960; Leij et al., 2012). Alternatively, when the water flow and PFAS advection and dispersion through the soil aggregates are negligible, we approximate the entire matrix as an immobile domain that can only exchange mass with the fracture domain via molecular diffusion, which leads to the so-called "dual-porosity" model (e.g., Warren and Root, 1963). Finally, if we further assume that the entire vadose zone is homogeneous, we obtain the simplest "single-porosity" (one domain) model representation.

The terminology for the multi-continuum models discussed varies in the literature. The triple-porosity model was sometimes referred to as "triple-porosity, dual-permeability" model (e.g., Bai et al., 1993) to indicate that water in the third continuum ("porosity") is immobile. Depending on the context, the dual-permeability model was also called "dual-porosity" model (e.g., Gerke and van Genuchten, 1993) or "dual-porosity, dual-permeability" model (e.g., Bai et al., 1993). The dual-porosity model was sometimes referred to as "mobile-immobile" model (e.g., van Genuchten and Wierenga, 1976; Šimůnek and van Genuchten, 2008) or "dual-porosity, single-permeability" model (e.g., Bai et al., 1993). In the present study, we adopt the terms "triple-porosity", "dual-permeability", and "dual-porosity" to be consistent with the terminology for the "single-porosity" model.

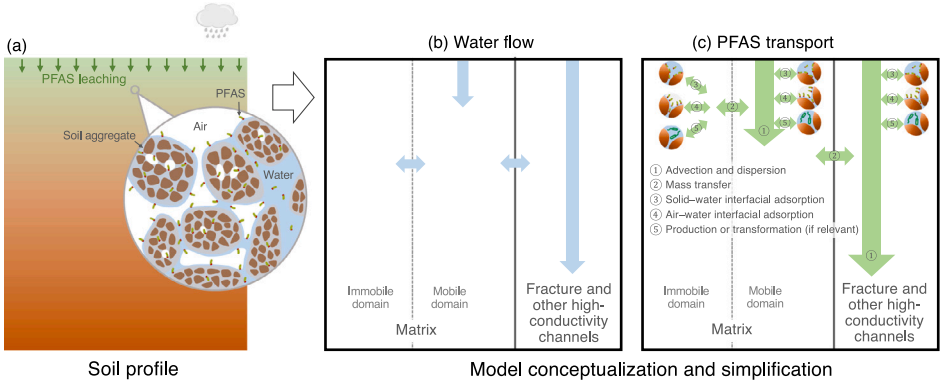


**Fig. 1.** (a) Schematic of PFAS migration in a heterogeneous vadose zone with structured soils, and the corresponding conceptual models for (b) water flow and (c) PFAS transport in the vadose zone. In the model conceptualization, the heterogeneous vadose zone is assumed to consist of three domains—a domain consisting of fractures and other high-conductivity channels, a soil matrix domain containing mobile water, and a soil matrix domain containing immobile water. The fractures and other high-conductivity channels, mobile matrix, and immobile matrix are each assumed a continuum throughout the vadose zone with distinct flow and transport mechanisms. When released to the vadose zone, PFAS can transport in domains with mobile water, diffuse in domains with immobile water, exchange mass between different domains, as well as kinetically adsorb at solid–water and air–water interfaces and biochemically transform in all domains.

### 2.2. Mathematical models

This section introduces the governing equations and initial and boundary conditions for all models. In each subsection, we start with the triple-porosity model. Following that, we simplify the triple-porosity formulations to obtain the dual-permeability, dual-porosity, and single-porosity formulations.

#### 2.2.1. Water flow

We assume one-dimensional steady-state gravity-driven (unit head gradient) infiltration along the vertical direction in the vadose zone and hydrodynamic equilibrium (i.e., equal hydraulic head) among the three domains (fracture, mobile matrix, and immobile matrix) at the same soil depth. Because the elevation head is the same across the three domains, their water pressure head is also equal. Under gravity-driven steady-state infiltration, the water pressure head is uniform across the soil depth. Denoting the bulk volume fraction of the three domains as $w_\mathrm{f}$, $w_\mathrm{m}$, and $w_\mathrm{im}$ (i.e., $w_\mathrm{f} + w_\mathrm{m} + w_\mathrm{im} = 1$), we obtain the following equations,

$$\begin{aligned} I_0 &= I_\mathrm{f} + I_\mathrm{m} = w_\mathrm{f} k_{r,\mathrm{f}}(\theta_\mathrm{f}) K_{sat,\mathrm{f}} + w_\mathrm{m} k_{r,\mathrm{m}}(\theta_\mathrm{m}) K_{sat,\mathrm{m}}, \\ h_\mathrm{f}(\theta_\mathrm{f}) &= h_\mathrm{m}(\theta_\mathrm{m}) = h_\mathrm{im}(\theta_\mathrm{im}), \end{aligned} \tag{1}$$

where the subscript "f", "m", and "im" denote the fracture, mobile matrix, and immobile matrix domains, respectively; $I_0$ is the total infiltration rate, and $I_\mathrm{f}$ and $I_\mathrm{m}$ are the infiltration rates in the fracture and mobile matrix domains, respectively; $k_{r,\mathrm{f}}$ and $k_{r,\mathrm{m}}$ are the relative permeability in the fracture and mobile matrix domains, respectively; $K_{sat,\mathrm{f}}$ and $K_{sat,\mathrm{m}}$ are the saturated hydraulic conductivity in the fracture and mobile matrix domains, respectively; $\theta$ and $h$ with the subscripts "f", "m", and "im" are the water content and water pressure head in the fracture, mobile matrix, and immobile matrix domains, respectively. The water pressure head and relative permeability can be computed as functions of the water content using the van Genuchten–Mualem model (Mualem, 1976; van Genuchten, 1980).

Eq. (1) describes steady-state water infiltration for the triple-porosity model. Steady-state water infiltration for the dual-permeability model can be obtained by setting $w_\mathrm{im} = 0$ (i.e., $w_\mathrm{f} + w_\mathrm{m} = 1$) and removing $h_\mathrm{im}(\theta_\mathrm{im})$. Removing $I_\mathrm{m}$ and $w_\mathrm{m} k_{r,\mathrm{m}}(\theta_\mathrm{m}) k_\mathrm{m}$ (i.e., $w_\mathrm{m} = 0$ and $w_\mathrm{f} + w_\mathrm{im} = 1$) and treating the water in the matrix domain as immobile gives the steady-state water infiltration for the dual-porosity model. Finally, the steady-state water infiltration for the single-porosity model (i.e., homogeneous vadose zone) is $I_0$ with a water content of $w_\mathrm{f}\theta_\mathrm{f} + w_\mathrm{m}\theta_\mathrm{m} + w_\mathrm{im}\theta_\mathrm{im}$.

#### 2.2.2. PFAS transport

PFAS, in addition to migrating by advection and dispersion in water, partition to the solid–water and air–water interfaces in each of the domains including fracture, mobile matrix, and immobile matrix domains. We represent the partitioning to solid–water and air–water interfaces by linear multi-site kinetic models. The solid–water and air–water interfaces are divided into multiple parts ("sites") and PFAS partition at each site with a different kinetic rate. Additionally, we represent the precursor transformation by a first-order kinetic model.

We formulate the governing equations for the transport of a PFAS, which can be a PFAA or a precursor. The equations for a PFAA and a precursor are almost identical except for the terms related to transformation. Transformation adds PFAA to the system as a product (i.e., source term) while it removes precursor from the system as a reactant (i.e., sink term). Below, we present the general equations that apply to either a PFAA or a precursor. Any terms that are specific to the PFAA or precursor will be stated explicitly.

Assuming the fracture domain contains $N_\mathrm{f}^\mathrm{sw}$ rate-limited solid-phase adsorption sites and $N_\mathrm{f}^\mathrm{aw}$ rate-limited air–water interfacial adsorption sites, the governing equation for the transport of a PFAA or precursor in the fracture domain can be written as

$$\begin{aligned} \theta_\mathrm{f} R_\mathrm{f} \frac{\partial c_\mathrm{f}}{\partial t} + \theta_\mathrm{f} v_\mathrm{f} \frac{\partial c_\mathrm{f}}{\partial z} - \theta_\mathrm{f} D_\mathrm{f} \frac{\partial^2 c_\mathrm{f}}{\partial z^2} \pm \mu_\mathrm{f} \theta_\mathrm{f} c_{\mathrm{p,f}} + \frac{w_\mathrm{m}}{w_\mathrm{f}} \kappa_{\mathrm{f,m}} \left(c_\mathrm{f} - c_\mathrm{m}\right) \\ + \sum_{i=1}^{N_\mathrm{f}^\mathrm{sw}} \rho_\mathrm{f} \frac{\partial c_{\mathrm{f},i}^\mathrm{sw}}{\partial t} + \sum_{i=1}^{N_\mathrm{f}^\mathrm{aw}} A_\mathrm{f}^\mathrm{aw} \frac{\partial c_{\mathrm{f},i}^\mathrm{aw}}{\partial t} = 0, \end{aligned} \tag{2}$$

where $c_\mathrm{f}$ is the aqueous PFAS concentration; $R_\mathrm{f}$ is the retardation factor and $R_\mathrm{f} = 1 + \left(F_\mathrm{f,eq}^\mathrm{sw} K_\mathrm{f}^\mathrm{sw} \rho_\mathrm{f} + F_\mathrm{f,eq}^\mathrm{aw} K_\mathrm{f}^\mathrm{aw} A_\mathrm{f}^\mathrm{aw}\right)/\theta_\mathrm{f}$, where $F_\mathrm{f,eq}^\mathrm{sw}$ is the fraction of the instantaneous solid-phase adsorption sites, $F_\mathrm{f,eq}^\mathrm{aw}$ is the fraction of the instantaneous air–water interfacial adsorption sites, $K_\mathrm{f}^\mathrm{sw}$ and $K_\mathrm{f}^\mathrm{aw}$ are respectively the solid-phase and air–water interfacial adsorption coefficients, $\rho_\mathrm{f}$ is the soil bulk density, and $A_\mathrm{f}^\mathrm{aw}$ is the specific area of air–water interfaces in the fracture domain; $v_\mathrm{f}$ is the porewater velocity; $D_\mathrm{f} = v_\mathrm{f}\alpha_{\mathrm{L,f}} + \tau_\mathrm{f} D_0$ is the dispersion coefficient, where $\alpha_{\mathrm{L,f}}$ is the longitudinal dispersivity, $\tau_\mathrm{f}$ is the tortuosity which can be approximated as $\tau_\mathrm{f} = \theta_\mathrm{f}^{7/3}/\theta_{s,\mathrm{f}}^2$ where $\theta_{s,\mathrm{f}}$ is the saturated water content (Millington and Quirk, 1961), and $D_0$ is the molecular diffusion coefficient in free water; $c_{\mathrm{p,f}}$ is the aqueous concentration of the precursor; $\mu_\mathrm{f}$ is the transformation rate constant; $\kappa_{\mathrm{f,m}}$ is the rate constant for the mass transfer between fracture and mobile matrix domains; $c_{\mathrm{f},i}^\mathrm{sw}$ is the PFAS concentration in the $i^\mathrm{th}$ ($i = 1, 2, \ldots, N_\mathrm{f}^\mathrm{sw}$) rate-limited solid-phase adsorption site; and $c_{\mathrm{f},i}^\mathrm{aw}$ is the PFAS concentration in the $i^\mathrm{th}$ ($i = 1, 2, \ldots, N_\mathrm{f}^\mathrm{aw}$) rate-limited air–water interfacial adsorption site.

Eq. (2) applies to either a PFAA or a precursor. For a PFAA, the sign of the transformation term ($\mu_f\theta_f c_{p,f}$) is negative and $c_{p,f}$ is an unknown variable that needs to be obtained from solving the transport equation for the corresponding precursor. If Eq. (2) is applied to a PFAA that is the transformation product of multiple precursors, a transformation term needs to be included for each precursor. For a PFAA with no sources from precursor transformation, the transformation term is removed. Conversely, the sign of the transformation term ($\mu_f\theta_f c_{p,f}$) is positive for a precursor and, in this case, $c_{p,f} = c_f$. The resulting equation directly applies to a precursor that serves as the reactant of a one-step transformation as well as the first-step reaction of a multi-step transformation. If a precursor is an intermediate product of a multi-step transformation, an additional transformation term must be added to account for the mass generated by that transformation step. Furthermore, all precursors involved in the multi-step transformation should be explicitly modeled. Example governing equations for multi-step transformation and multi-species transport processes can be found in the literature for non-PFAS solute transport in a single-porosity domain (e.g., Chen et al., 2019; Nguyen et al., 2024; Ho et al., 2024).

$A_f^{aw}$ in Eq. (2) can be a critical parameter due to the significant impact of air–water interfacial adsorption on PFAS transport (e.g., Guo et al., 2020). $A_f^{aw}$ may be obtained by different experimental methods, including direct micro-CT imaging (e.g., Culligan et al., 2004; Brusseau et al., 2007) and indirect measurements by interfacially-active tracers (e.g., Schaefer et al., 2000; Chen and Kibbey, 2006; Brusseau et al., 2015). If no measured data are available, an alternative is to estimate $A_f^{aw}$ using the thermodynamic-based method (Leverett, 1941; Morrow, 1970; Bradford and Leij, 1997). The thermodynamic-based method assumes that the mechanical work done for air–water displacement is fully converted to the interfacial energy for generating air–water interfaces. Based on this assumption, $A_f^{aw}$ may be estimated by computing the area under the soil–water characteristic curve as

$$A_f^{aw} = \frac{\phi_f}{\sigma}\int_{S_{w,f}}^{1} p_{c,f}(S'_{w,f})\,\mathrm{d}S'_{w,f}, \tag{3}$$

where $\phi_f$ is the porosity, $\sigma$ is the surface tension with no PFAS present, $p_{c,f}$ is the capillary pressure, $S_{w,f}$ is the water saturation, and $S'_{w,f}$ is a dummy variable.

Eq. (3) for the thermodynamic-based air–water interfacial area was derived based on the assumption of a quasi-static and reversible two-phase displacement process (Leverett, 1941; Morrow, 1970). It does not account for the impact of hysteretic phenomena—such as trapped and disconnected air bubbles in pore spaces (Reeves and Celia, 1996; Oostrom et al., 2001). It was also suggested that Eq. (3) may not represent the influence of microscale surface roughness on air–water interfaces associated with thin water films (Jiang et al., 2020a,b; Chen and Guo, 2023). To address this limitation, a scaling factor has been introduced to correct the thermodynamic-based specific air–water interfacial area computed by Eq. (3) (Zeng et al., 2021; Guo et al., 2022; Silva et al., 2022; Brusseau, 2023a).

Rate-limited solid-phase adsorption and air–water interfacial adsorption in the fracture domain are both described by a first-order kinetic model

$$\begin{aligned}\frac{\partial c_{f,i}^{sw}}{\partial t} &= \kappa_{f,i}^{sw}\left[f_{f,i}^{sw}(1-F_{f,eq}^{sw})K_f^{sw}c_f - c_{f,i}^{sw}\right],\\ \frac{\partial c_{f,i}^{aw}}{\partial t} &= \kappa_{f,i}^{aw}\left[f_{f,i}^{aw}\left(1-F_{f,eq}^{aw}\right)K_f^{aw}c_f - c_{f,i}^{aw}\right],\end{aligned} \tag{4}$$

where $\kappa_{f,i}^{sw}$ is the rate constant at the $i^{th}$ solid-phase adsorption site, $f_{f,i}^{sw}$ is the fraction of the $i^{th}$ solid-phase adsorption site with respect to all rate-limited sites (i.e., $\sum_{i=1}^{N_f^{sw}} f_{f,i}^{sw} = 1$ and $f_{f,i}^{sw}(1-F_{f,eq}^{sw})$ is the actual fraction with respect to all sites), $\kappa_{f,i}^{aw}$ is the rate constant at the $i^{th}$ air–water interfacial adsorption site, $f_{f,i}^{aw}$ is the fraction of the $i^{th}$ air–water interfacial adsorption site with respect to all rate-limited sites (i.e., $\sum_{i=1}^{N_f^{aw}} f_{f,i}^{aw} = 1$ and $f_{f,i}^{aw}(1-F_{f,eq}^{aw})$ is the actual fraction with respect to all sites). In general, the fractions of the solid-phase and air–water interfacial adsorption sites and the rate constants can be arbitrary. Determining these parameters (if arbitrary) can be challenging as it may require a large number of experimental measurements. One commonly used approach is to assume that $f$ and $\kappa$ (either $f_f^{sw}$ and $\kappa_f^{sw}$, or $f_f^{aw}$ and $\kappa_f^{aw}$) follow a log-normal distribution (Chen and Wagenet, 1995, 1997; Culver et al., 1997; Li and Brusseau, 2000), i.e., $f(\kappa) = \frac{1}{\sqrt{2\pi}\kappa\sigma_\kappa}\exp\left(-\frac{(\log(\kappa)-\bar{\kappa})^2}{2\sigma_\kappa^2}\right)$, where $\bar{\kappa}$ and $\sigma_\kappa$ are the mean and standard deviation of $\kappa$. Practically, it is often assumed that there is a finite number of rate-limited adsorption sites (either $N_f^{sw}$ or $N_f^{aw}$) and that each site is associated with a $\kappa$ spaced at equal intervals. We can then compute the fraction $f$ for each site. This leads to the so-called "multi-site" model that includes multiple adsorption sites (including rate-limited and instantaneous adsorption sites). When the number of rate-limited adsorption sites is 1 ($N_f^{sw} = 1$ or $N_f^{aw} = 1$), the multi-site model is reduced to a "two-site" model that includes one rate-limited adsorption site and one instantaneous adsorption site. The two-site model does not need a log-normal distribution. It only requires the total fraction of the rate-limited site and the rate constant of the rate-limited adsorption.

Similar equations can be written for PFAS transport in the mobile matrix domain with additional terms representing the mass exchange with the immobile matrix domain. The immobile matrix domain may contain soil aggregates of varying sizes that exchange mass with the mobile domain at different rates (i.e., different time scales), which we represent using a multi-domain model. Assuming that the immobile matrix domain consists of $N_{im}$ soil aggregates (referred to as "sub-domains" hereafter) and that the mobile matrix domain contains $N_m^{sw}$ rate-limited solid-phase adsorption sites and $N_m^{aw}$ rate-limited air–water interfacial adsorption sites, the governing equation for PFAS transport in the mobile matrix domain is given by

$$\begin{aligned}&\theta_m R_m\frac{\partial c_m}{\partial t} + \theta_m v_m\frac{\partial c_m}{\partial z} - \theta_m D_m\frac{\partial^2 c_m}{\partial z^2} \pm \mu_m\theta_m c_{p,m} - \kappa_{f,m}(c_f - c_m)\\ &+\sum_{i=1}^{N_m^{sw}}\rho_m\frac{\partial c_{m,i}^{sw}}{\partial t} + \sum_{i=1}^{N_m^{aw}}A_m^{aw}\frac{\partial c_{m,i}^{aw}}{\partial t} + \frac{w_{im}}{w_m}\sum_{i=1}^{N_{im}}w_{im,i}\kappa_{m,im,i}(c_m - c_{im,i}) = 0,\end{aligned} \tag{5}$$

where $\kappa_{m,im,i}$ is the rate constant for the mass transfer between the mobile matrix domain and the $i^{th}$ ($i = 1, 2, \ldots, N_{im}$) immobile subdomain, $c_{im,i}$ is the aqueous PFAS concentration in the $i^{th}$ ($i = 1, 2, \ldots, N_{im}$) immobile subdomain, $w_{im,i}$ is the fraction of the bulk volume of $i^{th}$ immobile matrix subdomain (i.e., $\sum_{i=1}^{N_{im}} w_{im,i} = 1$), and the remaining variables and parameters for the mobile matrix domain follow the same definitions as those in Eq. (2). The sign for the transformation term $\mu_m\theta_m c_{p,m}$ follows the same convention as that in Eq. (2) for a PFAA or a precursor, as discussed earlier.

Like that in the fracture domain, the rate-limited solid-phase adsorption and air–water interfacial adsorption in the mobile matrix domain are both described by a first-order kinetic model

$$\begin{aligned}\frac{\partial c_{m,i}^{sw}}{\partial t} &= \kappa_{m,i}^{sw}\left[f_{m,i}^{sw}(1-F_{m,eq}^{sw})K_m^{sw}c_m - c_{m,i}^{sw}\right],\\ \frac{\partial c_{m,i}^{aw}}{\partial t} &= \kappa_{m,i}^{aw}\left[f_{m,i}^{aw}(1-F_{m,eq}^{aw})K_m^{aw}c_m - c_{m,i}^{aw}\right],\end{aligned} \tag{6}$$

where the variables and parameters for the mobile matrix domain follow the same definitions as those in Eq. (4).

Finally, we present the governing equation for the PFAS in the $i^{th}$ ($i = 1, 2, \ldots, N_{im}$) immobile matrix subdomain. Assuming each $i^{th}$ subdomain contains one rate-limited solid-phase adsorption site and one rate-limited air–water interfacial adsorption site, we obtain

$$\begin{aligned}\theta_{im,i}R_{im,i}\frac{\partial c_{im,i}}{\partial t} &\pm \mu_{im,i}\theta_{im,i}c_{p,im,i} - \kappa_{m,im,i}(c_m - c_{im,i})\\ &+\rho_{im}\frac{\partial c_{im,i}^{sw}}{\partial t} + A_{im}^{aw}\frac{\partial c_{im,i}^{aw}}{\partial t} = 0,\end{aligned} \tag{7}$$

where $R_{im,i}$ is the retardation factor in the $i^{th}$ immobile matrix subdomain and $R_{im,i} = 1 + \left(F_{im,eq,i}^{sw}K_{im}^{sw}\rho_{im} + F_{im,eq,i}^{aw}K_{im}^{aw}A_{im}^{aw}\right)/\theta_{im,i}$, $F_{im,eq,i}^{sw}$ is

the fraction of the instantaneous solid-phase adsorption site, $F^{aw}_{im,eq,i}$ is the fraction of the instantaneous air–water interfacial adsorption site, and the remaining variables and parameters (including the sign for the transformation term) follow the same definitions as those in Eq. (2) and Eq. (5).

The rate-limited solid-phase adsorption and air–water interfacial adsorption in the immobile matrix domain, following a first-order kinetic model, is given by

$$\begin{aligned}\frac{\partial c^{sw}_{im,i}}{\partial t} &= \kappa^{sw}_{im,i}\left[\left(1-F^{sw}_{im,eq,i}\right)K^{sw}_{im}c_{im,i}-c^{sw}_{im,i}\right],\\ \frac{\partial c^{aw}_{im,i}}{\partial t} &= \kappa^{aw}_{im,i}\left[(1-F^{aw}_{im,eq,i})K^{aw}_{im}c_{im,i}-c^{aw}_{im,i}\right].\end{aligned} \tag{8}$$

Eqs. (2)–(8) provide the one-dimensional governing equations for the triple-porosity model. These equations can be reduced to obtain the governing equations for the dual-permeability, dual-porosity, and single-porosity models. For example, removing the mobile-immobile mass-transfer term (i.e., $\frac{w_{im}}{w_m}\sum_{i=1}^{N_{im}} w_{im,i}\kappa_{m,im,i}(c_m - c_{im,i})$) in Eq. (5) and the governing equations for the immobile matrix subdomains (i.e., Eqs. (7)–(8)) leads to the dual-permeability model. The dual-porosity model can be recovered by removing Eqs. (5)–(6) and connecting the fracture domain with the immobile matrix domain (see the resulting equations in Appendix B). Finally, the single-porosity model is obtained from Eq. (2) by removing the fracture–matrix mass transfer term and replacing the variables and parameters with their domain-averaged quantities.

Initial and boundary conditions are required to solve the governing equations presented above, which are described in the following two sections, respectively.

#### 2.2.3. Initial conditions

We first present the initial conditions for the triple-porosity model, and then show how they can be reduced to obtain the initial conditions for the dual-permeability, dual-porosity, and single-porosity models. All equations apply to both a PFAA and a precursor, thus we do not explicitly differentiate them.

In the fracture domain of the triple-porosity model, the initial aqueous PFAS concentration can be written as

$$c_f(z,t=0) = c^0_f(z). \tag{9}$$

The initial PFAS concentrations in the rate-limited solid-phase and air–water interfacial adsorption sites are respectively given by

$$\begin{aligned}c^{sw}_{f,i}(z,t=0) &= c^{sw,0}_{f,i}(z), \quad i=1,2,\ldots,N^{sw}_f,\\ c^{aw}_{f,i}(z,t=0) &= c^{aw,0}_{f,i}(z), \quad i=1,2,\ldots,N^{aw}_f.\end{aligned} \tag{10}$$

Similarly, the initial aqueous PFAS concentration in the mobile matrix domain can be written as

$$c_m(z,t=0) = c^0_m(z). \tag{11}$$

The initial PFAS concentrations of the rate-limited solid-phase and air–water interfacial adsorption sites in the mobile matrix domain are respectively given by

$$\begin{aligned}c^{sw}_{m,i}(z,t=0) &= c^{sw,0}_{m,i}(z), \quad i=1,2,\ldots,N^{sw}_m,\\ c^{aw}_{m,i}(z,t=0) &= c^{aw,0}_{m,i}(z), \quad i=1,2,\ldots,N^{aw}_m.\end{aligned} \tag{12}$$

For the immobile matrix domain, the initial aqueous PFAS concentration in the $i^{th}$ subdomain can be written as

$$c_{im,i}(z,t=0) = c^0_{im,i}(z), \tag{13}$$

where $i = 1,2,\ldots,N_{im}$. The initial PFAS concentrations of the rate-limited solid-phase and air–water interfacial adsorption sites in the immobile matrix domain are respectively given by

$$\begin{aligned}c^{sw}_{im,i}(z,t=0) &= c^{sw,0}_{im,i}(z),\\ c^{aw}_{im,i}(z,t=0) &= c^{aw,0}_{im,i}(z),\end{aligned} \tag{14}$$

where $i = 1,2,\ldots,N_{im}$.

Eqs. (9)–(14) provide all required initial conditions for solving the triple-porosity model. The initial conditions for the dual-permeability model are given by Eqs. (9)–(12), while those for the dual-porosity model are given by Eqs. (9)–(10) and Eqs. (13)–(14). For the single-porosity model, the initial conditions are given by the aqueous concentration, solid-phase adsorption, and air–water interfacial adsorption averaged across all three domains (fracture, mobile matrix, and immobile matrix domains).

The initial conditions presented above can be any arbitrary functions in space. Note that the initial PFAS concentrations in different domains and adsorption sites may be related to each other under certain conditions (e.g., under equilibrium conditions).

#### 2.2.4. Boundary conditions

Similar to Section 2.2.3, we present the boundary conditions for the triple-porosity model, and then introduce how they can be reduced to obtain the boundary conditions for the dual-permeability, dual-porosity, and single-porosity models. All equations apply to both a PFAA and a precursor.

We employ a flux-based aqueous concentration condition for the top boundary and a zero aqueous concentration gradient condition at the bottom boundary for both the fracture and mobile matrix domains. Assuming semi-infinite domains, we obtain

$$\left[-D_f\frac{\partial c_f}{\partial z}+v_f c_f\right]_{z=0} = v_f c_{f,in}(t), \quad \& \quad \left[\frac{\partial c_f}{\partial z}\right]_{z=\infty} = 0, \tag{15}$$

and

$$\left[-D_m\frac{\partial c_m}{\partial z}+v_m c_m\right]_{z=0} = v_m c_{m,in}(t), \quad \& \quad \left[\frac{\partial c_m}{\partial z}\right]_{z=\infty} = 0, \tag{16}$$

where $c_{f,in}(t)$ and $c_{m,in}(t)$ are the aqueous concentrations at the inlet ($z = 0$) of the fracture and mobile matrix domains at time $t$. No boundary conditions are needed for the immobile matrix domain.

The boundary conditions for the dual-permeability model are the same as the triple-porosity model (i.e., Eqs. (15)–(16)). For the dual-porosity model, only Equation (15) is needed, which gives the boundary conditions for the fracture domain. The boundary conditions for the single-porosity model are given by the weighted average of Eqs. (15) and (16) using $w_f\theta_f$ and $w_m\theta_m$ as their weights, respectively.

### 2.3. Semi-analytical solutions

We solve the governing equations for all the models (Section 2.2.2) semi-analytically using Laplace transform and inverse Laplace transform subject to the initial conditions and boundary conditions (Sections 2.2.3–2.2.4). We summarize the key procedures below and present additional details in the appendices.

We first nondimensionalize the governing equations, initial conditions, and boundary conditions, and perform Laplace transforms both in time and in space. The equations in the Laplace domain are then solved algebraically. Following that, we perform inverse Laplace transforms in space (analytically) and in time (numerically) to obtain the physical solutions. The detailed derivations for the triple-porosity and dual-permeability models are provided in Appendix A, and those for the dual-porosity and single-porosity models are presented in Appendix B.

## 3. Model evaluation and validation

We use three sets of miscible displacement experiments (i.e., laboratory experiments in which water containing a dissolved solute is injected into a soil column under steady-state water flow conditions) from the literature to evaluate and validate the semi-analytical models. For each simulation, we also verify the semi-analytical models by comparing with their numerical solutions.

**Table 1**
Parameters for simulating the miscible displacement experiments with packed homogeneous soils under saturated and unsaturated conditions. Most parameters are collected from the literature (Brusseau et al., 2015, 2019) except for the solid-phase adsorption parameters, which are obtained by model calibration. The adsorption parameters are assumed to be the same under saturated and unsaturated conditions.

| Physical and transport parameters | | | |
|---|---|---|---|
| Parameter | Unit | Vinton | Eustis |
| $L$ | cm | 15 | 20 |
| $v$ | cm/hr | 30 | 30 |
| $\alpha_L$ | cm | 0.2 | 0.5 |
| $\phi$ | $cm^3/cm^3$ | 0.42 | 0.36 |
| $\rho$ | $g/cm^3$ | 1.51 | 1.69 |

| Solid-phase adsorption parameters | | | | | |
|---|---|---|---|---|---|
| Parameter | Unit | Vinton | | Eustis | |
| | | PFOS | SDBS | PFOS | SDBS |
| $K^{sw}$ | $cm^3/g$ | 0.54 | 0.60 | 0.76 | 1.3 |
| *Two-site model* | | | | | |
| $F^{sw}$ | – | 0.92 | 0.39 | 0.88 | 0.41 |
| $\kappa^{sw}$ | $hr^{-1}$ | 0.70 | 1.66 | 1.2 | 0.54 |
| *Multi-site model* | | | | | |
| $F^{sw}$ | – | 0.97 | 0.19 | 0.88 | 0.41 |
| $\bar{\kappa}^{sw}$ | $hr^{-1}$ | 2.0 | 5.8 | 2.8 | 2.2 |
| $\sigma_{\kappa^{sw}}$ | $hr^{-1}$ | 1.8 | 19 | 3.6 | 4.8 |

### 3.1. Simulating miscible displacement experiments in saturated homogeneous soils

We first consider saturated miscible displacement experiments reported by Brusseau et al. (2019) for two interfacially-active solutes (PFOS (perfluorooctane sulfonic acid), and SDBS (sodium dodecylbenzene sulfonate)) conducted using packed homogeneous soil columns. The objective is to test the representation of multi-site rate-limited solid-phase adsorption (Brusseau et al., 2019) that was not included in the prior analytical models for PFAS transport (Guo et al., 2022).

In each experiment, a pulse injection of PFOS solution (10 mg/L) or SDBS solution (10 mg/L) is introduced at the inlet of the saturated soil column under steady-state flow. Breakthrough curves are constructed from a time series of aqueous concentrations at the outlet. Additional details of the experimental setup and soil hydraulic parameters are presented in Table 1.

Because the packed soil column is homogeneous, we simulate the experiments using the single-porosity model. For comparison, the simulations apply both the two-site and multi-site models for solid-phase adsorption, which allows us to evaluate the importance of representing multi-site rate-limited solid-phase adsorption. The two-site model has two undetermined parameters: the fraction of the instantaneous site ($F^{sw}$), and the rate constant for kinetic adsorption ($\kappa^{sw}$). The multi-site model has four undetermined parameters: the fraction of the instantaneous site ($F^{sw}$), the number of rate-limited sites ($N^{sw}$), and the mean and standard deviation of the rate constant for kinetic adsorption ($\bar{\kappa}^{sw}$ and $\sigma_{\kappa^{sw}}$). We set $N^{sw} = 100$ for the multi-site model, because we find that a further increase of $N^{sw}$ does not notably improve the results, consistent with previous studies (Brusseau et al., 2019). We determine the unknown parameters for both models via calibration. The calibration uses the Nelder–Mead optimization algorithm (or downhill simplex method) to find parameters that minimize the root mean square error of log-scale aqueous concentrations, defined as $\mathrm{RMSE}_{\log} = \left(\frac{1}{n}\sum_{i=1}^{n}\left(\log c_{\mathrm{sim},i} - \log c_{\mathrm{obs},i}\right)^2\right)^{1/2}$ where $c_{\mathrm{sim},i}$ and $c_{\mathrm{obs},i}$ are the normalized simulated and observed aqueous concentrations and $n$ is the number of data points.

We summarize the calibrated parameters in Table 1, and present the simulated and measured breakthrough curves in Fig. 2. In all cases, the multi-site model presents better agreements with the measurements than the two-site model. The two-site model does not capture the long tailing at later times, whereas the multi-site model matches well with later-time aqueous concentrations. For Vinton and Eustis soils, $\mathrm{RMSE}_{\log}$ for PFOS decreases from 1.52 and 9.47 (two-site model) to 0.98 and 7.02 (multi-site model), respectively. For SDBS, $\mathrm{RMSE}_{\log}$ are reduced from 0.36 and 1.09 to 0.33 and 0.35 for the two soils when the multi-site model is used. The semi-analytical solutions are also verified by their numerical solutions obtained from solving the governing equations using a backward Euler finite difference method. As shown in Fig. 2, the two solutions overlap for all cases.

### 3.2. Simulating miscible displacement experiments in unsaturated homogeneous soils

Using the calibrated solid-phase adsorption parameters from the saturated experiments in Section 3.1, we simulate two miscible displacement experiments for SDBS in Vinton soil conducted under unsaturated conditions (Brusseau et al., 2015). An experiment with a water saturation of $S_w = 0.82$ is established by drainage and another with a water saturation of $S_w = 0.80$ is established by imbibition. We assume instantaneous air–water interfacial adsorption (Brusseau, 2020; Zeng et al., 2021) and collect air–water interfacial adsorption parameters $A^{aw}$ and $K^{aw}$ from literature (Brusseau et al., 2015). The $A^{aw}$ is determined by interfacial tracer experiments and the $K^{aw}$ is computed by the Langmuir isotherm from measured surface tension data for SBDS. The calculations yield $A^{aw} = 68\,cm^{-1}$ at $S_w = 0.82$ and $A^{aw} = 61\,cm^{-1}$ at $S_w = 0.80$, and $K^{aw} = 2.9 \times 10^{-3}$ cm.

The predicted and measured breakthrough curves are presented in Fig. 3. The analytical and numerical solutions overlap for all cases and both generally agree with the experimental data. The multi-site model provides better predictions of the breakthrough curves than the two-site model as expected from the comparisons in Section 3.1. The $\mathrm{RMSE}_{\log}$ for the multi-site model are 0.27~0.77 times smaller than that for the two-site model. While the multi-site model matches the $S_w = 0.82$ experiment well, it deviates slightly from the $S_w = 0.8$ experiment (Fig. 3b), e.g., the model prediction did not capture the long tail. Because the solid-phase adsorption is not expected to differ between the two experiments, the deviation might be caused by experimental variability (Guo et al., 2022). Because the model simulations are predictions with no parameter tuning, a good agreement between the simulations and experiments validates the multi-site model for representing rate-limited solid-phase adsorption in unsaturated miscible displacement experiments.

Furthermore, because the two-site model is identical to the analytical solution of Guo et al. (2022), the better match between the multi-site model and experimental data indicates that the multi-site model provides a more realistic representation of the actual physical processes occurring in the simulated experiments. This enhanced capability enables more accurate simulations and better quantitative analyses of PFAS transport behaviors in more complex porous media systems.

### 3.3. Simulating miscible displacement experiments in unsaturated heterogeneous soils

This section further evaluates the dual-porosity and dual-permeability models by simulating unsaturated miscible displacement experiments in heterogeneous soils. Because experiments for PFAS and hydrocarbon surfactants in heterogeneous porous media are limited and not well constrained (Hitzelberger et al., 2022; Liu et al., 2024), we focus on simulating miscible displacement experiments conducted for other interfacially-active solutes (Pot et al., 2005).

We simulate two sets of miscible displacement experiments. Each set consists of three independent experiments conducted in an undisturbed soil core sampled from a tile-drained agriculture field (Pot et al., 2005). For each independent experiment, a pulse of solute solution is injected at the inlet under steady-state unsaturated flow, and a time series of

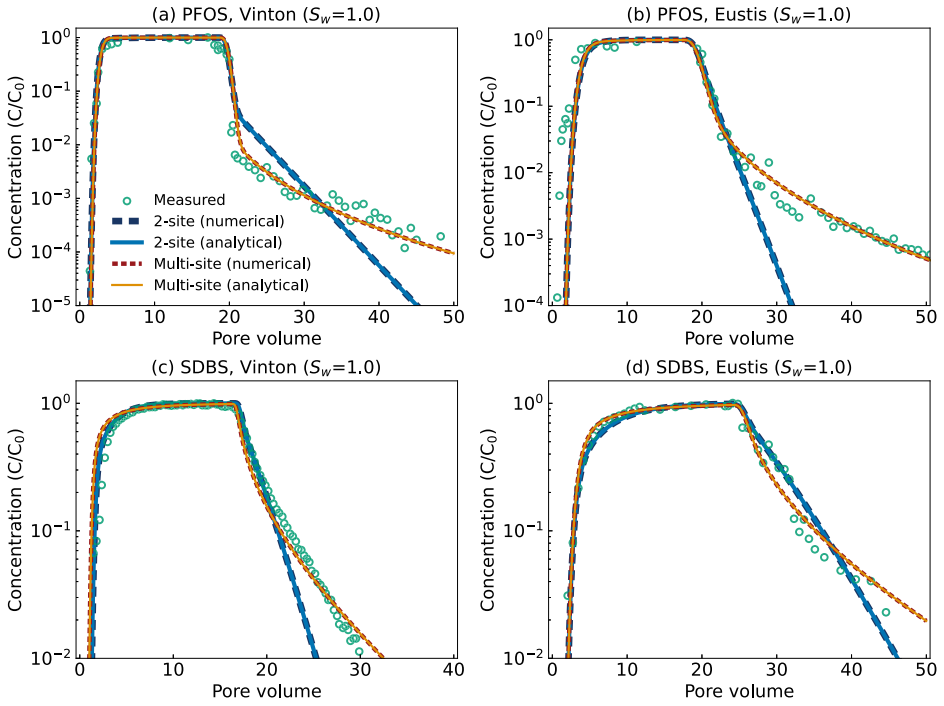


**Fig. 2.** Simulated vs. measured breakthrough curves for two interfacially active solutes (PFOS and SDBS) and two soil types (Vinton and Eustis) under saturated conditions. The simulations include numerical (dashed lines) and semi-analytical (solid lines) solutions of a single-porosity model with two-site and multi-site solid-phase adsorption. The measured data (circles, denoted as "Measured") are from Brusseau et al. (2019).

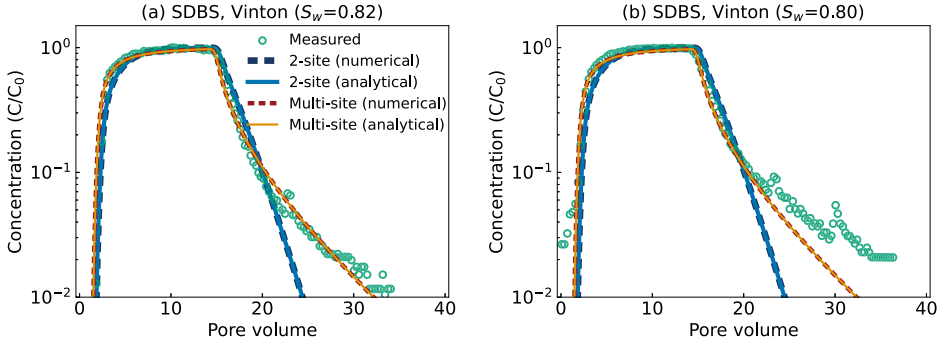


**Fig. 3.** Predicted vs. measured breakthrough curves for SDBS in Vinton soil under two unsaturated conditions: (a) $S_w = 0.82$ (established by drainage), and (b) $S_w = 0.80$ (established by imbibition). The simulations include numerical (dashed lines) and semi-analytical (solid lines) solutions of a single-porosity model with two-site and multi-site solid-phase adsorption. Adsorption at air–water interfaces is assumed to be in equilibrium. The measured data (circles, denoted as "Measured") are from Brusseau et al. (2015).

aqueous concentrations is measured at the outlet to construct a breakthrough curve. Three solutes are used, including bromide (a passive solute) and two herbicides (Isoproturon and Metribuzin). Isoproturon and Metribuzin both adsorb at solid–water interfaces and degrade in water (i.e., reactive tracer). The experimental parameters have been reported in Pot et al. (2005), which we summarize in Table 2.

We employ the dual-porosity and dual-permeability models with two-site kinetic solid-phase adsorption. Each simulation set begins by determining the flow and transport parameters for the fracture and matrix domains—including bulk volume fractions of fracture and matrix domains, water contents, infiltration rates, dispersivities, and fracture–matrix mass transfer rate constants. Because the fracture and matrix domains are not explicitly differentiated for intact soil cores, we calibrate the flow and transport parameters for the two domains using the breakthrough curves of the passive solute bromide (see Fig. 4a,d and Table 2). Then we use the herbicide breakthrough curves to estimate the parameters for solid-phase adsorption and transformation (see Table 3).

The comparisons between the simulated and measured breakthrough curves (see Fig. 4) suggest a better performance of the dual-permeability model than the dual-porosity model. The dual-permeability model captures the bimodal behavior of the breakthrough curves for the passive and reactive solutes in both soil cores. In contrast, the dual-porosity model fails to do so. As expected, the RMSE $= \left(\frac{1}{n}\sum_{i=1}^{n}\left(c_{\mathrm{sim},i} - c_{\mathrm{obs},i}\right)^2\right)^{1/2}$ for the dual-porosity model simulations (0.010~0.044) is greater than that for the dual-permeability model (0.006~0.019). Due to the relatively weak solid-phase adsorption (see Table 3), Isoproturon and Metribuzin do not exhibit significant retention. However, they undergo significant degradation. We quantify the degree of degradation using the ratio between the breakthrough mass and the total injected mass (i.e., $1-\int_0^\infty c_{z_1}(t)\,\mathrm{d}t / \int_0^\infty c_{z_0}(t)\,\mathrm{d}t$, where $c_{z_0}(t)$ and $c_{z_1}(t)$ are respectively the aqueous concentrations at the inlet and outlet at time $t$). The results suggest that 62% of the Isoproturon mass and 40% of the Metribuzin mass are degraded in soil core 1. Conversely, 28% of Isoproturon and 36% of Metribuzin in soil core 2 are degraded due to smaller degradation rates (see Table 3).

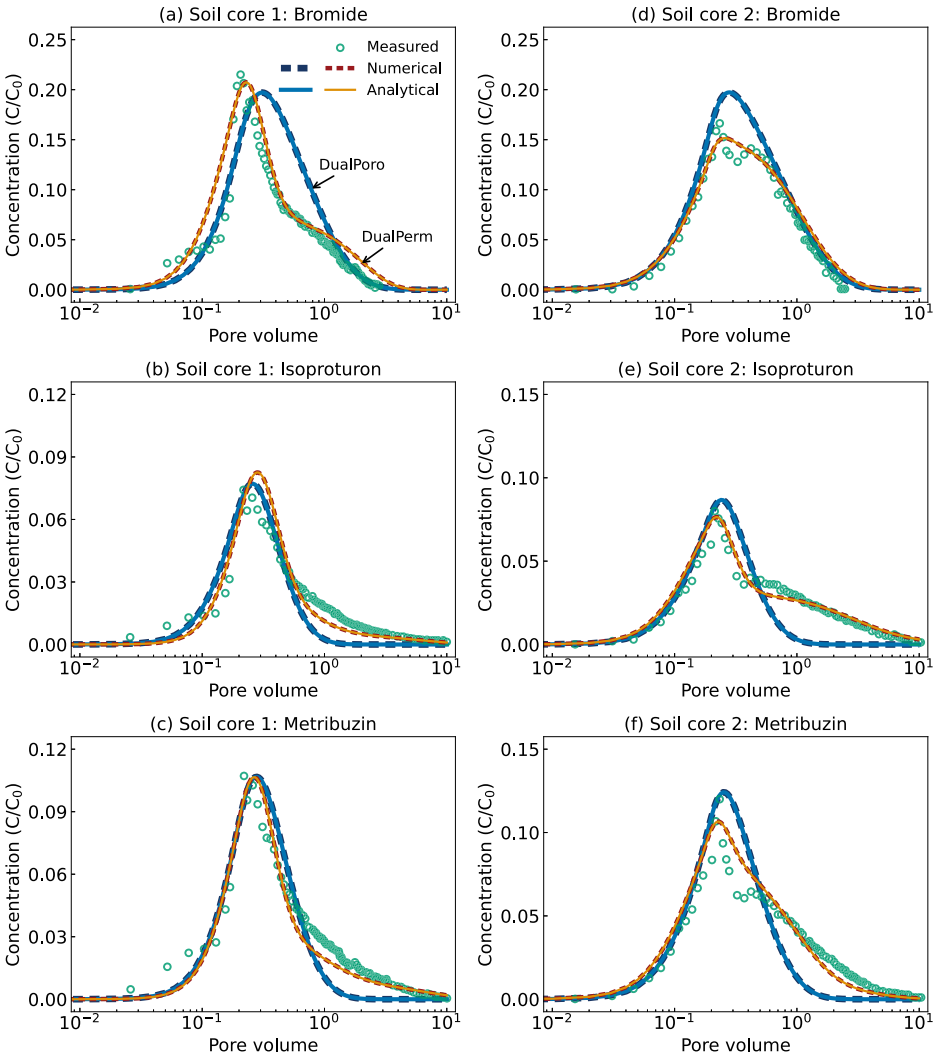


**Fig. 4.** Model evaluation in unsaturated heterogeneous soils by comparing breakthrough curves simulated by numerical (dashed lines) and semi-analytical (solid lines) solutions against those measured by Pot et al. (2005) (circles, denoted as "Measured"). We simulate three solutes—including one passive solute (bromide) and two reactive herbicides (Isoproturon and Metribuzin)—in two undisturbed soil cores using the dual-porosity model (denoted as "DualPoro") and dual-permeability model (denoted as "DualPerm").

## 4. Demonstration of model application

We present an example application to illustrate how the semi-analytical models can be used to quantify long-term PFAS leaching and transport in heterogeneous vadose zones at a model agricultural site impacted by the land application of PFAS-contaminated biosolids. We introduce below the details of the problem setup, simulation results, and analysis.

### 4.1. Problem setup

We consider a 4-meter deep vadose zone consisting of a uniform structured soil. We assume that PFAS-containing biosolids had been applied annually to the land for 30 years. Two example PFAS are considered in the biosolids: PFOS (a PFAS not known to degrade in the environment) and PFOSB (perfluorooctane sulfonate betaine, which is a precursor that may transform into PFOS). Because PFOS in the soil may be directly released from biosolids or produced from PFOSB transformation, we differentiate the two by referring to the former as "legacy" PFOS and the latter as "PFOSB-derived" PFOS. We consider an annual precipitation of 60 cm and an annual average irrigation of 45.72 cm (Smith et al., 2024). The precipitation and irrigation lead to a net infiltration rate of 9.144 cm. The soil hydraulic properties and PFAS transport parameters are presented in Table 4.

The initial concentration profile of PFAS at the site is generated by simulating PFAS contamination from 30 years of biosolids land application and the subsequent transport in the vadose zone using the dual-permeability model. Descriptions for how the initial concentration profile is generated are presented in Appendix D.1. We take the initial concentration profile and apply the dual-permeability model to simulate PFAS leaching in the vadose zone during post-contamination, i.e., no additional PFAS-containing biosolids are applied to the site. In addition to the base case simulation by the dual-permeability model, we also conduct simulations using the dual-porosity model and an effective single-porosity model. The dual-porosity model assumes that water is immobile in the matrix domain and PFAS therein can only transport downward by exchanging mass with the fracture domain. The effective single-porosity model is constructed by further simplifying the dual-porosity model assuming that the residence time for PFAS in the vadose zone is sufficiently long such that the fracture and matrix domains can be considered as in equilibrium. The governing equation for the effective single-porosity model is given by

$$R\frac{\partial c}{\partial t} + v\frac{\partial c}{\partial z} - D\frac{\partial^2 c}{\partial z^2} \pm \mu c_p = 0, \tag{17}$$

**Table 2**
Parameters for simulating breakthrough curves in heterogeneous soil cores under unsaturated conditions. The experimental data are obtained from Pot et al. (2005) and the parameters are determined by model calibration.

| Parameter | Unit | Soil core 1 | Soil core 2 |
|---|---|---|---|
| Experimental setup | | | |
| $L$ | cm | 30 | 30 |
| $\theta$ | $cm^3/cm^3$ | 0.398 | 0.375 |
| $I_0$ | cm/hr | 0.308 | 0.326 |
| Injection time | Pore volume | 0.1548 | 0.1741 |
| $\rho$ | $g/cm^3$ | 1.25 | 1.25 |
| Dual-porosity model | | | |
| *Fracture domain* | | | |
| $\theta_f$ | $cm^3/cm^3$ | 0.278 | 0.298 |
| $\alpha_{L,f}$ | cm | 5.74 | 20.85 |
| $\kappa_{f,im}$ | $hr^{-1}$ | 0.0003 | 0.0305 |
| *Immobile matrix domain* | | | |
| $\theta_{im}$ | $cm^3/cm^3$ | 0.120 | 0.077 |
| Dual-permeability model | | | |
| *Fracture* | | | |
| $w_f$ | – | 0.42 | 0.44 |
| $w_f I_f/I_0$ | – | 0.8403 | 0.9996 |
| $\theta_f$ | $cm^3/cm^3$ | 0.1952 | 0.3545 |
| $\alpha_{L,f}$ | cm | 7.462 | 20.85 |
| $\kappa_{f,m}$ | $hr^{-1}$ | 0.0443 | 0.09145 |
| *Matrix* | | | |
| $\theta_m$ | $cm^3/cm^3$ | 0.5448 | 0.3911 |
| $\alpha_{L,m}$ | cm | 1.00 | 1.00 |

**Table 3**
Model parameters for Isoproturon and Metribuzin in the undisturbed soil cores under unsaturated conditions.

| Parameter | Unit | Soil core 1 | | Soil core 2 | |
|---|---|---|---|---|---|
| | | Isoproturon | Metribuzin | Isoproturon | Metribuzin |
| Dual-porosity model | | | | | |
| $K^{sw}$ | $g/cm^3$ | 1.31 | 1.17 | 1.28 | 0.64 |
| $F_f^{sw}$ | – | 2.3e−2 | 1.64e−2 | 3.6e−2 | 4e−3 |
| $F_{im}^{sw}$ | – | 2.62e−2 | 2.74e−2 | 3.6e−2 | 4e−2 |
| $\kappa^{sw}$ | $hr^{-1}$ | 5.47e−2 | 5.75e−2 | 7.46e−2 | 0.1296 |
| $\mu$ | $hr^{-1}$ | 0.11325 | 6.375e−2 | 0.1284 | 6.5e−2 |
| Dual-permeability model | | | | | |
| $K^{sw}$ | $g/cm^3$ | 1.31 | 1.17 | 1.28 | 0.64 |
| $F_f^{sw}$ | – | 8.625e−2 | 6.56e−2 | 3.6e−2 | 4e−3 |
| $F_m^{sw}$ | – | 0.131 | 0.137 | 0.994 | 0.321 |
| $\kappa^{sw}$ | $hr^{-1}$ | 8.205e−3 | 8.625e−3 | 7.46e−3 | 1.296e−2 |
| $\mu$ | $hr^{-1}$ | 4.53e−2 | 1.53e−2 | 1.07e−2 | 6.5e−3 |

where $c$ is the aqueous PFAS concentration, $c_p$ is the aqueous precursor concentration, and $R$, $v$, $D$, and $\mu$ are respectively the effective retardation factor, porewater velocity, dispersion coefficient, and transformation rate constant. The effective parameters are derived from those of the dual-porosity model through a temporal moment analysis method (see Appendix C), which yields $R = \frac{w_f\theta_f R_f + w_{im}\theta_{im} R_{im}}{w_f\theta_f}$, $v = v_f$, $D = D_f$, and $\mu = \frac{w_f\theta_f\mu_f + w_{im}\theta_{im}\mu_{im}}{w_f\theta_f}$, where the subscripts "f" and "im" denote the parameters defined in the fracture and immobile matrix domains of the dual-porosity model.

The above simulations are conducted separately for PFOS and PFOSB. The PFOS simulations focus on the transport of legacy PFOS, while the PFOSB simulations—which exclude any release of legacy PFOS from biosolids—examine the movement of PFOSB and its transformation into PFOS. The results are analyzed in the following section.

### 4.2. Long-term PFAS mass discharge and accumulation

We first analyze the base case dual-permeability simulation results. The mass discharge from the vadose zone to groundwater and the spatial aqueous concentration profiles in the fracture and matrix domains are presented in Fig. 5. The results suggest that both PFOS and PFOSB are strongly retained in the vadose zone. Less than 66% of legacy PFOS and 25% of PFOSB and PFOSB-derived PFOS are discharged to groundwater after 200 years. Of the total PFAS mass (accounting for both PFOS and PFOSB) discharged to groundwater, the majority (approximately 98%) of the leaching occurred through the fracture domain.

**Table 4**
Soil properties and PFAS transport parameters (Smith et al., 2024) for field-scale simulations of PFAS transport in a heterogeneous vadose zone. Note that due to the lack of field data and experimental characterizations, the PFOSB release rate is assumed to be the same as PFOS and its interfacial adsorption coefficients are estimated based on quantitative-structure/property-relationship models (Brusseau and Van Glubt, 2021; Brusseau, 2023b). The solid-phase adsorption coefficient is computed from the product of the organic carbon normalized sorption coefficient and the fraction of organic carbon (Brusseau, 2023b). The transformation rate constant of PFOSB is estimated from its half-life time (Liu et al., 2021) using a first-order transformation model.

| Parameter | Unit | Value | |
|---|---|---|---|
| Soil properties | | Fracture | Matrix |
| $w$ | – | 0.03 | 0.97 |
| $\rho$ | $g/cm^3$ | 1.58 | 1.66 |
| $\theta_r$ | $cm^3/cm^3$ | 0.0 | 0.0 |
| $\theta_s$ | $cm^3/cm^3$ | 0.75 | 0.457 |
| $\alpha_{VG}$ | $cm^{-1}$ | 0.1 | 0.03 |
| $n_{VG}$ | – | 1.8 | 1.15 |
| $k$ | cm/hr | 20.1 | 2.54e−1 |
| PFAS transport | | PFOS | PFOSB |
| Release rate | $g/cm^2/yr$ | 6.72e−8 | 6.72e−8 |
| $M_w$ | g/mol | 500.13 | 587.32 |
| $\kappa_{f,m}$ | $hr^{-1}$ | 4e−3 | 4e−3 |
| $\alpha_L$ | cm | 24.4 | 24.4 |
| $K^{aw}$ | cm | 4.79e−2 | 1.26e−1 |
| $K^{sw}$ | $cm^3/g$ | 1.03 | 4.47 |
| $\mu$ | $hr^{-1}$ | 0 | 4.28e−5 |

The residence time for PFOS and PFOSB in the fracture domain is approximately 20 years and 54 years, respectively. They are even greater in the matrix domain (approximately $9.6\times10^3$ years for PFOS and $2.9\times10^4$ years for PFOSB). The residence time is much greater than the time scale of fracture–matrix mass transfer (approximately 10 days), giving sufficient time for PFAS in the fracture and matrix domains to reach equilibrium. Therefore, no significant nonequilibrium transport phenomena (e.g., early arrival and long tail) are observed. Similarly, because the residence time is also much greater than the half-life time of PFOSB transformation (approximately 1.8 years), the majority of PFOSB (approximately 93% by the end of the 800-year simulation) has been transformed into PFOS before reaching the groundwater. The transformation of PFOSB adds additional PFOS mass discharge to groundwater. Under the simulated conditions, the PFOSB-derived PFOS accounts for 48% of the total PFOS (including legacy and PFOSB-derived PFOS) mass discharge to groundwater.

The simulations by the dual-permeability and dual-porosity models are almost identical (see Figs. 5a–b and Fig. D.2). We quantify their differences using the first and second temporal moments of the mass discharge concentration curves, i.e., $\delta m_n = |(m_{n,\text{DualPerm}} - m_{n,\text{DualPoro}})/m_{n,\text{DualPerm}}| \times 100\%$, where $m_n$ is the first ($n = 1$) or second ($n = 2$) temporal moment, and the subscripts "DualPerm" and "DualPoro" denote the dual-permeability and the dual-porosity models (see Appendix C for the calculations of $m_n$). The computed $\delta m_1$ and $\delta m_2$ are respectively 0.0019% and 0.0067% for PFOS, and 4.6% and 5.0% for PFOSB. The difference between the dual-permeability and dual-porosity models is small because the residence time of PFOS and PFOSB in the matrix domain is much greater than those in the fracture domain, i.e., PFOS and PFOSB can be considered essentially immobile in the matrix domain. This suggests that a dual-porosity model is sufficient for simulating PFAS transport in the vadose zone under the set of conditions considered at the site.

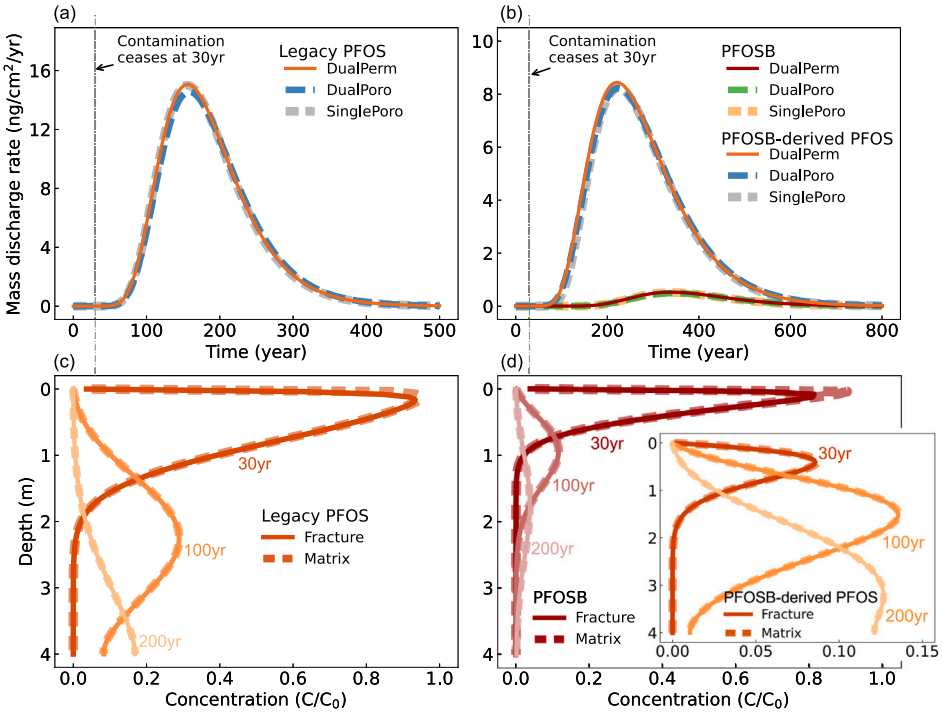


**Fig. 5.** Long-term PFAS leaching and mass discharge in a heterogeneous vadose zone. The contamination phase (0~30 years) is simulated by a dual-permeability model, followed by three independent post-contamination simulations: a dual-permeability simulation (denoted as "DualPerm"), a dual-porosity simulation (denoted as "DualPoro"), and an effective single-porosity simulation (denoted as "SinglePoro"). (a–b) are the mass discharge rates computed from all three models and (c-d) are the aqueous concentration profiles in the fracture domain and matrix domain computed from the dual-permeability model. The aqueous concentrations are normalized by the inlet PFOS (c) or PFOSB (d) concentrations. For clarity, we refer to the PFOS directly released from biosolids as "legacy PFOS", while that generated by PFOSB transformation as "PFOSB-derived PFOS".

Notably, the effective single-porosity model simulation also gives results almost identical to those of the dual-permeability and dual-porosity models. The computed relative differences of the first and second moments ($\delta m_1$ and $\delta m_2$) are respectively 0 and 1.6% for legacy PFOS simulations and are respectively 3.5% and 7.0% for PFOSB simulations. Here $\delta m_n$ is defined as $\delta m_n = |(m_{n,\text{DualPoro}} - m_{n,\text{SinglePoro}})/m_{n,\text{DualPoro}}| \times 100\%$ where the subscript "SinglePoro" denotes the single-porosity model (see Appendix C for the calculations of $m_n$). The excellent agreement between the single-porosity and dual-porosity models is expected given the earlier observation that PFAS in the fracture and matrix domains can be considered as in equilibrium.

The analyses presented above suggest a more general model simplification strategy. *A priori*, one can estimate the residence time of the PFAS in the fracture and matrix domains, and the time scale of mass transfer between the fracture and matrix domains. If the residence time in the matrix domain is much greater than that in the fracture domain, a dual-porosity model should be sufficient. Furthermore, if the mass transfer time is much smaller than the residence time in the fracture domain, we can further simplify by employing an effective single-porosity model. In this case, the analytical solutions presented in Guo et al. (2022) can be directly modified (using the parameterization of the effective single-porosity model) to conduct the simulation. The criteria for determining the relative importance of different transport processes based on their time scales and selecting the appropriate model options can be derived from the (semi-)analytical solutions (e.g., Valocchi, 1985), which we summarize in Appendix C.

Finally, we recognize that the semi-analytical models in the present study rely on a steady-state infiltration assumption that may not hold under all conditions. For instance, rainfall or irrigation events can create strong transient water flow near the land surface, particularly during initial wetting and subsequent drainage. Under such conditions, the semi-analytical models assuming steady-state may predict PFAS concentration profiles in the upper ~1 meter of soil that are notably different from the numerical simulations representing transient infiltration (Zeng and Guo, 2023). However, numerous field observations and modeling studies of non-PFAS solute transport show that these transient effects attenuate rapidly with depth and become negligible in deeper vadose zones (e.g., van Genuchten and Wierenga, 1976, 1977; Jury and Horton, 2004; Russo and Fiori, 2008). Furthermore, recent PFAS modeling studies indicate that infiltration-driven transients (30-min resolution rainfall) have a relatively minor impact on the long-term leaching of the strongly interfacially-active (e.g., longer-chain) PFAS, even in highly heterogeneous vadose zones (Zeng and Guo, 2023). Therefore, the steady-state infiltration assumption is likely appropriate for modeling long-term PFAS leaching in vadose zones that extend beyond the shallow soil layer (e.g., deeper than 2 to 3 meters below the land surface).

## 5. Summary and conclusion

We have developed a set of semi-analytical models for simulating the long-term fate and transport of PFAS in heterogeneous vadose zones and their mass discharge to groundwater. We employ the dual- or multi-continuum conceptualization that represents the high-conductivity channels (e.g., macropores or fractures) and low-conductivity matrix domains (e.g., soil aggregates) as overlapping continua. Depending on the specific representation used for the matrix domain, we have formulated three models: dual-porosity, dual-permeability, and tripe-porosity models. The dual-porosity and dual-permeability models represent the high- and low-conductivity transport pathways by two overlapping domains (i.e., a fracture domain and a matrix domain). The dual-porosity model assumes water is mobile in the fracture domain but immobile in the matrix domain, while the dual-permeability model considers mobile water in both domains. Compared to the dual-permeability model, the triple-porosity model includes an additional immobile matrix domain.

All three models account for PFAS-specific retention and transport processes, including advective and dispersive transport, two-site and multi-site rate-limited adsorption at solid–water and air–water interfaces, and biochemical transformation. We assume steady-state infiltration and linear interfacial adsorption, and derive semi-analytical solutions for the models. The semi-analytical solutions allow for arbitrary initial and boundary conditions for the transport equations. To the best of our knowledge, these semi-analytical models are the first that couple multi-site rate-limited solid-phase and air–water interfacial adsorption and biochemical transformation into dual-porosity, dual-permeability, and tripe-porosity model formalisms.

These semi-analytical models have been tested and evaluated for simulating miscible displacement experiments for a wide range of solutes (passive or interfacially-active), soil types, soil heterogeneities, and wetting conditions. Example one-dimensional field-scale simulations demonstrate that the models are capable of simulating long-term leaching and mass discharge of PFAS in the presence of precursor transformation in heterogeneous vadose zones. The results using two example longer-chain PFAS (PFOS and PFOSB) suggest that the large residence time (due to strong retention) in the vadose zone has eliminated any nonequilibrium behaviors (e.g., no early-arrival and long-tailing) under the simulated conditions. The large residence time also gives sufficient time for the precursor to transform into PFOS, which adds additional mass discharge of PFOS to groundwater. We have also illustrated that the dual-porosity model may be sufficient to simulate PFAS transport in the heterogeneous vadose zone if the residence time in the matrix domain is significantly greater than that in the fracture domain. Furthermore, a much simpler effective single-porosity model may be used when the residence time of PFAS in the vadose zone is much greater than the time scale of mass transfer between the fracture and matrix domains. Based on these analyses, we have developed a generalized strategy to guide the selection of the appropriate model.

Due to their computational efficiency, the semi-analytical solutions can be used as practical tools for screen-type analysis at PFAS-contaminated sites. Although the semi-analytical solutions assume a uniform heterogeneous vadose zone, they can indirectly account for the impact of spatial heterogeneity by running Monte Carlo simulations for a wide range of soil types relevant to a specific site. These simulations can provide the upper and lower bounds for expected long-term PFAS leaching and mass discharge at the contaminated sites. The computed mass discharge rates can also be incorporated into groundwater transport models (e.g., simple dilution factor models or other more sophisticated process-based models) to establish PFAS-specific soil screening levels for heterogeneous vadose zones, as recently demonstrated by Smith et al. (2024) and Ma et al. (2025) using the analytical solution of Guo et al. (2022) for homogeneous vadose zones. We anticipate that these efforts will advance site characterization, risk assessment, and design of remedial actions for PFAS-contaminated sites.

## CRediT authorship contribution statement

**Sidian Chen:** Writing – original draft, Visualization, Validation, Software, Methodology, Investigation, Formal analysis, Data curation. **Bo Guo:** Writing – review & editing, Supervision, Resources, Project administration, Methodology, Funding acquisition, Formal analysis, Conceptualization.

## Declaration of competing interest

The authors declare that they have no known competing financial interests or personal relationships that could have appeared to influence the work reported in this paper.

## Acknowledgments

This work was in part supported by National Science Foundation, United States (2237015, 2225750) and US Army Engineer Research and Development Center (ERDC) (W912HZ-23-2-0009). The source codes for the semi-analytical and numerical solutions are openly available at https://github.com/GuoSFPLab/SemiAnalyticalSoln-PFAS-HeteroVZ.

## Appendix A. Semi-analytical solutions for dual-permeability and triple-porosity models

We derive the semi-analytical solutions for the dual-permeability and triple-porosity models using the Laplace transform and inverse Laplace transform. Because the two models share the same procedure, the more sophisticated triple-porosity model formulations are used to illustrate the general derivations. To obtain the solutions for the dual-permeability model, one only needs to remove all the terms related to the immobile matrix domain and repeat the following procedures. The derivations for PFAAs and precursors are almost the same, except for one derivation step right after taking the Laplace transform of the governing equations in time. We explain the difference in the Laplace transform (Appendix A.3).

### A.1. Nondimensionalized governing equations

We nondimensionalize the governing equations (Eqs. (2)–(8)), initial conditions (Eqs. (9)–(14)), and boundary conditions (Eqs. (15)–(16)) using the following dimensionless parameters: $\bar{v} = (w_f\theta_f v_f + w_m\theta_m v_m)/\theta$ where $\theta = w_f\theta_f + w_m\theta_m + w_{im}\theta_{im}$, $T = t/(L/\bar{v})$, and $Z = z/L$. Because the PFAS concentration shows up linearly in every term and it does not influence the derivation, we keep its dimensional form to simplify the notation.

After the nondimensionalization, the governing equations in the fracture domain become

$$
\begin{aligned}
&-\frac{D_f}{Lv_f}\frac{\partial^2 c_f}{\partial Z^2}+\frac{\partial c_f}{\partial Z}+\frac{R_f\bar{v}}{v_f}\frac{\partial c_f}{\partial T}\pm\frac{\mu_f L}{v_f}c_{p,f}+\frac{\kappa_{f,m}L}{\theta_f v_f}\frac{w_m}{w_f}(c_f-c_m)\\
&\qquad+\sum_{i=1}^{N_f^{sw}}\frac{\bar{v}\rho_f}{\theta_f v_f}\frac{\partial c_{f,i}^{sw}}{\partial T}+\sum_{i=1}^{N_f^{aw}}\frac{\bar{v}A_f^{aw}}{\theta_f v_f}\frac{\partial c_{f,i}^{aw}}{\partial T}=0,\\
&\frac{\partial c_{f,i}^{sw}}{\partial T}=\frac{L\kappa_{f,i}^{sw}}{\bar{v}}\left[f_{f,i}^{sw}\left(1-F_{f,eq}^{sw}\right)K_f^{sw}c_f-c_{f,i}^{sw}\right],\quad i=1,2,\ldots,N_f^{sw},\\
&\frac{\partial c_{f,i}^{aw}}{\partial T}=\frac{L\kappa_{f,i}^{aw}}{\bar{v}}\left[f_{f,i}^{aw}\left(1-F_{f,eq}^{aw}\right)K_f^{aw}c_f-c_{f,i}^{aw}\right],\quad i=1,2,\ldots,N_f^{aw}.
\end{aligned}
\tag{A.1}
$$

The nondimensionalized governing equation in the mobile matrix domain is given by

$$
\begin{aligned}
&-\frac{D_m}{Lv_m}\frac{\partial^2 c_m}{\partial Z^2}+\frac{\partial c_m}{\partial Z}+\frac{R_m\bar{v}}{v_m}\frac{\partial c_m}{\partial T}\pm\frac{\mu_m L}{v_m}c_{p,m}-\frac{\kappa_{f,m}L}{\theta_m v_m}(c_f-c_m)\\
&+\sum_{i=1}^{N_m^{sw}}\frac{\bar{v}\rho_m}{\theta_m v_m}\frac{\partial c_{m,i}^{sw}}{\partial T}+\sum_{i=1}^{N_m^{aw}}\frac{\bar{v}A_m^{aw}}{\theta_m v_m}\frac{\partial c_{m,i}^{aw}}{\partial T}+\sum_{i=1}^{N_{im}}\frac{w_{im}w_{im,i}\kappa_{m,im,i}L}{w_m\theta_m v_m}(c_m-c_{im,i})=0,\\
&\frac{\partial c_{m,i}^{sw}}{\partial T}=\frac{L\kappa_{m,i}^{sw}}{\bar{v}}\left[f_{m,i}^{sw}\left(1-F_{m,eq}^{sw}\right)K_m^{sw}c_m-c_{m,i}^{sw}\right],\quad i=1,2,\ldots,N_m^{sw},\\
&\frac{\partial c_{m,i}^{aw}}{\partial T}=\frac{L\kappa_{m,i}^{aw}}{\bar{v}}\left[f_{m,i}^{aw}\left(1-F_{m,eq}^{aw}\right)K_m^{aw}c_m-c_{m,i}^{aw}\right],\quad i=1,2,\ldots,N_m^{aw}.
\end{aligned}
\tag{A.2}
$$

The governing equations for the immobile matrix domain $i$ ($i = 1, 2, \ldots, N_{\mathrm{im}}$) are

$$\begin{aligned} &R_{\mathrm{im},i}\frac{\partial c_{\mathrm{im},i}}{\partial T} - \frac{\kappa_{\mathrm{m,im},i}L}{\theta_{\mathrm{im},i}\bar{v}}(c_{\mathrm{m}} - c_{\mathrm{im},i}) \pm \frac{\mu_{\mathrm{im},i}L}{\bar{v}}c_{\mathrm{p,im},i} \\ &\qquad + \frac{\rho_{\mathrm{im}}}{\theta_{\mathrm{im},i}}\frac{\partial c^{\mathrm{sw}}_{\mathrm{im},i}}{\partial T} + \frac{A^{\mathrm{aw}}_{\mathrm{im}}}{\theta_{\mathrm{im},i}}\frac{\partial c^{\mathrm{aw}}_{\mathrm{im},i}}{\partial T} = 0, \\ &\frac{\partial c^{\mathrm{sw}}_{\mathrm{im},i}}{\partial T} = \frac{\kappa^{\mathrm{sw}}_{\mathrm{im},i}L}{\bar{v}}\left[(1 - F^{\mathrm{sw}}_{\mathrm{im,eq},i})K^{\mathrm{sw}}_{\mathrm{im}}c_{\mathrm{im},i} - c^{\mathrm{sw}}_{\mathrm{im},i}\right], \\ &\frac{\partial c^{\mathrm{aw}}_{\mathrm{im},i}}{\partial T} = \frac{\kappa^{\mathrm{aw}}_{\mathrm{im},i}L}{\bar{v}}\left[\left(1 - F^{\mathrm{aw}}_{\mathrm{im,eq},i}\right)K^{\mathrm{aw}}_{\mathrm{im}}c_{\mathrm{im},i} - c^{\mathrm{aw}}_{\mathrm{im},i}\right]. \end{aligned} \tag{A.3}$$

Eqs. (A.1)–(A.3) provide the dimensionless triple-porosity formulation for the transport of a PFAS in a semi-infinite vadose zone, which is subject to the following initial and boundary conditions

$$\begin{aligned} &c_{\mathrm{f}}(Z, T=0) = c^0_{\mathrm{f}}(Z), \\ &c^{\mathrm{sw}}_{\mathrm{f},i}(Z, T=0) = c^{\mathrm{sw},0}_{\mathrm{f},i}(Z), \quad i = 1, 2, \ldots, N^{\mathrm{sw}}_{\mathrm{f}}, \\ &c^{\mathrm{aw}}_{\mathrm{f},i}(Z, T=0) = c^{\mathrm{aw},0}_{\mathrm{f},i}(Z), \quad i = 1, 2, \ldots, N^{\mathrm{aw}}_{\mathrm{f}}, \\ &c_{\mathrm{m}}(Z, T=0) = c^0_{\mathrm{m}}(Z), \\ &c^{\mathrm{sw}}_{\mathrm{m},i}(Z, T=0) = c^{\mathrm{sw},0}_{\mathrm{m},i}(Z), \quad i = 1, 2, \ldots, N^{\mathrm{sw}}_{\mathrm{m}}, \\ &c^{\mathrm{aw}}_{\mathrm{m},i}(Z, T=0) = c^{\mathrm{aw},0}_{\mathrm{m},i}(Z), \quad i = 1, 2, \ldots, N^{\mathrm{aw}}_{\mathrm{m}}, \\ &c_{\mathrm{im},i}(Z, T=0) = c^0_{\mathrm{im},i}(Z), \quad i = 1, 2, \ldots, N_{\mathrm{im}}, \\ &c^{\mathrm{sw}}_{\mathrm{im},i}(Z, T=0) = c^{\mathrm{sw},0}_{\mathrm{im},i}(Z), \quad i = 1, 2, \ldots, N_{\mathrm{im}}, \\ &c^{\mathrm{aw}}_{\mathrm{im},i}(Z, T=0) = c^{\mathrm{aw},0}_{\mathrm{im},i}(Z), \quad i = 1, 2, \ldots, N_{\mathrm{im}}, \\ &\left[-\frac{D_{\mathrm{f}}}{Lv_{\mathrm{f}}}\frac{\partial c_{\mathrm{f}}}{\partial Z} + c_{\mathrm{f}}\right]_{Z=0} = c_{\mathrm{f,in}}(T), \quad \& \quad \left[\frac{\partial c_{\mathrm{f}}}{\partial Z}\right]_{Z=\infty} = 0, \\ &\left[-\frac{D_{\mathrm{m}}}{Lv_{\mathrm{m}}}\frac{\partial c_{\mathrm{m}}}{\partial Z} + c_{\mathrm{m}}\right]_{Z=0} = c_{\mathrm{m,in}}(T), \quad \& \quad \left[\frac{\partial c_{\mathrm{m}}}{\partial Z}\right]_{Z=\infty} = 0. \end{aligned} \tag{A.4}$$

### A.2. Simplification of nondimensionalized governing equations

For the convenience of derivation, we simplify the notations of the parameters and the expressions of Eqs. (A.1)–(A.4). The governing equations for PFAS transport in the fracture domain are simplified as

$$\begin{aligned} &-\frac{1}{\mathcal{P}_{\mathrm{f}}}\frac{\partial^2 c_{\mathrm{f}}}{\partial Z^2} + \frac{\partial c_{\mathrm{f}}}{\partial Z} + \mathcal{R}_{\mathrm{f}}\frac{\partial c_{\mathrm{f}}}{\partial T} \pm \mathcal{U}_{\mathrm{f}}c_{\mathrm{p,f}} + \mathcal{K}_{\mathrm{f}}(c_{\mathrm{f}} - c_{\mathrm{m}}) \\ &\qquad + \sum_{i=1}^{N^{\mathrm{sw}}_{\mathrm{f}}}\mathcal{R}^{\mathrm{sw}}_{\mathrm{f}}\frac{\partial c^{\mathrm{sw}}_{\mathrm{f},i}}{\partial T} + \sum_{i=1}^{N^{\mathrm{aw}}_{\mathrm{f}}}\mathcal{R}^{\mathrm{aw}}_{\mathrm{f}}\frac{\partial c^{\mathrm{aw}}_{\mathrm{f},i}}{\partial T} = 0, \\ &\frac{\partial c^{\mathrm{sw}}_{\mathrm{f},i}}{\partial T} = \mathcal{A}^{\mathrm{sw}}_{\mathrm{f},i}c_{\mathrm{f}} - \mathcal{B}^{\mathrm{sw}}_{\mathrm{f},i}c^{\mathrm{sw}}_{\mathrm{f},i}, \quad i = 1, 2, \ldots, N^{\mathrm{sw}}_{\mathrm{f}}, \\ &\frac{\partial c^{\mathrm{aw}}_{\mathrm{f},i}}{\partial T} = \mathcal{A}^{\mathrm{aw}}_{\mathrm{f},i}c_{\mathrm{f}} - \mathcal{B}^{\mathrm{aw}}_{\mathrm{f},i}c^{\mathrm{aw}}_{\mathrm{f},i}, \quad i = 1, 2, \ldots, N^{\mathrm{aw}}_{\mathrm{f}}, \end{aligned} \tag{A.5}$$

where $\mathcal{P}_{\mathrm{f}} = v_{\mathrm{f}}L/D_{\mathrm{f}}$, $\mathcal{R}_{\mathrm{f}} = \bar{v}R_{\mathrm{f}}/v_{\mathrm{f}}$, $\mathcal{U}_{\mathrm{f}} = \mu_{\mathrm{f}}L/v_{\mathrm{f}}$, $\mathcal{K}_{\mathrm{f}} = (\kappa_{\mathrm{f,m}}Lw_{\mathrm{m}})/(\theta_{\mathrm{f}}v_{\mathrm{f}}w_{\mathrm{f}})$, $\mathcal{R}^{\mathrm{sw}}_{\mathrm{f}} = (\bar{v}\rho_{\mathrm{f}})/(\theta_{\mathrm{f}}v_{\mathrm{f}})$, $\mathcal{R}^{\mathrm{aw}}_{\mathrm{f}} = (\bar{v}A^{\mathrm{aw}}_{\mathrm{f}})/(\theta_{\mathrm{f}}v_{\mathrm{f}})$, $\mathcal{A}^{\mathrm{sw}}_{\mathrm{f},i} = (L\kappa^{\mathrm{sw}}_{\mathrm{f},i}/\bar{v})f^{\mathrm{sw}}_{\mathrm{f},i}\left(1 - F^{\mathrm{sw}}_{\mathrm{f,eq}}\right)K^{\mathrm{sw}}_{\mathrm{f}}$, $\mathcal{B}^{\mathrm{sw}}_{\mathrm{f},i} = L\kappa^{\mathrm{sw}}_{\mathrm{f},i}/\bar{v}$, $\mathcal{A}^{\mathrm{aw}}_{\mathrm{f},i} = (L\kappa^{\mathrm{aw}}_{\mathrm{f},i}/\bar{v})f^{\mathrm{aw}}_{\mathrm{f},i}\left(1 - F^{\mathrm{aw}}_{\mathrm{f,eq}}\right)K^{\mathrm{aw}}_{\mathrm{f}}$, $\mathcal{B}^{\mathrm{aw}}_{\mathrm{f},i} = L\kappa^{\mathrm{aw}}_{\mathrm{f},i}/\bar{v}$.

The governing equations for PFAS transport in the mobile matrix domain are simplified as

$$\begin{aligned} &-\frac{1}{\mathcal{P}_{\mathrm{m}}}\frac{\partial^2 c_{\mathrm{m}}}{\partial Z^2} + \frac{\partial c_{\mathrm{m}}}{\partial Z} + \mathcal{R}_{\mathrm{m}}\frac{\partial c_{\mathrm{m}}}{\partial T} \pm \mathcal{U}_{\mathrm{m}}c_{\mathrm{p,m}} - \mathcal{K}_{\mathrm{m}}(c_{\mathrm{f}} - c_{\mathrm{m}}) \\ &+ \sum_{i=1}^{N^{\mathrm{sw}}_{\mathrm{m}}}\mathcal{R}^{\mathrm{sw}}_{\mathrm{m}}\frac{\partial c^{\mathrm{sw}}_{\mathrm{m},i}}{\partial T} + \sum_{i=1}^{N^{\mathrm{aw}}_{\mathrm{m}}}\mathcal{R}^{\mathrm{aw}}_{\mathrm{m}}\frac{\partial c^{\mathrm{aw}}_{\mathrm{m},i}}{\partial T} + \sum_{i=1}^{N_{\mathrm{im}}}\mathcal{K}_{\mathrm{mim},i}(c_{\mathrm{m}} - c_{\mathrm{im},i}) = 0, \\ &\frac{\partial c^{\mathrm{sw}}_{\mathrm{m},i}}{\partial T} = \mathcal{A}^{\mathrm{sw}}_{\mathrm{m},i}c_{\mathrm{m}} - \mathcal{B}^{\mathrm{sw}}_{\mathrm{m},i}c^{\mathrm{sw}}_{\mathrm{m},i}, \quad i = 1, 2, \ldots, N^{\mathrm{sw}}_{\mathrm{m}}, \\ &\frac{\partial c^{\mathrm{aw}}_{\mathrm{m},i}}{\partial T} = \mathcal{A}^{\mathrm{aw}}_{\mathrm{m},i}c_{\mathrm{m}} - \mathcal{B}^{\mathrm{aw}}_{\mathrm{m},i}c^{\mathrm{aw}}_{\mathrm{m},i}, \quad i = 1, 2, \ldots, N^{\mathrm{aw}}_{\mathrm{m}}, \end{aligned} \tag{A.6}$$

where $\mathcal{P}_{\mathrm{m}} = v_{\mathrm{m}}L/D_{\mathrm{m}}$, $\mathcal{R}_{\mathrm{m}} = \bar{v}R_{\mathrm{m}}/v_{\mathrm{m}}$, $\mathcal{U}_{\mathrm{m}} = \mu_{\mathrm{m}}L/v_{\mathrm{m}}$, $\mathcal{K}_{\mathrm{m}} = (\kappa_{\mathrm{f,m}}L)/(\theta_{\mathrm{m}}v_{\mathrm{m}})$, $\mathcal{R}^{\mathrm{sw}}_{\mathrm{m}} = (\bar{v}\rho_{\mathrm{m}})/(\theta_{\mathrm{m}}v_{\mathrm{m}})$, $\mathcal{R}^{\mathrm{aw}}_{\mathrm{m}} = (\bar{v}A^{\mathrm{aw}}_{\mathrm{m}})/(\theta_{\mathrm{m}}v_{\mathrm{m}})$, $\mathcal{A}^{\mathrm{sw}}_{\mathrm{m},i} = (L\kappa^{\mathrm{sw}}_{\mathrm{m},i}/\bar{v})f^{\mathrm{sw}}_{\mathrm{m},i}\left(1 - F^{\mathrm{sw}}_{\mathrm{m,eq}}\right)K^{\mathrm{sw}}_{\mathrm{m}}$, $\mathcal{B}^{\mathrm{sw}}_{\mathrm{m},i} = L\kappa^{\mathrm{sw}}_{\mathrm{m},i}/\bar{v}$, $\mathcal{A}^{\mathrm{aw}}_{\mathrm{m},i} = (L\kappa^{\mathrm{aw}}_{\mathrm{m},i}/\bar{v})f^{\mathrm{aw}}_{\mathrm{m},i}\left(1 - F^{\mathrm{aw}}_{\mathrm{m,eq}}\right)K^{\mathrm{aw}}_{\mathrm{m}}$, $\mathcal{B}^{\mathrm{aw}}_{\mathrm{m},i} = L\kappa^{\mathrm{aw}}_{\mathrm{m},i}/\bar{v}$, and $\mathcal{K}_{\mathrm{mim},i} = (w_{\mathrm{im}}w_{\mathrm{im},i}\kappa_{\mathrm{m,im},i}L)/(w_{\mathrm{m}}\theta_{\mathrm{m}}v_{\mathrm{m}})$.

The governing equations for PFAS transport in the immobile matrix domain are simplified as

$$\begin{aligned} &\mathcal{R}_{\mathrm{im},i}\frac{\partial c_{\mathrm{im},i}}{\partial T} - \mathcal{K}_{\mathrm{im},i}(c_{\mathrm{m}} - c_{\mathrm{im},i}) \pm \mathcal{U}_{\mathrm{im},i}c_{\mathrm{im},i} \\ &\qquad + \mathcal{R}^{\mathrm{sw}}_{\mathrm{im},i}\frac{\partial c^{\mathrm{sw}}_{\mathrm{im},i}}{\partial T} + \mathcal{R}^{\mathrm{aw}}_{\mathrm{im},i}\frac{\partial c^{\mathrm{aw}}_{\mathrm{im},i}}{\partial T} = 0, \\ &\frac{\partial c^{\mathrm{sw}}_{\mathrm{im},i}}{\partial T} = \mathcal{A}^{\mathrm{sw}}_{\mathrm{im},i}c_{\mathrm{im},i} - \mathcal{B}^{\mathrm{sw}}_{\mathrm{im},i}c^{\mathrm{sw}}_{\mathrm{im},i}, \\ &\frac{\partial c^{\mathrm{aw}}_{\mathrm{im},i}}{\partial T} = \mathcal{A}^{\mathrm{aw}}_{\mathrm{im},i}c_{\mathrm{im},i} - \mathcal{B}^{\mathrm{aw}}_{\mathrm{im},i}c^{\mathrm{aw}}_{\mathrm{im},i}, \end{aligned} \tag{A.7}$$

where $\mathcal{R}_{\mathrm{im},i} = R_{\mathrm{im},i}$, $\mathcal{U}_{\mathrm{im},i} = \mu_{\mathrm{im},i}L/\bar{v}$, $\mathcal{K}_{\mathrm{im},i} = (\kappa_{\mathrm{m,im},i}L)/(\theta_{\mathrm{im},i}\bar{v})$, $\mathcal{R}^{\mathrm{sw}}_{\mathrm{im},i} = \rho_{\mathrm{im}}/\theta_{\mathrm{im},i}$, $\mathcal{R}^{\mathrm{aw}}_{\mathrm{im},i} = A^{\mathrm{aw}}_{\mathrm{im}}/\theta_{\mathrm{im},i}$, $\mathcal{A}^{\mathrm{sw}}_{\mathrm{im},i} = (L\kappa^{\mathrm{sw}}_{\mathrm{im},i}/\bar{v})\left(1 - F^{\mathrm{sw}}_{\mathrm{im,eq},i}\right)K^{\mathrm{sw}}_{\mathrm{im}}$, $\mathcal{B}^{\mathrm{sw}}_{\mathrm{im},i} = L\kappa^{\mathrm{sw}}_{\mathrm{im},i}/\bar{v}$, $\mathcal{A}^{\mathrm{aw}}_{\mathrm{im},i} = (L\kappa^{\mathrm{aw}}_{\mathrm{im},i}/\bar{v})\left(1 - F^{\mathrm{aw}}_{\mathrm{im,eq},i}\right)K^{\mathrm{aw}}_{\mathrm{im}}$, and $\mathcal{B}^{\mathrm{aw}}_{\mathrm{im},i} = L\kappa^{\mathrm{aw}}_{\mathrm{im},i}/\bar{v}$, and $i = 1, 2, \ldots, N_{\mathrm{im}}$.

The equations for initial conditions remain the same as those in Eq. (A.4), while the equations for boundary conditions become

$$\begin{aligned} &\left[-\frac{1}{\mathcal{P}_{\mathrm{f}}}\frac{\partial c_{\mathrm{f}}}{\partial Z} + c_{\mathrm{f}}\right]_{Z=0} = c_{\mathrm{f,in}}(T), \quad \& \quad \left[\frac{\partial c_{\mathrm{f}}}{\partial Z}\right]_{Z=\infty} = 0, \\ &\left[-\frac{1}{\mathcal{P}_{\mathrm{m}}}\frac{\partial c_{\mathrm{m}}}{\partial Z} + c_{\mathrm{m}}\right]_{Z=0} = c_{\mathrm{m,in}}(T), \quad \& \quad \left[\frac{\partial c_{\mathrm{m}}}{\partial Z}\right]_{Z=\infty} = 0. \end{aligned} \tag{A.8}$$

### A.3. Laplace transform

We take the Laplace transform in time for Eqs. (A.5)–(A.7), which yields

$$\begin{aligned} &-\frac{1}{\mathcal{P}_{\mathrm{f}}}\frac{\partial^2 \tilde{c}_{\mathrm{f}}}{\partial Z^2} + \frac{\partial \tilde{c}_{\mathrm{f}}}{\partial Z} + \mathcal{R}_{\mathrm{f}}(s\tilde{c}_{\mathrm{f}} - c^0_{\mathrm{f}}) \pm \mathcal{U}_{\mathrm{f}}\tilde{c}_{\mathrm{p,f}} + \mathcal{K}_{\mathrm{f}}(\tilde{c}_{\mathrm{f}} - \tilde{c}_{\mathrm{m}}) \\ &+ \sum_{i=1}^{N^{\mathrm{sw}}_{\mathrm{f}}}\mathcal{R}^{\mathrm{sw}}_{\mathrm{f}}(s\tilde{c}^{\mathrm{sw}}_{\mathrm{f},i} - c^{\mathrm{sw},0}_{\mathrm{f},i}) + \sum_{i=1}^{N^{\mathrm{aw}}_{\mathrm{f}}}\mathcal{R}^{\mathrm{aw}}_{\mathrm{f}}(s\tilde{c}^{\mathrm{aw}}_{\mathrm{f},i} - c^{\mathrm{aw},0}_{\mathrm{f},i}) = 0, \\ &s\tilde{c}^{\mathrm{sw}}_{\mathrm{f},i} - c^{\mathrm{sw},0}_{\mathrm{f},i} = \mathcal{A}^{\mathrm{sw}}_{\mathrm{f},i}\tilde{c}_{\mathrm{f}} - \mathcal{B}^{\mathrm{sw}}_{\mathrm{f},i}\tilde{c}^{\mathrm{sw}}_{\mathrm{f},i}, \quad i = 1, 2, \ldots, N^{\mathrm{sw}}_{\mathrm{f}}, \\ &s\tilde{c}^{\mathrm{aw}}_{\mathrm{f},i} - c^{\mathrm{aw},0}_{\mathrm{f},i} = \mathcal{A}^{\mathrm{aw}}_{\mathrm{f},i}\tilde{c}_{\mathrm{f}} - \mathcal{B}^{\mathrm{aw}}_{\mathrm{f},i}\tilde{c}^{\mathrm{aw}}_{\mathrm{f},i}, \quad i = 1, 2, \ldots, N^{\mathrm{aw}}_{\mathrm{f}}, \end{aligned} \tag{A.9}$$

$$\begin{aligned} &-\frac{1}{\mathcal{P}_{\mathrm{m}}}\frac{\partial^2 \tilde{c}_{\mathrm{m}}}{\partial Z^2} + \frac{\partial \tilde{c}_{\mathrm{m}}}{\partial Z} + \mathcal{R}_{\mathrm{m}}(s\tilde{c}_{\mathrm{m}} - c^0_{\mathrm{m}}) \pm \mathcal{U}_{\mathrm{m}}\tilde{c}_{\mathrm{p,m}} - \mathcal{K}_{\mathrm{m}}(\tilde{c}_{\mathrm{f}} - \tilde{c}_{\mathrm{m}}) \\ &+ \sum_{i=1}^{N^{\mathrm{sw}}_{\mathrm{m}}}\mathcal{R}^{\mathrm{sw}}_{\mathrm{m}}(s\tilde{c}^{\mathrm{sw}}_{\mathrm{m},i} - c^{\mathrm{sw},0}_{\mathrm{m},i}) + \sum_{i=1}^{N^{\mathrm{aw}}_{\mathrm{m}}}\mathcal{R}^{\mathrm{aw}}_{\mathrm{m}}(s\tilde{c}^{\mathrm{aw}}_{\mathrm{m},i} - c^{\mathrm{aw},0}_{\mathrm{m},i}) \\ &+ \sum_{i=1}^{N_{\mathrm{im}}}\mathcal{K}_{\mathrm{mim},i}(\tilde{c}_{\mathrm{m}} - \tilde{c}_{\mathrm{im},i}) = 0, \\ &s\tilde{c}^{\mathrm{sw}}_{\mathrm{m},i} - c^{\mathrm{sw},0}_{\mathrm{m},i} = \mathcal{A}^{\mathrm{sw}}_{\mathrm{m},i}\tilde{c}_{\mathrm{m}} - \mathcal{B}^{\mathrm{sw}}_{\mathrm{m},i}\tilde{c}^{\mathrm{sw}}_{\mathrm{m},i}, \quad i = 1, 2, \ldots, N^{\mathrm{sw}}_{\mathrm{m}}, \\ &s\tilde{c}^{\mathrm{aw}}_{\mathrm{m},i} - c^{\mathrm{aw},0}_{\mathrm{m},i} = \mathcal{A}^{\mathrm{aw}}_{\mathrm{m},i}\tilde{c}_{\mathrm{m}} - \mathcal{B}^{\mathrm{aw}}_{\mathrm{m},i}\tilde{c}^{\mathrm{aw}}_{\mathrm{m},i}, \quad i = 1, 2, \ldots, N^{\mathrm{aw}}_{\mathrm{m}}, \end{aligned} \tag{A.10}$$

and

$$\begin{aligned} &\mathcal{R}_{\mathrm{im},i}(s\tilde{c}_{\mathrm{im},i} - c^0_{\mathrm{im},i}) - \mathcal{K}_{\mathrm{im},i}(\tilde{c}_{\mathrm{m}} - \tilde{c}_{\mathrm{im},i}) \pm \mathcal{U}_{\mathrm{im},i}\tilde{c}_{\mathrm{p,im},i} \\ &+ \mathcal{R}^{\mathrm{sw}}_{\mathrm{im},i}(s\tilde{c}^{\mathrm{sw}}_{\mathrm{im},i} - c^{\mathrm{sw},0}_{\mathrm{im},i}) + \mathcal{R}^{\mathrm{aw}}_{\mathrm{im},i}(s\tilde{c}^{\mathrm{aw}}_{\mathrm{im},i} - c^{\mathrm{aw},0}_{\mathrm{im},i}) = 0, \\ &s\tilde{c}^{\mathrm{sw}}_{\mathrm{im},i} - c^{\mathrm{sw},0}_{\mathrm{im},i} = \mathcal{A}^{\mathrm{sw}}_{\mathrm{im},i}\tilde{c}_{\mathrm{im},i} - \mathcal{B}^{\mathrm{sw}}_{\mathrm{im},i}\tilde{c}^{\mathrm{sw}}_{\mathrm{im},i}, \\ &s\tilde{c}^{\mathrm{aw}}_{\mathrm{im},i} - c^{\mathrm{aw},0}_{\mathrm{im},i} = \mathcal{A}^{\mathrm{aw}}_{\mathrm{im},i}\tilde{c}_{\mathrm{im},i} - \mathcal{B}^{\mathrm{aw}}_{\mathrm{im},i}\tilde{c}^{\mathrm{aw}}_{\mathrm{im},i}, \end{aligned} \tag{A.11}$$

where $i = 1, 2, \ldots, N_{\mathrm{im}}$.

Eqs. (A.9)–(A.11) contains the following unknown variables: $\tilde{c}_{\mathrm{f}}$, $\tilde{c}^{\mathrm{sw}}_{\mathrm{f},i}$, $\tilde{c}^{\mathrm{aw}}_{\mathrm{f},i}$, $\tilde{c}_{\mathrm{m}}$, $\tilde{c}^{\mathrm{sw}}_{\mathrm{m},i}$, $\tilde{c}^{\mathrm{aw}}_{\mathrm{m},i}$, $\tilde{c}_{\mathrm{im},i}$, $\tilde{c}^{\mathrm{sw}}_{\mathrm{im},i}$ and $\tilde{c}^{\mathrm{aw}}_{\mathrm{im},i}$. We reduce the unknown variables to $\tilde{c}_{\mathrm{f}}$ and $\tilde{c}_{\mathrm{m}}$ through equation rearrangements and variable substitutions. In particular, we rearrange the equations for rate-limited solid-phase and air–water interfacial adsorption in Eqs. (A.9)–(A.11) to obtain the expression for $\tilde{c}^{\mathrm{sw}}_{\mathrm{f},i}$ and $\tilde{c}^{\mathrm{aw}}_{\mathrm{f},i}$ as functions of $\tilde{c}_{\mathrm{f}}$, the expression for $\tilde{c}^{\mathrm{sw}}_{\mathrm{m},i}$ and $\tilde{c}^{\mathrm{aw}}_{\mathrm{m},i}$ as functions of $\tilde{c}_{\mathrm{m}}$, and the expression for $\tilde{c}^{\mathrm{sw}}_{\mathrm{im},i}$ and $\tilde{c}^{\mathrm{aw}}_{\mathrm{im},i}$

as functions of $\tilde{c}_{\mathrm{im},i}$. Additionally, Eq. (A.11) is further rearranged to obtain the expression for $\tilde{c}_{\mathrm{im},i}$ as a function of $\tilde{c}_{\mathrm{m}}$. Finally, we substitute these expressions into Eqs. (A.9)–(A.10), which results in two equations where $\tilde{c}_{\mathrm{f}}$ and $\tilde{c}_{\mathrm{m}}$ are the only unknown variables

$$\begin{aligned} &-\frac{1}{\mathcal{P}_{\mathrm{f}}}\frac{\partial^2\tilde{c}_{\mathrm{f}}}{\partial Z^2}+\frac{\partial\tilde{c}_{\mathrm{f}}}{\partial Z}+h_{\mathrm{f}}(s)\tilde{c}_{\mathrm{f}}-\mathcal{K}_{\mathrm{f}}\tilde{c}_{\mathrm{m}}+h^0_{\mathrm{f}}(Z,s)=0,\\ &-\frac{1}{\mathcal{P}_{\mathrm{m}}}\frac{\partial^2\tilde{c}_{\mathrm{m}}}{\partial Z^2}+\frac{\partial\tilde{c}_{\mathrm{m}}}{\partial Z}+h_{\mathrm{m}}(s)\tilde{c}_{\mathrm{m}}-\mathcal{K}_{\mathrm{m}}\tilde{c}_{\mathrm{f}}+h^0_{\mathrm{m}}(Z,s)=0, \end{aligned} \tag{A.12}$$

where $h_{\mathrm{f}}(s)$, $h^0_{\mathrm{f}}(Z,s)$, $h_{\mathrm{m}}(s)$, and $h^0_{\mathrm{m}}(Z,s)$ are slightly different for PFAAs and precursors. For PFAAs, the equations are given by

$$\begin{aligned} h_{\mathrm{f}}(s)&=s\mathcal{R}_{\mathrm{f}}+\mathcal{K}_{\mathrm{f}}+s\left(\sum_{i=1}^{N_{\mathrm{f}}^{\mathrm{sw}}}\frac{\mathcal{A}^{\mathrm{sw}}_{\mathrm{f},i}\mathcal{R}^{\mathrm{sw}}_{\mathrm{f}}}{s+\mathcal{B}^{\mathrm{sw}}_{\mathrm{f},i}}+\sum_{i=1}^{N_{\mathrm{f}}^{\mathrm{aw}}}\frac{\mathcal{A}^{\mathrm{aw}}_{\mathrm{f},i}\mathcal{R}^{\mathrm{aw}}_{\mathrm{f}}}{s+\mathcal{B}^{\mathrm{aw}}_{\mathrm{f},i}}\right),\\ h^0_{\mathrm{f}}(Z,s)&=-\sum_{i=1}^{N_{\mathrm{f}}^{\mathrm{sw}}}\frac{\mathcal{B}^{\mathrm{sw}}_{\mathrm{f},i}\mathcal{R}^{\mathrm{sw}}_{\mathrm{f}}c^{\mathrm{sw},0}_{\mathrm{f},i}}{s+\mathcal{B}^{\mathrm{aw}}_{\mathrm{f},i}}-\sum_{i=1}^{N_{\mathrm{f}}^{\mathrm{aw}}}\frac{\mathcal{B}^{\mathrm{aw}}_{\mathrm{f},i}\mathcal{R}^{\mathrm{aw}}_{\mathrm{f}}c^{\mathrm{aw},0}_{\mathrm{f},i}}{s+\mathcal{B}^{\mathrm{aw}}_{\mathrm{f},i}}\\ &\quad-\mathcal{R}_{\mathrm{f}}c^0_{\mathrm{f}}-\mathcal{U}_{\mathrm{f}}\tilde{c}_{\mathrm{p,f}},\\ h_{\mathrm{m}}(s)&=s\mathcal{R}_{\mathrm{m}}+\mathcal{K}_{\mathrm{m}}+s\left(\sum_{i=1}^{N_{\mathrm{m}}^{\mathrm{sw}}}\frac{\mathcal{A}^{\mathrm{sw}}_{\mathrm{m},i}\mathcal{R}^{\mathrm{sw}}_{\mathrm{m}}}{s+\mathcal{B}^{\mathrm{sw}}_{\mathrm{m},i}}+\sum_{i=1}^{N_{\mathrm{m}}^{\mathrm{aw}}}\frac{\mathcal{A}^{\mathrm{aw}}_{\mathrm{m},i}\mathcal{R}^{\mathrm{aw}}_{\mathrm{m}}}{s+\mathcal{B}^{\mathrm{aw}}_{\mathrm{m},i}}\right)\\ &\quad+\sum_{i=1}^{N_{\mathrm{im}}}\mathcal{K}_{\mathrm{mim},i}\frac{s\mathcal{R}_{\mathrm{im},i}+\frac{s\mathcal{R}^{\mathrm{sw}}_{\mathrm{im},i}\mathcal{A}^{\mathrm{sw}}_{\mathrm{im},i}}{s+\mathcal{B}^{\mathrm{sw}}_{\mathrm{im},i}}+\frac{s\mathcal{R}^{\mathrm{aw}}_{\mathrm{im},i}\mathcal{A}^{\mathrm{aw}}_{\mathrm{im},i}}{s+\mathcal{B}^{\mathrm{aw}}_{\mathrm{im},i}}}{s\mathcal{R}_{\mathrm{im},i}+\mathcal{K}_{\mathrm{im},i}+\frac{s\mathcal{R}^{\mathrm{sw}}_{\mathrm{im},i}\mathcal{A}^{\mathrm{sw}}_{\mathrm{im},i}}{s+\mathcal{B}^{\mathrm{sw}}_{\mathrm{im},i}}+\frac{s\mathcal{R}^{\mathrm{aw}}_{\mathrm{im},i}\mathcal{A}^{\mathrm{aw}}_{\mathrm{im},i}}{s+\mathcal{B}^{\mathrm{aw}}_{\mathrm{im},i}}},\\ h^0_{\mathrm{m}}(Z,s)&=-\mathcal{R}_{\mathrm{m}}c^0_{\mathrm{m}}-\mathcal{U}_{\mathrm{m}}\tilde{c}_{\mathrm{p,m}}-\sum_{i=1}^{N_{\mathrm{im}}}\mathcal{K}_{\mathrm{mim},i}\\ &\quad\times\frac{\mathcal{R}_{\mathrm{im},i}c^0_{\mathrm{im},i}+\mathcal{U}_{\mathrm{im},i}\tilde{c}_{\mathrm{p,im},i}+\frac{\mathcal{R}^{\mathrm{aw}}_{\mathrm{im},i}\mathcal{B}^{\mathrm{aw}}_{\mathrm{im},i}c^{\mathrm{aw},0}_{\mathrm{im},i}}{s+\mathcal{B}^{\mathrm{aw}}_{\mathrm{im},i}}+\frac{\mathcal{R}^{\mathrm{sw}}_{\mathrm{im},i}\mathcal{B}^{\mathrm{sw}}_{\mathrm{im},i}c^{\mathrm{sw},0}_{\mathrm{im},i}}{s+\mathcal{B}^{\mathrm{sw}}_{\mathrm{im},i}}}{s\mathcal{R}_{\mathrm{im},i}+\mathcal{K}_{\mathrm{im},i}+\frac{s\mathcal{R}^{\mathrm{sw}}_{\mathrm{im},i}\mathcal{A}^{\mathrm{sw}}_{\mathrm{im},i}}{s+\mathcal{B}^{\mathrm{sw}}_{\mathrm{im},i}}+\frac{s\mathcal{R}^{\mathrm{aw}}_{\mathrm{im},i}\mathcal{A}^{\mathrm{aw}}_{\mathrm{im},i}}{s+\mathcal{B}^{\mathrm{aw}}_{\mathrm{im},i}}}\\ &\quad-\sum_{i=1}^{N_{\mathrm{m}}^{\mathrm{sw}}}\frac{\mathcal{R}^{\mathrm{sw}}_{\mathrm{m}}\mathcal{B}^{\mathrm{sw}}_{\mathrm{m},i}c^{\mathrm{sw},0}_{\mathrm{m},i}}{s+\mathcal{B}^{\mathrm{sw}}_{\mathrm{m},i}}-\sum_{i=1}^{N_{\mathrm{m}}^{\mathrm{aw}}}\frac{\mathcal{R}^{\mathrm{aw}}_{\mathrm{m}}\mathcal{B}^{\mathrm{aw}}_{\mathrm{m},i}c^{\mathrm{aw},0}_{\mathrm{m},i}}{s+\mathcal{B}^{\mathrm{aw}}_{\mathrm{m},i}}, \end{aligned} \tag{A.13}$$

where $\tilde{c}_{\mathrm{p,f}}$, $\tilde{c}_{\mathrm{p,m}}$, and $\tilde{c}_{\mathrm{p,im},i}$ are the Laplace-transformed concentrations of precursors in the fracture, mobile matrix, and immobile matrix domains, respectively. Eq. (A.13) applies to PFAAs either without or with mass sources from precursor transformation. If the equation is applied to PFAAs without transformation-induced mass sources, the relevant source terms are set to zero: $\mathcal{U}_{\mathrm{f}}=\mathcal{U}_{\mathrm{m}}=\mathcal{U}_{\mathrm{im},i}=0$. When transformation-induced sources are present, the precursor-related variables ($\tilde{c}_{\mathrm{p,f}}$, $\tilde{c}_{\mathrm{p,m}}$, and $\tilde{c}_{\mathrm{p,im},i}$) must first be solved via Equation (A.12) using precursor-associated parameters and functions (i.e., $h_{\mathrm{f}}(s)$, $h^0_{\mathrm{f}}(Z,s)$, $h_{\mathrm{m}}(s)$, and $h^0_{\mathrm{m}}(Z,s)$).

The precursor-associated functions are derived by setting $\tilde{c}_{\mathrm{p,f}}=\tilde{c}_{\mathrm{f}}$, $\tilde{c}_{\mathrm{p,m}}=\tilde{c}_{\mathrm{m}}$, and $\tilde{c}_{\mathrm{p,im},i}=\tilde{c}_{\mathrm{im},i}$, which yields

$$\begin{aligned} h_{\mathrm{f}}(s)&=s\mathcal{R}_{\mathrm{f}}+\mathcal{K}_{\mathrm{f}}+\mathcal{U}_{\mathrm{f}}+s\left(\sum_{i=1}^{N_{\mathrm{f}}^{\mathrm{sw}}}\frac{\mathcal{A}^{\mathrm{sw}}_{\mathrm{f},i}\mathcal{R}^{\mathrm{sw}}_{\mathrm{f}}}{s+\mathcal{B}^{\mathrm{sw}}_{\mathrm{f},i}}+\sum_{i=1}^{N_{\mathrm{f}}^{\mathrm{aw}}}\frac{\mathcal{A}^{\mathrm{aw}}_{\mathrm{f},i}\mathcal{R}^{\mathrm{aw}}_{\mathrm{f}}}{s+\mathcal{B}^{\mathrm{aw}}_{\mathrm{f},i}}\right),\\ h^0_{\mathrm{f}}(Z,s)&=-\mathcal{R}_{\mathrm{f}}c^0_{\mathrm{f}}-\sum_{i=1}^{N_{\mathrm{f}}^{\mathrm{sw}}}\frac{\mathcal{R}^{\mathrm{sw}}_{\mathrm{f}}\mathcal{B}^{\mathrm{sw}}_{\mathrm{f},i}c^{\mathrm{sw},0}_{\mathrm{f},i}}{s+\mathcal{B}^{\mathrm{sw}}_{\mathrm{f},i}}-\sum_{i=1}^{N_{\mathrm{f}}^{\mathrm{aw}}}\frac{\mathcal{R}^{\mathrm{aw}}_{\mathrm{f}}\mathcal{B}^{\mathrm{aw}}_{\mathrm{f},i}c^{\mathrm{aw},0}_{\mathrm{f},i}}{s+\mathcal{B}^{\mathrm{aw}}_{\mathrm{f},i}},\\ h_{\mathrm{m}}(s)&=s\mathcal{R}_{\mathrm{m}}+\mathcal{K}_{\mathrm{m}}+\mathcal{U}_{\mathrm{m}}+s\left(\sum_{i=1}^{N_{\mathrm{m}}^{\mathrm{sw}}}\frac{\mathcal{A}^{\mathrm{sw}}_{\mathrm{m},i}\mathcal{R}^{\mathrm{sw}}_{\mathrm{m}}}{s+\mathcal{B}^{\mathrm{sw}}_{\mathrm{m},i}}+\sum_{i=1}^{N_{\mathrm{m}}^{\mathrm{aw}}}\frac{\mathcal{A}^{\mathrm{aw}}_{\mathrm{m},i}\mathcal{R}^{\mathrm{aw}}_{\mathrm{m}}}{s+\mathcal{B}^{\mathrm{aw}}_{\mathrm{m},i}}\right)\\ &\quad+\sum_{i=1}^{N_{\mathrm{im}}}\mathcal{K}_{\mathrm{mim},i}\frac{s\mathcal{R}_{\mathrm{im},i}+\mathcal{U}_{\mathrm{im},i}+\frac{s\mathcal{R}^{\mathrm{sw}}_{\mathrm{im},i}\mathcal{A}^{\mathrm{sw}}_{\mathrm{im},i}}{s+\mathcal{B}^{\mathrm{sw}}_{\mathrm{im},i}}+\frac{s\mathcal{R}^{\mathrm{aw}}_{\mathrm{im},i}\mathcal{A}^{\mathrm{aw}}_{\mathrm{im},i}}{s+\mathcal{B}^{\mathrm{aw}}_{\mathrm{im},i}}}{s\mathcal{R}_{\mathrm{im},i}+\mathcal{K}_{\mathrm{im},i}+\mathcal{U}_{\mathrm{im},i}+\frac{s\mathcal{R}^{\mathrm{sw}}_{\mathrm{im},i}\mathcal{A}^{\mathrm{sw}}_{\mathrm{im},i}}{s+\mathcal{B}^{\mathrm{sw}}_{\mathrm{im},i}}+\frac{s\mathcal{R}^{\mathrm{aw}}_{\mathrm{im},i}\mathcal{A}^{\mathrm{aw}}_{\mathrm{im},i}}{s+\mathcal{B}^{\mathrm{aw}}_{\mathrm{im},i}}},\\ h^0_{\mathrm{m}}(Z,s)&=-\mathcal{R}_{\mathrm{m}}c^0_{\mathrm{m}}-\sum_{i=1}^{N_{\mathrm{m}}^{\mathrm{sw}}}\frac{\mathcal{R}^{\mathrm{sw}}_{\mathrm{m}}\mathcal{B}^{\mathrm{sw}}_{\mathrm{m},i}c^{\mathrm{sw},0}_{\mathrm{m},i}}{s+\mathcal{B}^{\mathrm{sw}}_{\mathrm{m},i}}-\sum_{i=1}^{N_{\mathrm{m}}^{\mathrm{aw}}}\frac{\mathcal{R}^{\mathrm{aw}}_{\mathrm{m}}\mathcal{B}^{\mathrm{aw}}_{\mathrm{m},i}c^{\mathrm{aw},0}_{\mathrm{m},i}}{s+\mathcal{B}^{\mathrm{aw}}_{\mathrm{m},i}}\\ &\quad-\sum_{i=1}^{N_{\mathrm{im}}}\mathcal{K}_{\mathrm{mim},i}\frac{\mathcal{R}_{\mathrm{im},i}c^0_{\mathrm{im},i}+\frac{\mathcal{R}^{\mathrm{aw}}_{\mathrm{im},i}\mathcal{B}^{\mathrm{aw}}_{\mathrm{im},i}c^{\mathrm{aw},0}_{\mathrm{im},i}}{s+\mathcal{B}^{\mathrm{aw}}_{\mathrm{im},i}}+\frac{\mathcal{R}^{\mathrm{sw}}_{\mathrm{im},i}\mathcal{B}^{\mathrm{sw}}_{\mathrm{im},i}c^{\mathrm{sw},0}_{\mathrm{im},i}}{s+\mathcal{B}^{\mathrm{sw}}_{\mathrm{im},i}}}{s\mathcal{R}_{\mathrm{im},i}+\mathcal{K}_{\mathrm{im},i}+\mathcal{U}_{\mathrm{im},i}+\frac{s\mathcal{R}^{\mathrm{sw}}_{\mathrm{im},i}\mathcal{A}^{\mathrm{sw}}_{\mathrm{im},i}}{s+\mathcal{B}^{\mathrm{sw}}_{\mathrm{im},i}}+\frac{s\mathcal{R}^{\mathrm{aw}}_{\mathrm{im},i}\mathcal{A}^{\mathrm{aw}}_{\mathrm{im},i}}{s+\mathcal{B}^{\mathrm{aw}}_{\mathrm{im},i}}}. \end{aligned} \tag{A.14}$$

Eq. (A.12) and Eq. (A.13) are used for PFAAs, while Eq. (A.12) and Eq. (A.14) are used for precursors. They can be solved following the same procedure hereafter. The next step is to take the Laplace transform of Eq. (A.12) in space, which yields

$$\begin{aligned} &-\frac{1}{\mathcal{P}_{\mathrm{f}}}\left(r^2\hat{\tilde{c}}_{\mathrm{f}}-r\tilde{c}_{\mathrm{f}}|_{Z=0}-\frac{\partial\tilde{c}_{\mathrm{f}}}{\partial Z}|_{Z=0}\right)+r\hat{\tilde{c}}_{\mathrm{f}}-\tilde{c}_{\mathrm{f}}|_{Z=0}\\ &\qquad+h_{\mathrm{f}}(s)\hat{\tilde{c}}_{\mathrm{f}}-\mathcal{K}_{\mathrm{f}}\hat{\tilde{c}}_{\mathrm{m}}=-\hat{h}^0_{\mathrm{f}}(r,s),\\ &-\frac{1}{\mathcal{P}_{\mathrm{m}}}\left(r^2\hat{\tilde{c}}_{\mathrm{m}}-r\tilde{c}_{\mathrm{m}}|_{Z=0}-\frac{\partial\tilde{c}_{\mathrm{m}}}{\partial Z}|_{Z=0}\right)+r\hat{\tilde{c}}_{\mathrm{m}}-\tilde{c}_{\mathrm{m}}|_{Z=0}\\ &\qquad+h_{\mathrm{m}}(s)\hat{\tilde{c}}_{\mathrm{m}}-\mathcal{K}_{\mathrm{m}}\hat{\tilde{c}}_{\mathrm{f}}=-\hat{h}^0_{\mathrm{m}}(r,s). \end{aligned} \tag{A.15}$$

In Eq. (A.15), $\tilde{c}_{\mathrm{f}}|_{Z=0}$, $\tilde{c}_{\mathrm{m}}|_{Z=0}$, $\frac{\partial\tilde{c}_{\mathrm{f}}}{\partial Z}|_{Z=0}$, and $\frac{\partial\tilde{c}_{\mathrm{m}}}{\partial Z}|_{Z=0}$ remain unknown. We first eliminate $\frac{\partial\tilde{c}_{\mathrm{f}}}{\partial Z}|_{Z=0}$ and $\frac{\partial\tilde{c}_{\mathrm{m}}}{\partial Z}|_{Z=0}$ using the boundary conditions at $Z=0$ (see Eq. (A.4)). To do so, we first take the Laplace transform of Eq. (A.4) in time, which gives

$$\left[-\frac{1}{\mathcal{P}_{\mathrm{f}}}\frac{\partial\tilde{c}_{\mathrm{f}}}{\partial Z}+\tilde{c}_{\mathrm{f}}\right]_{Z=0}=\tilde{c}_{\mathrm{f,in}},\quad\&\quad\left[-\frac{1}{\mathcal{P}_{\mathrm{m}}}\frac{\partial\tilde{c}_{\mathrm{m}}}{\partial Z}+\tilde{c}_{\mathrm{m}}\right]_{Z=0}=\tilde{c}_{\mathrm{m,in}}. \tag{A.16}$$

Then we cast Equation (A.16) back in Eq. (A.15), which yields

$$\begin{aligned} \left(-\frac{1}{\mathcal{P}_{\mathrm{f}}}r^2+r+h_{\mathrm{f}}(s)\right)\hat{\tilde{c}}_{\mathrm{f}}-\mathcal{K}_{\mathrm{f}}\hat{\tilde{c}}_{\mathrm{m}}&=-\frac{r}{\mathcal{P}_{\mathrm{f}}}\tilde{c}_{\mathrm{f}}|_{Z=0}+\tilde{c}_{\mathrm{f,in}}-\hat{h}^0_{\mathrm{f}}(r,s),\\ \left(-\frac{1}{\mathcal{P}_{\mathrm{m}}}r^2+r+h_{\mathrm{m}}(s)\right)\hat{\tilde{c}}_{\mathrm{m}}-\mathcal{K}_{\mathrm{m}}\hat{\tilde{c}}_{\mathrm{f}}&=-\frac{r}{\mathcal{P}_{\mathrm{m}}}\tilde{c}_{\mathrm{m}}|_{Z=0}+\tilde{c}_{\mathrm{m,in}}-\hat{h}^0_{\mathrm{m}}(r,s). \end{aligned} \tag{A.17}$$

Solving Equation (A.17) yields,

$$\begin{aligned} \hat{\tilde{c}}_{\mathrm{f}}&=\frac{\left(r^2-\mathcal{P}_{\mathrm{m}}r-\mathcal{P}_{\mathrm{m}}h_{\mathrm{m}}(s)\right)\left(r\tilde{c}_{\mathrm{f}}|_{Z=0}-\mathcal{P}_{\mathrm{f}}\tilde{c}_{\mathrm{f,in}}+\mathcal{P}_{\mathrm{f}}\hat{h}^0{}_{\mathrm{f}}(r,s)\right)}{\left(r^2-\mathcal{P}_{\mathrm{f}}r-\mathcal{P}_{\mathrm{f}}h_{\mathrm{f}}(s)\right)\left(r^2-\mathcal{P}_{\mathrm{m}}r-\mathcal{P}_{\mathrm{m}}h_{\mathrm{m}}(s)\right)-\mathcal{P}_{\mathrm{f}}\mathcal{K}_{\mathrm{f}}\mathcal{P}_{\mathrm{m}}\mathcal{K}_{\mathrm{m}}}\\ &\quad-\frac{\mathcal{P}_{\mathrm{f}}\mathcal{K}_{\mathrm{f}}\left(r\tilde{c}_{\mathrm{m}}|_{Z=0}-\mathcal{P}_{\mathrm{m}}\tilde{c}_{\mathrm{m,in}}+\mathcal{P}_{\mathrm{m}}\hat{h}^0_{\mathrm{m}}(r,s)\right)}{\left(r^2-\mathcal{P}_{\mathrm{f}}r-\mathcal{P}_{\mathrm{f}}h_{\mathrm{f}}(s)\right)\left(r^2-\mathcal{P}_{\mathrm{m}}r-\mathcal{P}_{\mathrm{m}}h_{\mathrm{m}}(s)\right)-\mathcal{P}_{\mathrm{f}}\mathcal{K}_{\mathrm{f}}\mathcal{P}_{\mathrm{m}}\mathcal{K}_{\mathrm{m}}},\\ \hat{\tilde{c}}_{\mathrm{m}}&=-\frac{\mathcal{P}_{\mathrm{m}}\mathcal{K}_{\mathrm{m}}\left(r\tilde{c}_{\mathrm{f}}|_{Z=0}-\mathcal{P}_{\mathrm{f}}\tilde{c}_{\mathrm{f,in}}+\mathcal{P}_{\mathrm{f}}\hat{h}^0{}_{\mathrm{f}}(r,s)\right)}{\left(r^2-\mathcal{P}_{\mathrm{f}}r-\mathcal{P}_{\mathrm{f}}h_{\mathrm{f}}(s)\right)\left(r^2-\mathcal{P}_{\mathrm{m}}r-\mathcal{P}_{\mathrm{m}}h_{\mathrm{m}}(s)\right)-\mathcal{P}_{\mathrm{f}}\mathcal{K}_{\mathrm{f}}\mathcal{P}_{\mathrm{m}}\mathcal{K}_{\mathrm{m}}}\\ &\quad+\frac{\left(r^2-\mathcal{P}_{\mathrm{f}}r-\mathcal{P}_{\mathrm{f}}h_{\mathrm{f}}(s)\right)\left(r\tilde{c}_{\mathrm{m}}|_{Z=0}-\mathcal{P}_{\mathrm{m}}\tilde{c}_{\mathrm{m,in}}+\mathcal{P}_{\mathrm{m}}\hat{h}^0_{\mathrm{m}}(r,s)\right)}{\left(r^2-\mathcal{P}_{\mathrm{f}}r-\mathcal{P}_{\mathrm{f}}h_{\mathrm{f}}(s)\right)\left(r^2-\mathcal{P}_{\mathrm{m}}r-\mathcal{P}_{\mathrm{m}}h_{\mathrm{m}}(s)\right)-\mathcal{P}_{\mathrm{f}}\mathcal{K}_{\mathrm{f}}\mathcal{P}_{\mathrm{m}}\mathcal{K}_{\mathrm{m}}}. \end{aligned} \tag{A.18}$$

Suppose $\left(r^2-\mathcal{P}_{\mathrm{f}}r-\mathcal{P}_{\mathrm{f}}h_{\mathrm{f}}(s)\right)\left(r^2-\mathcal{P}_{\mathrm{m}}r-\mathcal{P}_{\mathrm{m}}h_{\mathrm{m}}(s)\right)-\mathcal{P}_{\mathrm{f}}\mathcal{K}_{\mathrm{f}}\mathcal{P}_{\mathrm{m}}\mathcal{K}_{\mathrm{m}}=\Pi_{i=1}^4(r-r_i)$. We can factorize all the terms in Eq. (A.18) by

$$\begin{aligned} \hat{\tilde{c}}_{\mathrm{f}}&=\tilde{c}_{\mathrm{f}}|_{Z=0}\sum_{i=1}^{4}\frac{C_{4,i}-C_{3,i}\mathcal{P}_{\mathrm{m}}-C_{2,i}\mathcal{P}_{\mathrm{m}}h_{\mathrm{m}}(s)}{r-r_i}-\tilde{c}_{\mathrm{m}}|_{Z=0}\sum_{i=1}^{4}\frac{C_{2,i}\mathcal{P}_{\mathrm{f}}\mathcal{K}_{\mathrm{f}}}{r-r_i}\\ &\quad+\sum_{i=1}^{4}\frac{\left(C_{3,i}-C_{2,i}\mathcal{P}_{\mathrm{m}}-C_{1,i}\mathcal{P}_{\mathrm{m}}h_{\mathrm{m}}(s)\right)\left(-\mathcal{P}_{\mathrm{f}}\tilde{c}_{\mathrm{f,in}}+\mathcal{P}_{\mathrm{f}}\hat{h}^0_{\mathrm{f}}(r,s)\right)}{r-r_i}\\ &\quad-\sum_{i=1}^{4}\frac{C_{1,i}\mathcal{P}_{\mathrm{f}}\mathcal{K}_{\mathrm{f}}\left(-\mathcal{P}_{\mathrm{m}}\tilde{c}_{\mathrm{m,in}}+\mathcal{P}_{\mathrm{m}}\hat{h}^0_{\mathrm{m}}(r,s)\right)}{r-r_i},\\ \hat{\tilde{c}}_{\mathrm{m}}&=-\tilde{c}_{\mathrm{f}}|_{Z=0}\sum_{i=1}^{4}\frac{C_{2,i}\mathcal{P}_{\mathrm{m}}\mathcal{K}_{\mathrm{m}}}{r-r_i}+\tilde{c}_{\mathrm{m}}|_{Z=0}\sum_{i=1}^{4}\frac{C_{4,i}-C_{3,i}\mathcal{P}_{\mathrm{f}}-C_{2,i}\mathcal{P}_{\mathrm{f}}h_{\mathrm{f}}(s)}{r-r_i}\\ &\quad-\sum_{i=1}^{4}\frac{C_{1,i}\mathcal{P}_{\mathrm{m}}\mathcal{K}_{\mathrm{m}}\left(-\mathcal{P}_{\mathrm{f}}\tilde{c}_{\mathrm{f,in}}+\mathcal{P}_{\mathrm{f}}\hat{h}^0{}_{\mathrm{f}}(r,s)\right)}{r-r_i}\\ &\quad+\sum_{i=1}^{4}\frac{\left(C_{3,i}-C_{2,i}\mathcal{P}_{\mathrm{f}}-C_{1,i}\mathcal{P}_{\mathrm{f}}h_{\mathrm{f}}(s)\right)\left(-\mathcal{P}_{\mathrm{m}}\tilde{c}_{\mathrm{m,in}}+\mathcal{P}_{\mathrm{m}}\hat{h}^0_{\mathrm{m}}(r,s)\right)}{r-r_i}, \end{aligned} \tag{A.19}$$

where $C_{j,i}$ $(j = 1, 2, 3, 4)$ are coefficients that are independent of $r$ and satisfy $\sum_{i=1}^{4} C_{j,i}/(r - r_i) = r^{j-1}/\Pi_{i=1}^{4}(r - r_i)$.

In Eq. (A.19), $\tilde{c}_\mathrm{f}|_{Z=0}$ and $\tilde{c}_\mathrm{m}|_{Z=0}$ remain unknown and they need to be solved using the boundary conditions at $Z = \infty$, which will be discussed in Appendix A.4.

### A.4. Inverse Laplace transform

We solve the physical aqueous concentrations ($c_\mathrm{f}$ and $c_\mathrm{m}$) through the inverse Laplace transform. The inverse Laplace transform of Eq. (A.19) is

$$
\begin{aligned}
\tilde{c}_\mathrm{f} =& \tilde{c}_\mathrm{f}|_{Z=0} \sum_{i=1}^{4} \left(C_{4,i} - C_{3,i}\mathcal{P}_\mathrm{m} - C_{2,i}\mathcal{P}_\mathrm{m} h_\mathrm{m}(s)\right) \exp\left(r_i Z\right) \\
& - \tilde{c}_\mathrm{m}|_{Z=0} \mathcal{P}_\mathrm{f}\mathcal{K}_\mathrm{f} \sum_{i=1}^{4} C_{2,i} \exp\left(r_i Z\right) \\
& - \mathcal{P}_\mathrm{f}\tilde{c}_{\mathrm{f,in}} \sum_{i=1}^{4} \left(C_{3,i} - C_{2,i}\mathcal{P}_\mathrm{m} - C_{1,i}\mathcal{P}_\mathrm{m} h_\mathrm{m}(s)\right) \exp\left(r_i Z\right) \\
& + \mathcal{P}_\mathrm{f} \sum_{i=1}^{4} \left(C_{3,i} - C_{2,i}\mathcal{P}_\mathrm{m} - C_{1,i}\mathcal{P}_\mathrm{m} h_\mathrm{m}(s)\right) \int_0^Z h_\mathrm{f}^0(z', s) \exp\left(r_i(Z - z')\right) dz' \\
& + \mathcal{P}_\mathrm{f}\mathcal{K}_\mathrm{f}\mathcal{P}_\mathrm{m}\tilde{c}_{\mathrm{m,in}} \sum_{i=1}^{4} C_{1,i} \exp\left(r_i Z\right) \\
& - \mathcal{P}_\mathrm{f}\mathcal{K}_\mathrm{f}\mathcal{P}_\mathrm{m} \sum_{i=1}^{4} C_{1,i} \int_0^Z h_\mathrm{m}^0(z', s) \exp\left(r_i(Z - z')\right) dz', \\
\tilde{c}_\mathrm{m} =& - \tilde{c}_\mathrm{f}|_{Z=0} \mathcal{P}_\mathrm{m}\mathcal{K}_\mathrm{m} \sum_{i=1}^{4} C_{2,i} \exp\left(r_i Z\right) \\
& + \tilde{c}_\mathrm{m}|_{Z=0} \sum_{i=1}^{4} \left(C_{4,i} - C_{3,i}\mathcal{P}_\mathrm{f} - C_{2,i}\mathcal{P}_\mathrm{f} h_\mathrm{f}(s)\right) \exp\left(r_i Z\right) \\
& + \mathcal{P}_\mathrm{m}\mathcal{K}_\mathrm{m}\mathcal{P}_\mathrm{f}\tilde{c}_{\mathrm{f,in}} \sum_{i=1}^{4} C_{1,i} \exp\left(r_i Z\right) \\
& - \mathcal{P}_\mathrm{m}\mathcal{K}_\mathrm{m}\mathcal{P}_\mathrm{f} \sum_{i=1}^{4} C_{1,i} \int_0^Z h_\mathrm{f}^0(z', s) \exp\left(r_i(Z - z')\right) dz' \\
& - \mathcal{P}_\mathrm{m}\tilde{c}_{\mathrm{m,in}} \sum_{i=1}^{4} \left(C_{3,i} - C_{2,i}\mathcal{P}_\mathrm{f} - C_{1,i}\mathcal{P}_\mathrm{f} h_\mathrm{f}(s)\right) \exp\left(r_i Z\right) \\
& + \mathcal{P}_\mathrm{m} \sum_{i=1}^{4} \left(C_{3,i} - C_{2,i}\mathcal{P}_\mathrm{f} - C_{1,i}\mathcal{P}_\mathrm{f} h_\mathrm{f}(s)\right) \int_0^Z h_\mathrm{m}^0(z', s) \exp\left(r_i(Z - z')\right) dz',
\end{aligned}
\tag{A.20}
$$

where $\tilde{c}_\mathrm{f}|_{Z=0}$ and $\tilde{c}_\mathrm{m}|_{Z=0}$ need to be solved using the boundary conditions at $Z = \infty$ (see Eq. (A.4)). To simplify the calculations, we further define the following equations,

$$
\begin{aligned}
g_{\mathrm{f},i}(s) &= C_{4,i} - C_{3,i}\mathcal{P}_\mathrm{f} - C_{2,i}\mathcal{P}_\mathrm{f} h_\mathrm{f}(s), \\
g_{\mathrm{m},i}(s) &= C_{4,i} - C_{3,i}\mathcal{P}_\mathrm{m} - C_{2,i}\mathcal{P}_\mathrm{m} h_\mathrm{m}(s), \\
g_\mathrm{f}(Z, s) &= -\mathcal{P}_\mathrm{f}\tilde{c}_{\mathrm{f,in}} \sum_{i=1}^{4} \left(C_{3,i} - C_{2,i}\mathcal{P}_\mathrm{m} - C_{1,i}\mathcal{P}_\mathrm{m} h_\mathrm{m}(s)\right) \exp\left(r_i Z\right) \\
&\quad + \mathcal{P}_\mathrm{f} \sum_{i=1}^{4} \left(C_{3,i} - C_{2,i}\mathcal{P}_\mathrm{m} - C_{1,i}\mathcal{P}_\mathrm{m} h_\mathrm{m}(s)\right) \\
&\quad \times \int_0^Z h_\mathrm{f}^0(z', s) \exp\left(r_i(Z - z')\right) dz' \\
&\quad + \mathcal{P}_\mathrm{f}\mathcal{K}_\mathrm{f}\mathcal{P}_\mathrm{m}\tilde{c}_{\mathrm{m,in}} \sum_{i=1}^{4} C_{1,i} \exp\left(r_i Z\right) \\
&\quad - \mathcal{P}_\mathrm{f}\mathcal{K}_\mathrm{f}\mathcal{P}_\mathrm{m} \sum_{i=1}^{4} C_{1,i} \int_0^Z h_\mathrm{m}^0(z', s) \exp\left(r_i(Z - z')\right) dz', \\
g_\mathrm{m}(Z, s) &= \mathcal{P}_\mathrm{m}\mathcal{K}_\mathrm{m}\mathcal{P}_\mathrm{f}\tilde{c}_{\mathrm{f,in}} \sum_{i=1}^{4} C_{1,i} \exp\left(r_i Z\right) \\
&\quad - \mathcal{K}_\mathrm{m}\mathcal{P}_\mathrm{m}\mathcal{P}_\mathrm{f} \sum_{i=1}^{4} C_{1,i} \int_0^Z h_\mathrm{f}^0(z', s) \exp\left(r_i(Z - z')\right) dz' \\
&\quad - \mathcal{P}_\mathrm{m}\tilde{c}_{\mathrm{m,in}} \sum_{i=1}^{4} \left(C_{3,i} - C_{2,i}\mathcal{P}_\mathrm{f} - C_{1,i}\mathcal{P}_\mathrm{f} h_\mathrm{f}(s)\right) \exp\left(r_i Z\right) \\
&\quad + \mathcal{P}_\mathrm{m} \sum_{i=1}^{4} \left(C_{3,i} - C_{2,i}\mathcal{P}_\mathrm{f} - C_{1,i}\mathcal{P}_\mathrm{f} h_\mathrm{f}(s)\right) \\
&\quad \times \int_0^Z h_\mathrm{m}^0(z', s) \exp\left(r_i(Z - z')\right) dz'.
\end{aligned}
\tag{A.21}
$$

Accordingly, Eq. (A.20) can be written as

$$
\begin{aligned}
\tilde{c}_\mathrm{f} =& \tilde{c}_\mathrm{f}|_{Z=0} \sum_{i=1}^{4} g_{\mathrm{m},i}(s) \exp\left(r_i Z\right) \\
& - \tilde{c}_\mathrm{m}|_{Z=0} \mathcal{P}_\mathrm{f}\mathcal{K}_\mathrm{f} \sum_{i=1}^{4} C_{2,i} \exp\left(r_i Z\right) + g_\mathrm{f}(Z, s), \\
\tilde{c}_\mathrm{m} =& - \tilde{c}_\mathrm{f}|_{Z=0} \mathcal{P}_\mathrm{m}\mathcal{K}_\mathrm{m} \sum_{i=1}^{4} C_{2,i} \exp\left(r_i Z\right) \\
& + \tilde{c}_\mathrm{m}|_{Z=0} \sum_{i=1}^{4} g_{\mathrm{f},i}(s) \exp\left(r_i Z\right) + g_\mathrm{m}(Z, s).
\end{aligned}
\tag{A.22}
$$

Applying the boundary condition at $Z = \infty$ (see Eq. (A.4)) results in

$$
\begin{aligned}
\lim_{Z=\infty} \frac{\partial \tilde{c}_\mathrm{f}}{\partial Z} =& \tilde{c}_\mathrm{f}|_{Z=0} \lim_{Z=\infty} \sum_{i=1}^{4} g_{\mathrm{m},i}(s) r_i \exp\left(r_i Z\right) \\
& - \tilde{c}_\mathrm{m}|_{Z=0} \mathcal{P}_\mathrm{f}\mathcal{K}_\mathrm{f} \lim_{Z=\infty} \sum_{i=1}^{4} C_{2,i} r_i \exp\left(r_i Z\right) \\
& + \lim_{Z=\infty} \frac{\partial g_\mathrm{f}(Z, s)}{\partial Z} \\
=& 0, \\
\lim_{Z=\infty} \frac{\partial \tilde{c}_\mathrm{m}}{\partial Z} =& - \tilde{c}_\mathrm{f}|_{Z=0} \mathcal{P}_\mathrm{m}\mathcal{K}_\mathrm{m} \lim_{Z=\infty} \sum_{i=1}^{4} C_{2,i} r_i \exp\left(r_i Z\right) \\
& + \tilde{c}_\mathrm{m}|_{Z=0} \lim_{Z=\infty} \sum_{i=1}^{4} g_{\mathrm{f},i}(s) r_i \exp\left(r_i Z\right) \\
& + \lim_{Z=\infty} \frac{\partial g_\mathrm{m}(Z, s)}{\partial Z} \\
=& 0.
\end{aligned}
\tag{A.23}
$$

Eq. (A.23) contains both decaying (i.e., $\exp(r_i Z)$ where $r_i$ has a negative real part) and growing (i.e., $\exp(r_i Z)$ where $r_i$ has a positive real part) exponential terms. As $Z \to \infty$, all the decaying terms vanish. After these terms are eliminated, the remaining growing terms still involve the unknown $\tilde{c}_\mathrm{f}|_{Z=0}$ and $\tilde{c}_\mathrm{m}|_{Z=0}$. To ensure that $\tilde{c}_\mathrm{f}(Z, s)$ and $\tilde{c}_\mathrm{m}(Z, s)$ remain bounded, the coefficients of the growing terms must be set to zero. These constraints yield a linear system, which can be directly solved to obtain $\tilde{c}_\mathrm{f}|_{Z=0}$ and $\tilde{c}_\mathrm{m}|_{Z=0}$.

Finally, we can substitute the solved $\tilde{c}_\mathrm{f}|_{Z=0}$ and $\tilde{c}_\mathrm{m}|_{Z=0}$ into Eq. (A.22) for computing $\tilde{c}_\mathrm{f}$ and $\tilde{c}_\mathrm{m}$, which are nonlinear functions of the Laplace variable $s$. We can then perform inverse Laplace transform on $\tilde{c}_\mathrm{f}$ and $\tilde{c}_\mathrm{m}$ to compute the spatial and temporal variations of aqueous PFAS concentrations in the fracture domain $c_\mathrm{f}$ and matrix domain $c_\mathrm{m}$ using numerical approximation methods reported by Durbin (1974), Crump (1976), and De Hoog et al. (1982). Note that the accuracy of these numerical approximations may depend on the model parameters (Honig and Hirdes, 1984) and the specific flow and transport conditions. For conditions where the errors become significant, more advanced numerical approximation methods can be adopted (Du et al., 2017).

## Appendix B. Semi-analytical solutions for single-porosity and dual-porosity models

We derive the semi-analytical solutions for the single-porosity and dual-porosity models using the Laplace transform and inverse Laplace transform. Because the two models share the same procedure, the more involved dual-porosity model formulations are used to illustrate the general derivations. One can remove all the terms related to the (immobile) matrix domain to obtain the solutions for the single-porosity model and repeat the following procedures. The derivations for PFAAs and precursors are almost the same, except for one derivation step right after taking the Laplace transform of the governing equations in time. We explain the difference in the Laplace transform (Appendix B.4).

### B.1. Governing equations

The governing equation for PFAS transport in the fracture domain of the dual-porosity model is similar to that of the triple-porosity model (Eq. (2)), except that the fracture domain exchanges mass directly with the matrix domain where all of the water is immobile. The equation is given by

$$\theta_{\mathrm{f}} R_{\mathrm{f}} \frac{\partial c_{\mathrm{f}}}{\partial t} + \theta_{\mathrm{f}} v_{\mathrm{f}} \frac{\partial c_{\mathrm{f}}}{\partial z} - \theta_{\mathrm{f}} D_{\mathrm{f}} \frac{\partial^2 c_{\mathrm{f}}}{\partial z^2} \pm \theta_{\mathrm{f}} \mu_{\mathrm{f}} c_{\mathrm{p,f}} + \frac{w_{\mathrm{im}}}{w_{\mathrm{f}}} \sum_{i=1}^{N_{\mathrm{im}}} w_{\mathrm{im},i} \kappa_{\mathrm{f,im},i} \left(c_{\mathrm{f}} - c_{\mathrm{im},i}\right) + \sum_{i=1}^{N_{\mathrm{f}}^{\mathrm{sw}}} \rho_{\mathrm{f}} \frac{\partial c_{\mathrm{f},i}^{\mathrm{sw}}}{\partial t} + \sum_{i=1}^{N_{\mathrm{f}}^{\mathrm{aw}}} A_{\mathrm{f}}^{\mathrm{aw}} \frac{\partial c_{\mathrm{f},i}^{\mathrm{aw}}}{\partial t} = 0. \tag{B.1}$$

The PFAS concentrations at the solid–water and air–water interfaces follow the same governing equations as the triple-porosity model,

$$\begin{aligned} \frac{\partial c_{\mathrm{f},i}^{\mathrm{sw}}}{\partial t} &= \kappa_{\mathrm{f},i}^{\mathrm{sw}} \left[ f_{\mathrm{f},i}^{\mathrm{sw}} (1 - F_{\mathrm{f,eq}}^{\mathrm{sw}}) K_{\mathrm{f}}^{\mathrm{sw}} c_{\mathrm{f}} - c_{\mathrm{f},i}^{\mathrm{sw}} \right], \\ \frac{\partial c_{\mathrm{f},i}^{\mathrm{aw}}}{\partial t} &= \kappa_{\mathrm{f},i}^{\mathrm{aw}} \left[ f_{\mathrm{f},i}^{\mathrm{aw}} \left(1 - F_{\mathrm{f,eq}}^{\mathrm{aw}}\right) K_{\mathrm{f}}^{\mathrm{aw}} c_{\mathrm{f}} - c_{\mathrm{f},i}^{\mathrm{aw}} \right]. \end{aligned} \tag{B.2}$$

Similarly, the (immobile) matrix domain directly exchanges mass with the fracture domain. The aqueous PFAS concentration in each $i^{\mathrm{th}}$ immobile matrix domain is controlled by

$$\theta_{\mathrm{im},i} R_{\mathrm{im},i} \frac{\partial c_{\mathrm{im},i}}{\partial t} - \kappa_{\mathrm{f,im},i} (c_{\mathrm{f}} - c_{\mathrm{im},i}) \pm \theta_{\mathrm{im},i} \mu_{\mathrm{im},i} c_{\mathrm{p,im},i} + \rho_{\mathrm{im}} \frac{\partial c_{\mathrm{im},i}^{\mathrm{sw}}}{\partial t} + A_{\mathrm{im}}^{\mathrm{aw}} \frac{\partial c_{\mathrm{im},i}^{\mathrm{aw}}}{\partial t} = 0. \tag{B.3}$$

The governing equations for PFAS concentrations at the solid–water and air–water interfaces of each $i^{\mathrm{th}}$ immobile matrix domain remain the same,

$$\begin{aligned} \frac{\partial c_{\mathrm{im},i}^{\mathrm{sw}}}{\partial t} &= \kappa_{\mathrm{im},i}^{\mathrm{sw}} \left[ \left(1 - F_{\mathrm{im,eq},i}^{\mathrm{sw}}\right) K_{\mathrm{im}}^{\mathrm{sw}} c_{\mathrm{im},i} - c_{\mathrm{im},i}^{\mathrm{sw}} \right], \\ \frac{\partial c_{\mathrm{im},i}^{\mathrm{aw}}}{\partial t} &= \kappa_{\mathrm{im},i}^{\mathrm{aw}} \left[ (1 - F_{\mathrm{im,eq},i}^{\mathrm{aw}}) K_{\mathrm{im}}^{\mathrm{aw}} c_{\mathrm{im},i} - c_{\mathrm{im},i}^{\mathrm{aw}} \right]. \end{aligned} \tag{B.4}$$

### B.2. Nondimensionalized governing equations

We derive the semi-analytical solutions for the dual-porosity model following the same procedure as the triple-porosity model.

$$-\frac{D_{\mathrm{f}}}{L v_{\mathrm{f}}} \frac{\partial^2 c_{\mathrm{f}}}{\partial Z^2} + \frac{\partial c_{\mathrm{f}}}{\partial Z} + \frac{\bar{v}}{v_{\mathrm{f}}} R_{\mathrm{f}} \frac{\partial c_{\mathrm{f}}}{\partial T} \pm \frac{\mu_{\mathrm{f}} L}{v_{\mathrm{f}}} c_{\mathrm{p,f}} + \sum_{i=1}^{N_{\mathrm{f}}^{\mathrm{sw}}} \frac{\bar{v}}{v_{\mathrm{f}}} \frac{\rho_{\mathrm{f}}}{\theta_{\mathrm{f}}} \frac{\partial c_{\mathrm{f},i}^{\mathrm{sw}}}{\partial T} + \sum_{i=1}^{N_{\mathrm{f}}^{\mathrm{aw}}} \frac{\bar{v}}{v_{\mathrm{f}}} \frac{A_{\mathrm{f}}^{\mathrm{aw}}}{\theta_{\mathrm{f}}} \frac{\partial c_{\mathrm{f},i}^{\mathrm{aw}}}{\partial T} + \frac{w_{\mathrm{im}}}{w_{\mathrm{f}}} \sum_{i=1}^{N_{\mathrm{im}}} \frac{w_{\mathrm{im},i} \kappa_{\mathrm{f,im},i} L}{\theta_{\mathrm{f}} v_{\mathrm{f}}} (c_{\mathrm{f}} - c_{\mathrm{im},i}) = 0, \tag{B.5}$$

where $\bar{v} = v_{\mathrm{f}} w_{\mathrm{f}} \theta_{\mathrm{f}} / (w_{\mathrm{f}} \theta_{\mathrm{f}} + w_{\mathrm{im}} \theta_{\mathrm{im}})$. The governing equations in the rate-limited solid-phase and air–water interfacial adsorption sites are

$$\begin{aligned} \frac{\partial c_{\mathrm{f},i}^{\mathrm{sw}}}{\partial T} &= \frac{L \kappa_{\mathrm{f},i}^{\mathrm{sw}}}{\bar{v}} \left[ f_{\mathrm{f},i}^{\mathrm{sw}} \left(1 - F_{\mathrm{f,eq}}^{\mathrm{sw}}\right) K_{\mathrm{f}}^{\mathrm{sw}} c_{\mathrm{f}} - c_{\mathrm{f},i}^{\mathrm{sw}} \right], \quad i = 1, 2, \ldots, N_{\mathrm{f}}^{\mathrm{sw}}, \\ \frac{\partial c_{\mathrm{f},i}^{\mathrm{aw}}}{\partial T} &= \frac{L \kappa_{\mathrm{f},i}^{\mathrm{aw}}}{\bar{v}} \left[ f_{\mathrm{f},i}^{\mathrm{aw}} (1 - F_{\mathrm{f,eq}}^{\mathrm{aw}}) K_{\mathrm{f}}^{\mathrm{aw}} c_{\mathrm{f}} - c_{\mathrm{f},i}^{\mathrm{aw}} \right], \quad i = 1, 2, \ldots, N_{\mathrm{f}}^{\mathrm{aw}}. \end{aligned} \tag{B.6}$$

The governing equation in the immobile matrix domain $i$ ($i = 1, 2, \ldots, N_{\mathrm{im}}$) is given by

$$R_{\mathrm{im},i} \frac{\partial c_{\mathrm{im},i}}{\partial T} - \frac{\kappa_{\mathrm{f,im},i} L}{\theta_{\mathrm{im},i} \bar{v}} (c_{\mathrm{f}} - c_{\mathrm{im},i}) \pm \frac{\mu_{\mathrm{im},i} L}{\bar{v}} c_{\mathrm{p,im},i} + \frac{\rho_{\mathrm{f}}}{\theta_{\mathrm{im},i}} \frac{\partial c_{\mathrm{im},i}^{\mathrm{sw}}}{\partial T} + \frac{A_{\mathrm{f}}^{\mathrm{aw}}}{\theta_{\mathrm{im},i}} \frac{\partial c_{\mathrm{im},i}^{\mathrm{aw}}}{\partial T} = 0. \tag{B.7}$$

The governing equations at the rate-limited solid-phase adsorption site, and rate-limited air–water interfacial adsorption site of the immobile matrix domain $i$ ($i = 1, 2, \ldots, N_{\mathrm{im}}$) are given by

$$\begin{aligned} \frac{\partial c_{\mathrm{im},i}^{\mathrm{sw}}}{\partial T} &= \frac{\kappa_{\mathrm{im},i}^{\mathrm{sw}} L}{\bar{v}} \left[ \left(1 - F_{\mathrm{im,eq},i}^{\mathrm{sw}}\right) K_{\mathrm{im}}^{\mathrm{sw}} c_{\mathrm{im},i} - c_{\mathrm{im},i}^{\mathrm{sw}} \right], \\ \frac{\partial c_{\mathrm{im},i}^{\mathrm{aw}}}{\partial T} &= \frac{\kappa_{\mathrm{im},i}^{\mathrm{aw}} L}{\bar{v}} \left[ (1 - F_{\mathrm{im,eq},i}^{\mathrm{aw}}) K_{\mathrm{im}}^{\mathrm{aw}} c_{\mathrm{im},i} - c_{\mathrm{im},i}^{\mathrm{aw}} \right]. \end{aligned} \tag{B.8}$$

Eqs. (B.5)–(B.8) can be solved given the following initial conditions,

$$\begin{aligned} &c_{\mathrm{f}}(Z, T=0) = c_{\mathrm{f}}^{0}(Z), \\ &c_{\mathrm{f},i}^{\mathrm{sw}}(Z, T=0) = c_{\mathrm{f},i}^{\mathrm{sw},0}(Z) \quad \left(i = 1, 2, \ldots, N_{\mathrm{f}}^{\mathrm{sw}}\right), \\ &c_{\mathrm{f},i}^{\mathrm{aw}}(Z, T=0) = c_{\mathrm{f},i}^{\mathrm{aw},0}(Z) \quad \left(i = 1, 2, \ldots, N_{\mathrm{f}}^{\mathrm{aw}}\right), \\ &c_{\mathrm{im},i}(Z, T=0) = c_{\mathrm{im},i}^{0}(Z) \quad \left(i = 1, 2, \ldots, N_{\mathrm{im}}\right), \\ &c_{\mathrm{im},i}^{\mathrm{sw}}(Z, T=0) = c_{\mathrm{im},i}^{\mathrm{sw},0}(Z) \quad \left(i = 1, 2, \ldots, N_{\mathrm{im}}\right), \\ &c_{\mathrm{im},i}^{\mathrm{aw}}(Z, T=0) = c_{\mathrm{im},i}^{\mathrm{aw},0}(Z) \quad \left(i = 1, 2, \ldots, N_{\mathrm{im}}\right), \end{aligned} \tag{B.9}$$

and boundary conditions

$$\left[ -\frac{D_{\mathrm{f}}}{L} \frac{\partial c_{\mathrm{f}}}{\partial Z} + v_{\mathrm{f}} c_{\mathrm{f}} \right]_{Z=0} = v_{\mathrm{f}} c_{\mathrm{f,in}}(T), \quad \& \quad \left[ \frac{\partial c_{\mathrm{f}}}{\partial Z} \right]_{Z=\infty} = 0. \tag{B.10}$$

### B.3. Simplification of the nondimensionalized governing equations

We derive the semi-analytical solutions for Eqs. (B.5)–(B.8) using the following nondimensionalized governing equations,

$$-\frac{1}{\mathcal{P}_{\mathrm{f}}} \frac{\partial^2 c_{\mathrm{f}}}{\partial Z^2} + \frac{\partial c_{\mathrm{f}}}{\partial Z} + \mathcal{R}_{\mathrm{f}} \frac{\partial c_{\mathrm{f}}}{\partial T} \pm \mathcal{U}_{\mathrm{f}} c_{\mathrm{p,f}} + \sum_{i=1}^{N_{\mathrm{f}}^{\mathrm{sw}}} \mathcal{R}_{\mathrm{f}}^{\mathrm{sw}} \frac{\partial c_{\mathrm{f},i}^{\mathrm{sw}}}{\partial T} + \sum_{i=1}^{N_{\mathrm{f}}^{\mathrm{aw}}} \mathcal{R}_{\mathrm{f}}^{\mathrm{aw}} \frac{\partial c_{\mathrm{f},i}^{\mathrm{aw}}}{\partial T} + \sum_{i=1}^{N_{\mathrm{im}}} \mathcal{K}_{\mathrm{f},i} (c_{\mathrm{f}} - c_{\mathrm{im},i}) = 0, \tag{B.11}$$

where $\mathcal{K}_{\mathrm{f},i} = (w_{\mathrm{im}} w_{\mathrm{im},i} \kappa_{\mathrm{f,im},i} L) / (w_{\mathrm{f}} \theta_{\mathrm{f}} v_{\mathrm{f}})$,

$$\begin{aligned} \frac{\partial c_{\mathrm{f},i}^{\mathrm{sw}}}{\partial T} &= \mathcal{A}_{\mathrm{f},i}^{\mathrm{sw}} c_{\mathrm{f}} - \mathcal{B}_{\mathrm{f},i}^{\mathrm{sw}} c_{\mathrm{f},i}^{\mathrm{sw}}, \quad i = 1, 2, \ldots, N_{\mathrm{f}}^{\mathrm{sw}}, \\ \frac{\partial c_{\mathrm{f},i}^{\mathrm{aw}}}{\partial T} &= \mathcal{A}_{\mathrm{f},i}^{\mathrm{aw}} c_{\mathrm{f}} - \mathcal{B}_{\mathrm{f},i}^{\mathrm{aw}} c_{\mathrm{f},i}^{\mathrm{aw}}, \quad i = 1, 2, \ldots, N_{\mathrm{f}}^{\mathrm{aw}}, \end{aligned} \tag{B.12}$$

$$\mathcal{R}_{\mathrm{im},i} \frac{\partial c_{\mathrm{im},i}}{\partial T} - \mathcal{K}_{\mathrm{im},i} (c_{\mathrm{f}} - c_{\mathrm{im},i}) \pm \mathcal{U}_{\mathrm{im},i} c_{\mathrm{p,im},i} + \mathcal{R}_{\mathrm{im},i}^{\mathrm{sw}} \frac{\partial c_{\mathrm{im},i}^{\mathrm{sw}}}{\partial T} + \mathcal{R}_{\mathrm{im},i}^{\mathrm{aw}} \frac{\partial c_{\mathrm{im},i}^{\mathrm{aw}}}{\partial T} = 0, \quad i = 1, 2, \ldots, N_{\mathrm{im}}, \tag{B.13}$$

$$\begin{aligned} \frac{\partial c_{\mathrm{im},i}^{\mathrm{sw}}}{\partial T} &= \mathcal{A}_{\mathrm{im},i}^{\mathrm{sw}} c_{\mathrm{im},i} - \mathcal{B}_{\mathrm{im},i}^{\mathrm{sw}} c_{\mathrm{im},i}^{\mathrm{sw}}, \quad i = 1, 2, \ldots, N_{\mathrm{im}}, \\ \frac{\partial c_{\mathrm{im},i}^{\mathrm{aw}}}{\partial T} &= \mathcal{A}_{\mathrm{im},i}^{\mathrm{aw}} c_{\mathrm{im},i} - \mathcal{B}_{\mathrm{im},i}^{\mathrm{aw}} c_{\mathrm{im},i}^{\mathrm{aw}}, \quad i = 1, 2, \ldots, N_{\mathrm{im}}. \end{aligned} \tag{B.14}$$

### B.4. Laplace transform

We take the Laplace transform in time for Eqs. (B.11)–(B.14), which yields

$$-\frac{1}{\mathcal{P}_\mathrm{f}}\frac{\partial^2\tilde{c}_\mathrm{f}}{\partial Z^2}+\frac{\partial\tilde{c}_\mathrm{f}}{\partial Z}+\mathcal{R}_\mathrm{f}(s\tilde{c}_\mathrm{f}-\tilde{c}^0{}_\mathrm{f})\pm\mathcal{U}_\mathrm{f}\tilde{c}_\mathrm{p,f}+\sum_{i=1}^{N_\mathrm{f}^\mathrm{sw}}\mathcal{R}_\mathrm{f}^\mathrm{sw}(s\tilde{c}_{\mathrm{f},i}^\mathrm{sw}-c_{\mathrm{f},i}^{\mathrm{sw},0})+\sum_{i=1}^{N_\mathrm{f}^\mathrm{aw}}\mathcal{R}_\mathrm{f}^\mathrm{aw}(s\tilde{c}_{\mathrm{f},i}^\mathrm{aw}-c_{\mathrm{f},i}^{\mathrm{aw},0})+\sum_{i=1}^{N_\mathrm{im}}\mathcal{K}_{\mathrm{f},i}(\tilde{c}_\mathrm{f}-\tilde{c}_{\mathrm{im},i})=0, \tag{B.15}$$

$$\begin{aligned}s\tilde{c}_{\mathrm{f},i}^\mathrm{sw}-c_{\mathrm{f},i}^{\mathrm{sw},0}&=\mathcal{A}_{\mathrm{f},i}^\mathrm{sw}\tilde{c}_\mathrm{f}-\mathcal{B}_{\mathrm{f},i}^\mathrm{sw}\tilde{c}_{\mathrm{f},i}^\mathrm{sw},\quad i=1,2,\dots,N_\mathrm{f}^\mathrm{sw},\\ s\tilde{c}_{\mathrm{f},i}^\mathrm{aw}-c_{\mathrm{f},i}^{\mathrm{aw},0}&=\mathcal{A}_{\mathrm{f},i}^\mathrm{aw}\tilde{c}_\mathrm{f}-\mathcal{B}_{\mathrm{f},i}^\mathrm{aw}\tilde{c}_{\mathrm{f},i}^\mathrm{aw},\quad i=1,2,\dots,N_\mathrm{f}^\mathrm{aw},\end{aligned} \tag{B.16}$$

$$\mathcal{R}_{\mathrm{im},i}\left(s\tilde{c}_{\mathrm{im},i}-c_{\mathrm{im},i}^0\right)+\mathcal{R}_{\mathrm{im},i}^\mathrm{aw}\left(s\tilde{c}_{\mathrm{im},i}^\mathrm{aw}-c_{\mathrm{im},i}^{\mathrm{aw},0}\right)\pm\mathcal{U}_{\mathrm{im},i}\tilde{c}_{\mathrm{p,im},i}-\mathcal{K}_{\mathrm{im},i}(\tilde{c}_\mathrm{f}-\tilde{c}_{\mathrm{im},i})+\mathcal{R}_{\mathrm{im},i}^\mathrm{sw}\left(s\tilde{c}_{\mathrm{im},i}^\mathrm{sw}-c_{\mathrm{im},i}^{\mathrm{sw},0}\right)=0,\quad i=1,2,\dots,N_\mathrm{im}, \tag{B.17}$$

$$\begin{aligned}s\tilde{c}_{\mathrm{im},i}^\mathrm{sw}-c_{\mathrm{im},i}^{\mathrm{sw},0}&=\mathcal{A}_{\mathrm{im},i}^\mathrm{sw}\tilde{c}_{\mathrm{im},i}-\mathcal{B}_{\mathrm{im},i}^\mathrm{sw}\tilde{c}_{\mathrm{im},i}^\mathrm{sw},\quad i=1,2,\dots,N_\mathrm{im},\\ s\tilde{c}_{\mathrm{im},i}^\mathrm{aw}-c_{\mathrm{im},i}^{\mathrm{aw},0}&=\mathcal{A}_{\mathrm{im},i}^\mathrm{aw}\tilde{c}_{\mathrm{im},i}-\mathcal{B}_{\mathrm{im},i}^\mathrm{aw}\tilde{c}_{\mathrm{im},i}^\mathrm{aw},\quad i=1,2,\dots,N_\mathrm{im}.\end{aligned} \tag{B.18}$$

Eqs. (B.15)–(B.18) contains the following unknown variables: $\tilde{c}_\mathrm{f}$, $\tilde{c}_{\mathrm{f},i}^\mathrm{sw}$, $\tilde{c}_{\mathrm{f},i}^\mathrm{aw}$, $\tilde{c}_{\mathrm{im},i}$, $\tilde{c}_{\mathrm{im},i}^\mathrm{sw}$ and $\tilde{c}_{\mathrm{im},i}^\mathrm{aw}$. Similar to the derivations in Appendix A.3, we rearrange the equations to eliminate the unknown variables except for $\tilde{c}_\mathrm{f}$ and obtain the following equation,

$$-\frac{1}{\mathcal{P}_\mathrm{f}}\frac{\partial^2\tilde{c}_\mathrm{f}}{\partial Z^2}+\frac{\partial\tilde{c}_\mathrm{f}}{\partial Z}+h_\mathrm{f}(s)\tilde{c}_\mathrm{f}+h_\mathrm{f}^0(Z,s)=0, \tag{B.19}$$

where $h_\mathrm{f}(s)$ and $h_\mathrm{f}^0(Z,s)$ have different expressions for PFAAs and precursors. For PFAAs, $h_\mathrm{f}(s)$ and $h_\mathrm{f}^0(Z,s)$ are given by

$$\begin{aligned}h_\mathrm{f}(s)=&s\mathcal{R}_\mathrm{f}+\sum_{i=1}^{N_\mathrm{f}^\mathrm{sw}}\frac{s\mathcal{R}_\mathrm{f}^\mathrm{sw}\mathcal{A}_{\mathrm{f},i}^\mathrm{sw}}{s+\mathcal{B}_{\mathrm{f},i}^\mathrm{sw}}+\sum_{i=1}^{N_\mathrm{f}^\mathrm{aw}}\frac{s\mathcal{R}_\mathrm{f}^\mathrm{aw}\mathcal{A}_{\mathrm{f},i}^\mathrm{aw}}{s+\mathcal{B}_{\mathrm{f},i}^\mathrm{aw}}+\sum_{i=1}^{N_\mathrm{im}}\mathcal{K}_{\mathrm{f},i}\frac{g_{\mathrm{im},i}(s)-\mathcal{K}_{\mathrm{im},i}}{g_{\mathrm{im},i}(s)},\\ h_\mathrm{f}^0(Z,s)=&-\mathcal{R}_\mathrm{f}\tilde{c}_\mathrm{f}^0-\mathcal{U}_\mathrm{f}\tilde{c}_\mathrm{p,f}-\sum_{i=1}^{N_\mathrm{im}}\mathcal{K}_{\mathrm{f},i}\frac{g_{\mathrm{im},i}^0(Z,s)}{g_{\mathrm{im},i}(s)}\\ &-\sum_{i=1}^{N_\mathrm{f}^\mathrm{sw}}\frac{\mathcal{R}_\mathrm{f}^\mathrm{sw}\mathcal{B}_{\mathrm{f},i}^\mathrm{sw}c_{\mathrm{f},i}^{\mathrm{sw},0}}{s+\mathcal{B}_{\mathrm{f},i}^\mathrm{sw}}-\sum_{i=1}^{N_\mathrm{f}^\mathrm{aw}}\frac{\mathcal{R}_\mathrm{f}^\mathrm{aw}\mathcal{B}_{\mathrm{f},i}^\mathrm{aw}c_{\mathrm{f},i}^{\mathrm{aw},0}}{s+\mathcal{B}_{\mathrm{f},i}^\mathrm{aw}},\end{aligned} \tag{B.20}$$

where

$$\begin{aligned}g_{\mathrm{im},i}(s)=&s\mathcal{R}_{\mathrm{im},i}+\mathcal{K}_{\mathrm{im},i}+\frac{s\mathcal{R}_{\mathrm{im},i}^\mathrm{sw}\mathcal{A}_{\mathrm{im},i}^\mathrm{sw}}{s+\mathcal{B}_{\mathrm{im},i}^\mathrm{sw}}+\frac{s\mathcal{R}_{\mathrm{im},i}^\mathrm{aw}\mathcal{A}_{\mathrm{im},i}^\mathrm{aw}}{s+\mathcal{B}_{\mathrm{im},i}^\mathrm{aw}},\\ g_{\mathrm{im},i}^0(Z,s)=&\mathcal{R}_{\mathrm{im},i}c_{\mathrm{im},i}^0+\mathcal{U}_{\mathrm{im},i}\tilde{c}_{\mathrm{p,im},i}+\frac{\mathcal{R}_{\mathrm{im},i}^\mathrm{sw}\mathcal{B}_{\mathrm{im},i}^\mathrm{sw}c_{\mathrm{im},i}^{\mathrm{sw},0}}{s+\mathcal{B}_{\mathrm{im},i}^\mathrm{sw}}+\frac{\mathcal{R}_{\mathrm{im},i}^\mathrm{aw}\mathcal{B}_{\mathrm{im},i}^\mathrm{aw}c_{\mathrm{im},i}^{\mathrm{aw},0}}{s+\mathcal{B}_{\mathrm{im},i}^\mathrm{aw}},\end{aligned} \tag{B.21}$$

where $\tilde{c}_\mathrm{p,f}$ and $\tilde{c}_{\mathrm{p,im},i}$ are the Laplace-transformed aqueous concentrations of precursors in the fracture and matrix domains, respectively. Eqs. (B.20)–(B.21) apply to PFAAs either without or with mass sources from precursor transformation. If the equation is applied to PFAAs without transformation-induced mass sources, the relevant source terms are set to zero: $\mathcal{U}_\mathrm{f}=\mathcal{U}_{\mathrm{im},i}=0$. If Eqs. (B.20)–(B.21) are used for PFAAs with transformation-induced mass sources, the precursor-related variables ($\tilde{c}_\mathrm{p,f}$ and $\tilde{c}_{\mathrm{p,im},i}$) need to be first solved via Equation (B.19) using precursor-associated parameters and functions (i.e., $h_\mathrm{f}(s)$ and $h_\mathrm{f}^0(Z,s)$).

The precursor-associated functions (i.e., $h_\mathrm{f}(s)$ and $h_\mathrm{f}^0(Z,s)$) are derived by setting $\tilde{c}_\mathrm{p,f}=\tilde{c}_\mathrm{f}$ and $\tilde{c}_{\mathrm{p,im},i}=\tilde{c}_{\mathrm{im},i}$, which yields

$$\begin{aligned}h_\mathrm{f}(s)=&s\mathcal{R}_\mathrm{f}+\mathcal{U}_\mathrm{f}+\sum_{i=1}^{N_\mathrm{f}^\mathrm{sw}}\frac{s\mathcal{R}_\mathrm{f}^\mathrm{sw}\mathcal{A}_{\mathrm{f},i}^\mathrm{sw}}{s+\mathcal{B}_{\mathrm{f},i}^\mathrm{sw}}+\sum_{i=1}^{N_\mathrm{f}^\mathrm{aw}}\frac{s\mathcal{R}_\mathrm{f}^\mathrm{aw}\mathcal{A}_{\mathrm{f},i}^\mathrm{aw}}{s+\mathcal{B}_{\mathrm{f},i}^\mathrm{aw}}+\sum_{i=1}^{N_\mathrm{im}}\mathcal{K}_{\mathrm{f},i}\frac{g_{\mathrm{im},i}(s)-\mathcal{K}_{\mathrm{im},i}}{g_{\mathrm{im},i}(s)},\\ h_\mathrm{f}^0(Z,s)=&-\mathcal{R}_\mathrm{f}\tilde{c}_\mathrm{f}^0-\sum_{i=1}^{N_\mathrm{im}}\mathcal{K}_{\mathrm{f},i}\frac{g_{\mathrm{im},i}^0(Z,s)}{g_{\mathrm{im},i}(s)}\\ &-\sum_{i=1}^{N_\mathrm{f}^\mathrm{sw}}\frac{\mathcal{R}_\mathrm{f}^\mathrm{sw}\mathcal{B}_{\mathrm{f},i}^\mathrm{sw}c_{\mathrm{f},i}^{\mathrm{sw},0}}{s+\mathcal{B}_{\mathrm{f},i}^\mathrm{sw}}-\sum_{i=1}^{N_\mathrm{f}^\mathrm{aw}}\frac{\mathcal{R}_\mathrm{f}^\mathrm{aw}\mathcal{B}_{\mathrm{f},i}^\mathrm{aw}c_{\mathrm{f},i}^{\mathrm{aw},0}}{s+\mathcal{B}_{\mathrm{f},i}^\mathrm{aw}},\end{aligned} \tag{B.22}$$

where

$$\begin{aligned}g_{\mathrm{im},i}(s)=&s\mathcal{R}_{\mathrm{im},i}+\mathcal{K}_{\mathrm{im},i}+\mathcal{U}_{\mathrm{im},i}+\frac{s\mathcal{R}_{\mathrm{im},i}^\mathrm{sw}\mathcal{A}_{\mathrm{im},i}^\mathrm{sw}}{s+\mathcal{B}_{\mathrm{im},i}^\mathrm{sw}}+\frac{s\mathcal{R}_{\mathrm{im},i}^\mathrm{aw}\mathcal{A}_{\mathrm{im},i}^\mathrm{aw}}{s+\mathcal{B}_{\mathrm{im},i}^\mathrm{aw}},\\ g_{\mathrm{im},i}^0(Z,s)=&\mathcal{R}_{\mathrm{im},i}c_{\mathrm{im},i}^0+\frac{\mathcal{R}_{\mathrm{im},i}^\mathrm{sw}\mathcal{B}_{\mathrm{im},i}^\mathrm{sw}c_{\mathrm{im},i}^{\mathrm{sw},0}}{s+\mathcal{B}_{\mathrm{im},i}^\mathrm{sw}}+\frac{\mathcal{R}_{\mathrm{im},i}^\mathrm{aw}\mathcal{B}_{\mathrm{im},i}^\mathrm{aw}c_{\mathrm{im},i}^{\mathrm{aw},0}}{s+\mathcal{B}_{\mathrm{im},i}^\mathrm{aw}}.\end{aligned} \tag{B.23}$$

Eq. (B.19) and Eqs. (B.20)–(B.21) are used for PFAAs, while Equation (B.19) and Eqs. (B.22)–(B.23) are used for precursors. They can be solved following the same procedure hereafter. The next step is to take the Laplace transform in space for Eq. (B.19), which yields

$$-\frac{1}{\mathcal{P}_\mathrm{f}}\left(r^2\hat{\tilde{c}}_\mathrm{f}-r\tilde{c}_\mathrm{f}|_{Z=0}-\frac{\partial\tilde{c}_\mathrm{f}}{\partial Z}|_{Z=0}\right)+r\hat{\tilde{c}}_\mathrm{f}-\tilde{c}_\mathrm{f}|_{Z=0}+h_\mathrm{f}(s)\hat{\tilde{c}}_\mathrm{f}+\hat{h}_\mathrm{f}^0(r,s)=0. \tag{B.24}$$

Eq. (B.24) is subject to the boundary condition given by Eq. (B.10). We can take the Laplace transform of Eq. (B.10) at $Z=0$ and cast it into Eq. (B.24), which yields

$$\begin{aligned}\hat{\tilde{c}}_\mathrm{f}=&\frac{\tilde{c}_\mathrm{f}|_{Z=0}}{r_1-r_2}\left(\frac{r_1}{r-r_1}-\frac{r_2}{r-r_2}\right)\\ &-\frac{\mathcal{P}_\mathrm{f}\tilde{c}_\mathrm{f,in}}{r_1-r_2}\left(\frac{1}{r-r_1}-\frac{1}{r-r_2}\right)\\ &+\frac{\mathcal{P}_\mathrm{f}}{r_1-r_2}\left(\frac{\hat{h}_\mathrm{f}^0(r,s)}{r-r_1}-\frac{\hat{h}_\mathrm{f}^0(r,s)}{r-r_2}\right),\end{aligned} \tag{B.25}$$

where $r_1=\mathcal{P}_\mathrm{f}/2\left(1-\sqrt{4h_\mathrm{f}(s)/\mathcal{P}_\mathrm{f}+1}\right)$ and $r_2=\mathcal{P}_\mathrm{f}/2\left(1+\sqrt{4h_\mathrm{f}(s)/\mathcal{P}_\mathrm{f}+1}\right)$.

### B.5. Inverse Laplace transform

We obtain the semi-analytical solutions from the inverse Laplace transform of Eq. (B.25), which gives

$$\begin{aligned}\tilde{c}_\mathrm{f}=&\frac{\tilde{c}_\mathrm{f}|_{Z=0}}{r_1-r_2}\left(r_1\exp(r_1Z)-r_2\exp(r_2Z)\right)\\ &-\frac{\mathcal{P}_\mathrm{f}\tilde{c}_\mathrm{f,in}}{r_1-r_2}\left(\exp(r_1Z)-\exp(r_2Z)\right)\\ &+\frac{\mathcal{P}_\mathrm{f}}{r_1-r_2}\int_0^Z\exp(r_1(Z-z'))h_\mathrm{f}^0(z',s)dz'\\ &-\frac{\mathcal{P}_\mathrm{f}}{r_1-r_2}\int_0^Z\exp(r_2(Z-z'))h_\mathrm{f}^0(z',s)dz'.\end{aligned} \tag{B.26}$$

Therefore,

$$\begin{aligned}\frac{\partial\tilde{c}_\mathrm{f}}{\partial Z}=&\frac{\tilde{c}_\mathrm{f}|_{Z=0}}{r_1-r_2}\left(r_1^2\exp(r_1Z)-r_2^2\exp(r_2Z)\right)\\ &-\frac{\mathcal{P}_\mathrm{f}\tilde{c}_\mathrm{f,in}}{r_1-r_2}\left(r_1\exp(r_1Z)-r_2\exp(r_2Z)\right)\\ &+\frac{\mathcal{P}_\mathrm{f}}{r_1-r_2}\left(r_1\int_0^Z\exp(r_1(Z-z'))h_\mathrm{f}^0(z',s)dz'+h_\mathrm{f}^0(Z,s)\right)\\ &-\frac{\mathcal{P}_\mathrm{f}}{r_1-r_2}\left(r_2\int_0^Z\exp(r_2(Z-z'))h_\mathrm{f}^0(z',s)dz'+h_\mathrm{f}^0(Z,s)\right).\end{aligned} \tag{B.27}$$

Given the boundary condition at $z = \infty$ (Eq. (B.10)), we get

$$\begin{aligned}\lim_{Z=\infty}\frac{\partial\tilde{c}_{\mathrm{f}}}{\partial Z} &= \lim_{Z=\infty}\exp(r_2 Z)\left[\frac{\tilde{c}_{\mathrm{f}}|_{Z=0}}{r_1-r_2}\left(r_1^2\exp((r_1-r_2)Z)-r_2^2\right)\right.\\ &-\frac{\mathcal{P}_{\mathrm{f}}\tilde{c}_{\mathrm{f,in}}}{r_1-r_2}\left(r_1\exp((r_1-r_2)Z)-r_2\right)\\ &+\frac{\mathcal{P}_{\mathrm{f}}}{r_1-r_2}\left(r_1\int_0^Z\exp(r_1(Z-z'))h_{\mathrm{f}}^0(z',s)dz'\right)\exp(-r_2Z)\\ &\left.-\frac{\mathcal{P}_{\mathrm{f}}}{r_1-r_2}\left(r_2\int_0^Z\exp(-r_2z')h_{\mathrm{f}}^0(z',s)dz'\right)\right]\\ &=0.\end{aligned} \tag{B.28}$$

Given $\lim_{Z=\infty}\exp((r_1-r_2)Z)=0$, we compute $\tilde{c}_{\mathrm{f}}|_{Z=0}$ from Eq. (B.28), which yields

$$\begin{aligned}\tilde{c}_{\mathrm{f}}|_{Z=0} =& \frac{\mathcal{P}_{\mathrm{f}}}{r_2}\left[\tilde{c}_{\mathrm{f,in}}-\int_0^\infty\exp(-r_2z')h_{\mathrm{f}}^0(z',s)dz'\right.\\ &\left.+\left(\frac{r_1}{r_2}\int_0^Z\exp(r_1(Z-z'))h_{\mathrm{f}}^0(z',s)dz'\right)\exp(-r_2Z)\right].\end{aligned} \tag{B.29}$$

Casting Eq. (B.29) into Eq. (B.26) yields the solution in the Laplace domain,

$$\begin{aligned}\tilde{c}_{\mathrm{f}} =& \left[\tilde{c}_{\mathrm{f,in}}-\int_0^\infty\exp(-r_2z')h_{\mathrm{f}}^0(z',s)dz'\right.\\ &\left.+\left(\frac{r_1}{r_2}\int_0^Z\exp(r_1(Z-z'))h_{\mathrm{f}}^0(z',s)dz'\right)\exp(-r_2Z)\right]\\ &\times\frac{\mathcal{P}_{\mathrm{f}}}{r_2(r_1-r_2)}\left(r_1\exp(r_1Z)-r_2\exp(r_2Z)\right)\\ &-\frac{\mathcal{P}_{\mathrm{f}}\tilde{c}_{\mathrm{f,in}}}{r_1-r_2}\left(\exp(r_1Z)-\exp(r_2Z)\right)\\ &+\frac{\mathcal{P}_{\mathrm{f}}}{r_1-r_2}\int_0^Z\exp(r_1(Z-z'))h_{\mathrm{f}}^0(z',s)dz'\\ &-\frac{\mathcal{P}_{\mathrm{f}}}{r_1-r_2}\int_0^Z\exp(r_2(Z-z'))h_{\mathrm{f}}^0(z',s)dz'.\end{aligned} \tag{B.30}$$

We can then perform the inverse Laplace transform on $\tilde{c}_{\mathrm{f}}$ to compute the spatial and temporal variations of aqueous concentrations in the mobile region. This can be done analytically using the method provided by Toride et al. (1993) or numerically using the methods reported by Durbin (1974), Crump (1976), and De Hoog et al. (1982).

## Appendix C. Criteria for identifying nonequilibrium transport regimes and guiding model selections

We use the semi-analytical solutions to derive the criteria to identify the nonequilibrium transport regimes and provide guidance for selecting the appropriate model complexity for a given problem. This is done by performing the temporal moment analysis on the mass discharge concentration curves (Aris, 1958; Valocchi, 1985; Leij et al., 2012) and computing the relative difference in the temporal moments. The derivations are summarized below.

In general, we can compute the $n^{\mathrm{th}}$ normalized absolute temporal moments via the following equations (e.g., Valocchi, 1985)

$$m_n=\int_0^\infty T^n c(Z,T)\,\mathrm{d}T=(-1)^n\lim_{s\to0}\frac{\partial^n\tilde{c}(Z,s)}{\partial s^n}, \tag{C.1}$$

where $\tilde{c}$ is the aqueous concentration at location $Z$ and Laplace time $s$.

For the mathematical convenience of deriving $\tilde{c}$, we assume that the adsorption is instantaneous (which can be relaxed if rate-limited adsorption is of interest) and that the inlet boundary condition is given by a Dirac delta function with a unit mass. Accordingly, we can compute $\tilde{c}$ for all the models.

For the single-porosity and dual-porosity models, $\tilde{c}$ is given by (e.g., Valocchi, 1985)

$$\tilde{c}(Z,s)=\exp\left\{\frac{P}{2}\left[1-\left(1+\frac{4}{P}h(s)\right)^{1/2}\right]\right\}, \tag{C.2}$$

where $P$ is the Péclet number and $h(s)$ is a function in the Laplace time domain which can be obtained from the Laplace transform of the governing equations of a specific model. The $h(s)$ are derived from the governing equations and their Laplace transform, as provided below.

For a single-porosity model, the governing equation is given by

$$-\frac{1}{P}\frac{\partial^2c}{\partial Z^2}+\frac{\partial c}{\partial Z}+R\frac{\partial c}{\partial T}+\mathcal{U}c=0, \tag{C.3}$$

where $P=vL/D$ is the Péclet number, $R=1+K^{\mathrm{aw}}A^{\mathrm{aw}}/\theta+\rho A^{\mathrm{sw}}/\theta$ is the retardation factor, $\mathcal{U}=\mu L/v$ is the Damköhler number for transformation, and $T$ is the dimensionless time ($T=t/(L/v)$ with $v$ being the porewater velocity). Taking the Laplace transform of the above equation yields

$$-\frac{1}{P}\frac{\partial^2\tilde{c}}{\partial Z^2}+\frac{\partial\tilde{c}}{\partial Z}+h(s)\tilde{c}=0, \tag{C.4}$$

where $h(s)=Rs+\mathcal{U}$. Substituting $h(s)$ into Eqs. (C.1) and (C.2) allows for computing the temporal moments for the breakthrough curves of a single-porosity model.

For a dual-porosity model, we further assume the matrix contains only one immobile domain and obtain the governing equations as

$$\begin{aligned}-\frac{1}{P_{\mathrm{f}}}\frac{\partial^2c_{\mathrm{f}}}{\partial Z^2}+\frac{\partial c_{\mathrm{f}}}{\partial Z}+\frac{\bar{v}}{v_{\mathrm{f}}}R_{\mathrm{f}}\frac{\partial c_{\mathrm{f}}}{\partial T}+\mathcal{U}_{\mathrm{f}}c_{\mathrm{f}}+\frac{w_{\mathrm{im}}}{w_{\mathrm{f}}\theta_{\mathrm{f}}}\mathrm{Da}_{\mathrm{f,im}}(c_{\mathrm{f}}-c_{\mathrm{im}})=0,\\ R_{\mathrm{im}}\frac{\partial c_{\mathrm{im}}}{\partial T}+\frac{v_{\mathrm{f}}}{\bar{v}}\mathcal{U}_{\mathrm{im}}c_{\mathrm{im}}-\frac{v_{\mathrm{f}}}{\theta_{\mathrm{im}}\bar{v}}\mathrm{Da}_{\mathrm{f,im}}(c_{\mathrm{f}}-c_{\mathrm{im}})=0,\end{aligned} \tag{C.5}$$

where $\bar{v}=w_{\mathrm{f}}\theta_{\mathrm{f}}v_{\mathrm{f}}/(w_{\mathrm{f}}\theta_{\mathrm{f}}+w_{\mathrm{im}}\theta_{\mathrm{im}})$, $T$ is the dimensionless time (i.e., $T=t/(L/\bar{v})$), and $P_{\mathrm{f}}=v_{\mathrm{f}}L/D_{\mathrm{f}}$, $\mathrm{Da}_{\mathrm{f,im}}=\kappa_{\mathrm{f,im}}L/v_{\mathrm{f}}$, and $\mathcal{U}_{\mathrm{f}}=\mu_{\mathrm{f}}L/v_{\mathrm{f}}$ are respectively the Péclet number, Damköhler number for fracture–matrix mass transfer, and Damköhler number for transformation in the fracture domain; and $\mathcal{U}_{\mathrm{im}}=\mu_{\mathrm{im}}L/v_{\mathrm{f}}$ is Damköhler number for transformation in the immobile matrix domain. Applying the Laplace transform to Eq. (C.5) and rearranging the resulting equation yields

$$-\frac{1}{P_{\mathrm{f}}}\frac{\partial^2\tilde{c}_{\mathrm{f}}}{\partial Z^2}+\frac{\partial\tilde{c}_{\mathrm{f}}}{\partial Z}+h(s)\tilde{c}_{\mathrm{f}}=0, \tag{C.6}$$

where $h(s)=\bar{v}R_{\mathrm{f}}s/v_{\mathrm{f}}+\mathcal{U}_{\mathrm{f}}+\frac{w_{\mathrm{im}}\theta_{\mathrm{im}}}{w_{\mathrm{f}}\theta_{\mathrm{f}}}\frac{\mathrm{Da}_{\mathrm{f,im}}(R_{\mathrm{im}}s+\mathcal{U}_{\mathrm{im}})}{\theta_{\mathrm{im}}\bar{v}R_{\mathrm{im}}s/v_{\mathrm{f}}+\theta_{\mathrm{im}}\mathcal{U}_{\mathrm{im}}+\mathrm{Da}_{\mathrm{f,im}}}$. Substituting $h(s)$ into Eqs. (C.1) and (C.2) allows for computing the temporal moments for the breakthrough curves of a dual-porosity model.

For the dual-permeability model, the $\tilde{c}$ in Eq. (C.1) is given by $\tilde{c}=(w_{\mathrm{f}}\theta_{\mathrm{f}}v_{\mathrm{f}}\tilde{c}_{\mathrm{f}}+w_{\mathrm{m}}\theta_{\mathrm{m}}v_{\mathrm{m}}\tilde{c}_{\mathrm{m}})/(w_{\mathrm{f}}\theta_{\mathrm{f}}v_{\mathrm{f}}+w_{\mathrm{m}}\theta_{\mathrm{m}}v_{\mathrm{m}})$, where $\tilde{c}_{\mathrm{f}}$ and $\tilde{c}_{\mathrm{m}}$ are solved using the following governing equations,

$$\begin{aligned}-\frac{1}{P_{\mathrm{f}}}\frac{\partial^2c_{\mathrm{f}}}{\partial Z^2}+\frac{\partial c_{\mathrm{f}}}{\partial Z}+\frac{\bar{v}}{v_{\mathrm{f}}}R_{\mathrm{f}}\frac{\partial c_{\mathrm{f}}}{\partial T}+\mathcal{U}_{\mathrm{f}}c_{\mathrm{f}}+\frac{w_{\mathrm{m}}}{w_{\mathrm{f}}\theta_{\mathrm{f}}}\mathrm{Da}_{\mathrm{f,m}}(c_{\mathrm{f}}-c_{\mathrm{m}})=0,\\ -\frac{1}{P_{\mathrm{m}}}\frac{\partial^2c_{\mathrm{m}}}{\partial Z^2}+\frac{\partial c_{\mathrm{m}}}{\partial Z}+\frac{\bar{v}}{v_{\mathrm{m}}}R_{\mathrm{m}}\frac{\partial c_{\mathrm{m}}}{\partial T}+\frac{v_{\mathrm{f}}}{v_{\mathrm{m}}}\mathcal{U}_{\mathrm{m}}c_{\mathrm{m}}-\frac{v_{\mathrm{f}}}{v_{\mathrm{m}}\theta_{\mathrm{m}}}\mathrm{Da}_{\mathrm{f,m}}(c_{\mathrm{f}}-c_{\mathrm{m}})=0,\end{aligned} \tag{C.7}$$

where $\bar{v}=(w_{\mathrm{f}}\theta_{\mathrm{f}}v_{\mathrm{f}}+w_{\mathrm{m}}\theta_{\mathrm{m}}v_{\mathrm{m}})/(w_{\mathrm{f}}\theta_{\mathrm{f}}+w_{\mathrm{m}}\theta_{\mathrm{m}})$, $T$ is the dimensionless time (i.e., $T=t/(L/\bar{v})$), $\mathrm{Da}_{\mathrm{f,m}}=\kappa_{\mathrm{f,m}}L/v_{\mathrm{f}}$ and $\mathcal{U}_{\mathrm{f}}=\mu_{\mathrm{f}}L/v_{\mathrm{f}}$ are respectively the Damköhler number for fracture–matrix mass transfer and Damköhler number for transformation in the fracture domain, and $\mathcal{U}_{\mathrm{m}}=\mu_{\mathrm{m}}L/v_{\mathrm{f}}$ is Damköhler number for transformation in the mobile matrix domain. For mathematical convenience, we assume $P_{\mathrm{m}}=P_{\mathrm{f}}$ and solve $\tilde{c}_{\mathrm{f}}$ and $\tilde{c}_{\mathrm{m}}$ using the method presented by Leij et al. (2012). Then we compute the flux-averaged breakthrough curve in the Laplace domain and evaluate the temporal moments from Eq. (C.1). This method also applies to the triple-porosity model. However, fully analytical solutions in the Laplace domain may be challenging to obtain for dual-permeability and triple-porosity models under more general conditions (e.g., $P_{\mathrm{m}}\neq P_{\mathrm{f}}$). In those cases, we can compute the flux-averaged aqueous PFAS concentration at the outlet using Eq. (A.22), and then evaluate the temporal moments from Eq. (C.1) via symbolic calculations or numerical approximations.

We apply the above methods to compute the first and second moments for all three models (see Table C.5). The relative differences

in moments are used to identify the nonequilibrium transport regimes and guide model selections. For a specific problem, if the relative differences are small between two models with different complexities, the simpler model is then sufficient for the simulations. Otherwise, the more sophisticated model may need to be adopted. For example, if the fracture flow is much faster than the matrix flow (i.e., $\eta = v_m/v_f \to 0$) in a heterogeneous vadose zone, a dual-permeability model will share the same moments as those of a dual-porosity model. In that case, a dual-porosity model can be used. Furthermore, if the residence time in the fracture domain is much longer than the time scale of fracture–matrix mass transfer (i.e., $\mathrm{Da}_{f,m} \to \infty$), the dual-porosity model shares the same moments as those of an effective single-porosity model. The parameters for the effective single-porosity model can be obtained by comparing the moments for the two models, as provided in Table C.5. The comparison shows that the parameters for the effective single-porosity model (i.e., Eq. (C.3)) are given by: $R = \frac{w_f\theta_f R_f + w_{im}\theta_{im} R_{im}}{w_f\theta_f + w_{im}\theta_{im}}$, $P = P_f = v_f L/D_f$, and $\mathcal{U} = \frac{w_f\theta_f \mathcal{U}_f + w_{im}\theta_{im}\mathcal{U}_{im}}{w_f\theta_f} = \frac{L}{v_f}\frac{w_f\theta_f\mu_f + w_{im}\theta_{im}\mu_{im}}{w_f\theta_f}$, where the parameters with subscripts "f" and "im" are respectively defined in the fracture and immobile matrix domains of the dual-porosity model. Additionally, the dimensionless time in the effective model (i.e., Eq. (C.3)) is given by $T = t/(L/\bar{v})$ where $\bar{v} = w_f\theta_f v_f/(w_f\theta_f + w_{im}\theta_{im})$. If Eq. (17) is used, the effective parameters remain the same (i.e., $v = v_f$, $D = D_f$, and $\mu = \frac{w_f\theta_f\mu_f + w_{im}\theta_{im}\mu_{im}}{w_f\theta_f}$), except that $R$ becomes $\frac{w_f\theta_f R_f + w_{im}\theta_{im}R_{im}}{w_f\theta_f}$.

## Appendix D. Supplementary materials for Section 4

### D.1. Initial concentration profile for post-contamination simulations at the model agricultural site

We generate the initial PFAS concentration profile for the post-contamination simulations by simulating 30 years of land application of biosolids using the dual-permeability model. The first step is to partition the total infiltration rate ($I_0$) into the fracture and matrix domains such that the two domains are in hydraulic equilibrium under gravity-driven flow. The actual infiltration rates and water contents in the two domains are determined by solving the nonlinear algebraic equation $I_f + I_m = w_f k_{r,f}(\theta_f)K_{sat,f} + w_m k_{r,m}(\theta_m)K_{sat,m} = I_0$ (see Fig. D.1 for the simulated conditions). Second, we determine the parameters for PFAS transport as follows. We assume that mechanical dispersion is dominant (i.e., $v\alpha_L \gg \tau D_0 \approx 0$) in the fracture and mobile matrix domains. Solid-phase and air–water interfacial adsorption are assumed instantaneous (i.e., $F_{eq}^{sw} = F_{eq}^{aw} = 1$). We estimate $A^{aw}$ for the fracture and matrix domains using the thermodynamic method (Eq. (3)) with a roughness scaling factor of 1. The remaining PFAS transport parameters (including PFAS release rate, PFAS molecular weight, fracture–matrix mass-transfer rate constant, dispersivity, solid-phase adsorption coefficient, air–water interfacial adsorption coefficient, and transformation rate constant) are collected from the literature (Guo et al., 2022; Smith et al., 2024; Liu et al., 2021), which we summarize in Table 4. Finally, we use the parameters to solve the PFAS transport equations. This gives the distribution of PFAS across the vadose zone resulting from the 30-year contamination. We generate the initial concentration profiles for both the PFOS and PFOSB simulations. Because the legacy PFOS is modeled in the PFOS simulations, the PFOSB simulations do not consider the release of legacy PFOS from biosolids.

### D.2. Soil water characteristics for the soil in the vadose zone at the model agricultural site

We present in Fig. D.1 the soil water characteristic curves for the soil in the fracture and matrix domain of the vadose zone at the model agricultural site and the simulated water saturation conditions.

**Table C.5**
First and second temporal moments ($m_1$ and $m_2$) of the breakthrough curves at the outlet ($Z = 1$) corresponding to a Dirac delta injection at the inlet ($Z = 0$) for the single-porosity, dual-porosity, and dual-permeability models. For the convenience of mathematical derivations, we assume (1) the adsorption is instantaneous for all three models, (2) the dual-porosity model only contains one immobile matrix domain, and (3) the dual-permeability model has the same Péclet number in the fracture and matrix domains (i.e., $P_m = P_f$).

**Single-porosity model**

$$m_1 \quad R \times \exp\left[\frac{P}{2}\left(1 - g_0^{1/2}\right)\right] g_0^{-1/2\,a}$$

$$m_2 \quad \left(R^2 + \frac{2g_0^{-1/2}}{P}R^2\right) \times \exp\left[\frac{P}{2}\left(1 - g_0^{1/2}\right)\right] g_0^{-1\,a}$$

**Dual-porosity model**

$$m_1 \quad \left[\beta R + (1-\beta)R\frac{\mathrm{Da}_{f,m}^2}{(\theta_{im}\mathcal{U}_{im} + \mathrm{Da}_{f,m})^2}\right] \times \exp\left[\frac{P_f}{2}\left(1 - g_0^{1/2}\right)\right] g_0^{-1/2\,b}$$

$$m_2 \quad \left\{\left[\beta R + (1-\beta)R\frac{\mathrm{Da}_{f,m}^2}{(\theta_{im}\mathcal{U}_{im} + \mathrm{Da}_{f,m})^2}\right]^2 + \frac{2g_0^{-1/2}}{P_f}\left[\beta R + (1-\beta)R\frac{\mathrm{Da}_{f,m}^2}{(\theta_{im}\mathcal{U}_{im} + \mathrm{Da}_{f,m})^2}\right]^2 + g_0^{1/2}(1-\beta)^2R^2\frac{2\gamma\theta_{im}}{1-\gamma}\frac{\mathrm{Da}_{f,m}^2}{(\theta_{im}\mathcal{U}_{im} + \mathrm{Da}_{f,m})^3}\right\} \times \exp\left[\frac{P_f}{2}\left(1 - g_0^{1/2}\right)\right] g_0^{-1\,b}$$

**Dual-permeability model**

$$\begin{aligned}
m_1 \quad & -\left[\frac{2\eta(1-\gamma)\mathrm{Da}_{f,m}(\eta R_f - R_m)}{\theta_m Q_0(-\eta H_{f,0} + H_{m,0} + Q_0)}\right] \times \exp\left[\frac{P_f}{2}\left(1 - g_{1,0}^{1/2}\right)\right] \\
& + \left[1 + \frac{2\eta(1-\gamma)\mathrm{Da}_{f,m}}{\gamma\theta_m(-\eta H_{f,0} + H_{m,0} + Q_0)}\right]\left[\beta R\frac{-\eta H_{f,0} + H_{m,0} + Q_0}{2Q_0} + (1-\beta)R\frac{2\mathrm{Da}_{f,m}^2}{\theta_m^2 Q_0(-\eta H_{f,0} + H_{m,0} + Q_0)}\right] \\
& \times \exp\left[\frac{P_f}{2}\left(1 - g_{1,0}^{1/2}\right)\right] g_{1,0}^{-1/2} \\
& + \left[\frac{2\eta(1-\gamma)\mathrm{Da}_{f,m}(\eta R_f - R_m)}{\theta_m Q_0(\eta H_{f,0} - H_{m,0} + Q_0)}\right] \times \exp\left[\frac{P_f}{2}\left(1 - g_{2,0}^{1/2}\right)\right] \\
& + \left[1 - \frac{2\eta(1-\gamma)\mathrm{Da}_{f,m}}{\gamma\theta_m(\eta H_{f,0} - H_{m,0} + Q_0)}\right]\left[\beta R\frac{\eta H_{f,0} - H_{m,0} + Q_0}{2Q_0} + (1-\beta)R\frac{2\mathrm{Da}_{f,m}^2}{\theta_m^2 Q_0(\eta H_{f,0} - H_{m,0} + Q_0)}\right] \\
& \times \exp\left[\frac{P_f}{2}\left(1 - g_{2,0}^{1/2}\right)\right] g_{2,0}^{-1/2\,c} \\
m_2 \quad & \frac{\bar{v}}{\gamma v_f}\left[\frac{2\eta\gamma(1-\gamma)(\eta R_f - R_m)^2\mathrm{Da}_{f,m}}{\theta_m Q_0^3}\right] \times \exp\left[\frac{P_f}{2}\left(1 - g_{1,0}^{1/2}\right)\right] \\
& - \frac{\bar{v}}{\gamma v_f}\left[\frac{4\eta(1-\gamma)\mathrm{Da}_{f,m}(\eta R_f - R_m)}{\theta_m Q_0(-\eta H_{f,0} + H_{m,0} + Q_0)}\right]\left[\beta R\frac{-\eta H_{f,0} + H_{m,0} + Q_0}{2Q_0} + (1-\beta)R\frac{2\mathrm{Da}_{f,m}^2}{\theta_m^2 Q_0(-\eta H_{f,0} + H_{m,0} + Q_0)}\right] \\
& \times \exp\left[\frac{P_f}{2}\left(1 - g_{1,0}^{1/2}\right)\right] g_{1,0}^{-1/2} \\
& + \frac{\bar{v}}{\gamma v_f}\left\{\left[1 + \frac{2\eta(1-\gamma)\mathrm{Da}_{f,m}}{\gamma\theta_m(-\eta H_{f,0} + H_{m,0} + Q_0)}\right]\left[\beta R\frac{-\eta H_{f,0} + H_{m,0} + Q_0}{2Q_0} + (1-\beta)R\frac{2\mathrm{Da}_{f,m}^2}{\theta_m^2 Q_0(-\eta H_{f,0} + H_{m,0} + Q_0)}\right]^2\right. \\
& + \frac{2g_{1,0}^{-1/2}}{P_f}\left[1 + \frac{2\eta(1-\gamma)\mathrm{Da}_{f,m}}{\gamma\theta_m(-\eta H_{f,0} + H_{m,0} + Q_0)}\right]\left[\beta R\frac{-\eta H_{f,0} + H_{m,0} + Q_0}{2Q_0} + (1-\beta)R\frac{2\mathrm{Da}_{f,m}^2}{\theta_m^2 Q_0(-\eta H_{f,0} + H_{m,0} + Q_0)}\right]^2 \\
& \left. + g_{1,0}^{1/2}\left[1 - \frac{\eta(1-\gamma)\beta}{\gamma(1-\beta)}\right]^2(1-\beta)^2R^2\left[1 + \frac{2\eta\mathrm{Da}_{f,m}}{\theta_m(-\eta H_{f,0} + H_{m,0} + Q_0)}\right]\frac{2\gamma\theta_m\mathrm{Da}_{f,m}^2}{(1-\gamma)(\theta_m Q_0)^3}\right\} \\
& \times \exp\left[\frac{P_f}{2}\left(1 - g_{1,0}^{1/2}\right)\right] g_{1,0}^{-1} \\
& - \frac{\bar{v}}{\gamma v_f}\left[\frac{2\eta\gamma(1-\gamma)(\eta R_f - R_m)^2\mathrm{Da}_{f,m}}{\theta_m Q_0^3}\right] \times \exp\left[\frac{P_f}{2}\left(1 - g_{2,0}^{1/2}\right)\right] \\
& + \frac{\bar{v}}{\gamma v_f}\left[\frac{4\eta(1-\gamma)\mathrm{Da}_{f,m}(\eta R_f - R_m)}{\theta_m Q_0(\eta H_{f,0} - H_{m,0} + Q_0)}\right]\left[\beta R\frac{\eta H_{f,0} - H_{m,0} + Q_0}{2Q_0} + (1-\beta)R\frac{2\mathrm{Da}_{f,m}^2}{\theta_m^2 Q_0(\eta H_{f,0} - H_{m,0} + Q_0)}\right] \\
& \times \exp\left[\frac{P_f}{2}\left(1 - g_{2,0}^{1/2}\right)\right] g_{2,0}^{-1/2} \\
& + \frac{\bar{v}}{\gamma v_f}\left\{\left[1 - \frac{2\eta(1-\gamma)\mathrm{Da}_{f,m}}{\gamma\theta_m(\eta H_{f,0} - H_{m,0} + Q_0)}\right]\left[\beta R\frac{\eta H_{f,0} - H_{m,0} + Q_0}{2Q_0} + (1-\beta)R\frac{2\mathrm{Da}_{f,m}^2}{\theta_m^2 Q_0(\eta H_{f,0} - H_{m,0} + Q_0)}\right]^2\right. \\
& + \frac{2g_{2,0}^{-1/2}}{P_f}\left[1 - \frac{2\eta(1-\gamma)\mathrm{Da}_{f,m}}{\gamma\theta_m(\eta H_{f,0} - H_{m,0} + Q_0)}\right]\left[\beta R\frac{\eta H_{f,0} - H_{m,0} + Q_0}{2Q_0} + (1-\beta)R\frac{2\mathrm{Da}_{f,m}^2}{\theta_m^2 Q_0(\eta H_{f,0} - H_{m,0} + Q_0)}\right]^2 \\
& \left. - g_{2,0}^{1/2}\left[1 - \frac{\eta(1-\gamma)\beta}{\gamma(1-\beta)R}\right]^2(1-\beta)^2R^2\left(1 + \frac{\eta H_{f,0} - H_{m,0} - Q_0}{2\mathrm{Da}_{f,m}}\right)\frac{2\gamma\theta_m\mathrm{Da}_{f,m}^2}{(1-\gamma)(\theta_m Q_0)^3}\right\} \\
& \times \exp\left[\frac{P_f}{2}\left(1 - g_{2,0}^{1/2}\right)\right] g_{2,0}^{-1\,c}
\end{aligned}$$

[a] $R = 1 + K^{sw}\rho/\theta + K^{aw}A^{aw}/\theta$, $g_0 = 1 + 4h_0/P$, $h_0 = \mathcal{U} = \mu L/v$, and $P = vL/D$.

[b] $\gamma = w_f\theta_f/\theta$, $\theta = w_f\theta_f + w_{im}\theta_{im}$, $\bar{v} = \gamma v_f + (1-\gamma)v_{im}$, $\beta = \gamma R_f/R$, $R = \gamma R_f + (1-\gamma)R_{im}$, $g_0 = 1 + 4h_0/P_f$, $h_0 = \mathcal{U}_f + \frac{(1-\gamma)\mathcal{U}_{im}\mathrm{Da}_{f,m}}{\gamma\left(\theta_{im}\mathcal{U}_{im} + \mathrm{Da}_{f,m}\right)}$.

[c] $\eta = v_m/v_f$, $\gamma = w_f\theta_f/\theta$, $\beta = \gamma R_f/R$, $\theta = w_f\theta_f + w_m\theta_m$, $\bar{v} = \gamma v_f + (1-\gamma)v_m$, $R = \gamma R_f + (1-\gamma)R_m$, $H_{f,0} = \mathcal{U}_f + (1-\gamma)\mathrm{Da}_{f,m}/(\gamma\theta_m)$, $H_{m,0} = \mathcal{U}_m + \mathrm{Da}_{f,m}/\theta_m$, $Q_0 = [(\eta H_{f,0} - H_{m,0})^2 + 4\eta(1-\gamma)\mathrm{Da}_{f,m}/(\gamma\theta_m)]^{1/2}$, $g_{1,0} = 1 + \frac{2}{\eta P_f}(\eta H_{f,0} + H_{m,0} - Q_0)$, $g_{2,0} = 1 + \frac{2}{\eta P_f}(\eta H_{f,0} + H_{m,0} + Q_0)$.

### D.3. Mass discharge concentrations for PFAS and their transformation product in the vadose zone at the model agricultural site

Fig. D.2 presents the mass discharge concentrations for PFAS and their transformation product through the vadose zone of the model agricultural site.

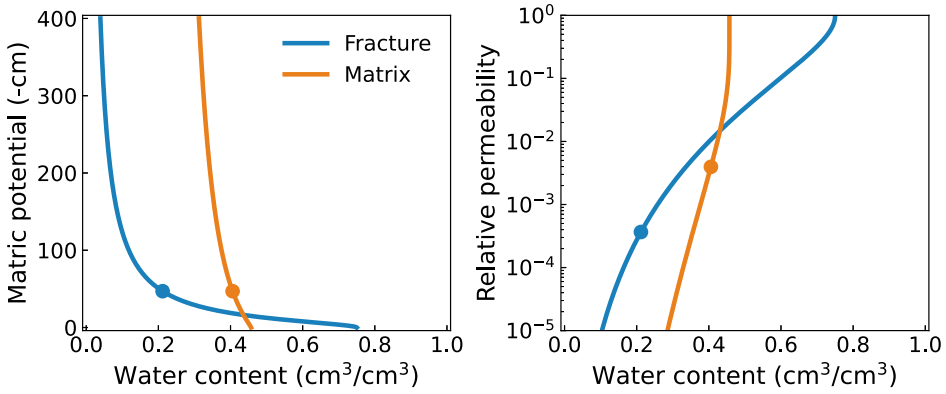


**Fig. D.1.** Soil water characteristic curves and relative permeability curves for soils in the fracture and matrix domains of the vadose zone at the model agricultural site. The dots indicate the water contents and relative permeabilities in the two domains under the simulated condition.

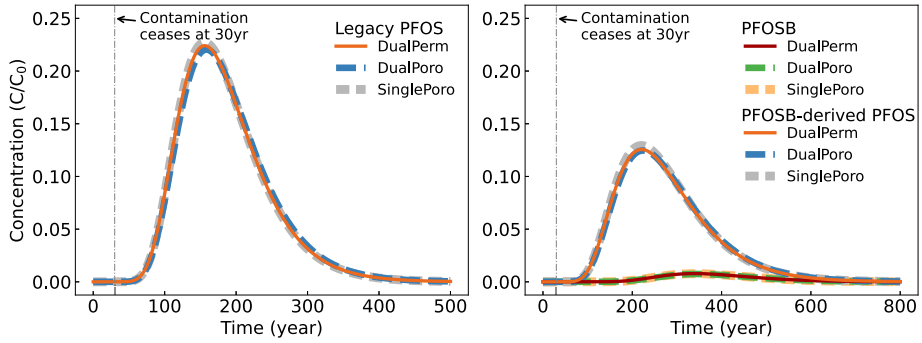


**Fig. D.2.** Mass discharge concentrations for PFAS and their transformation product in the vadose zone at the model agricultural site.

## Data availability

All datasets used in the study have been presented in the manuscript and appendices.

## References


Anderson, R.H., Adamson, D.T., Stroo, H.F., 2019. Partitioning of poly-and perfluoroalkyl substances from soil to groundwater within aqueous film-forming foam source zones. J. Contam. Hydrol. 220, 59–65.

Aris, R., 1958. On the dispersion of linear kinematic waves. Proc. R. Soc. Lond. Ser. A. Math. Phys. Sci. 245 (1241), 268–277.

Bai, M., Elsworth, D., Roegiers, J.C., 1993. Multiporosity/multipermeability approach to the simulation of naturally fractured reservoirs. Water Resour. Res. 29 (6), 1621–1633.

Barenblatt, G.I., Zheltov, I.P., Kochina, I., 1960. Basic concepts in the theory of seepage of homogeneous liquids in fissured rocks [strata]. J. Appl. Math. Mech. 24 (5), 1286–1303.

Beven, K., Germann, P., 1982. Macropores and water flow in soils. Water Resour. Res. 18 (5), 1311–1325.

Bradford, S.A., Leij, F.J., 1997. Estimating interfacial areas for multi-fluid soil systems. J. Contam. Hydrol. 27 (1–2), 83–105.

Brusseau, M.L., 2020. Simulating PFAS transport influenced by rate-limited multi-process retention. Water Res. 168, 115179.

Brusseau, M.L., 2023a. Determining air–water interfacial areas for the retention and transport of PFAS and other interfacially active solutes in unsaturated porous media. Sci. Total Environ. 163730.

Brusseau, M.L., 2023b. Differential sorption of short-chain versus long-chain anionic per-and poly-fluoroalkyl substances by soils. Environments 10 (10), 175.

Brusseau, M.L., Anderson, R.H., Guo, B., 2020. PFAS concentrations in soils: Background levels versus contaminated sites. Sci. Total Environ. 740, 140017.

Brusseau, M.L., El Ouni, A., Araujo, J.B., Zhong, H., 2015. Novel methods for measuring air–water interfacial area in unsaturated porous media. Chemosphere 127, 208–213.

Brusseau, M.L., Guo, B., 2024. Vapor-phase transport of per and polyfluoroalkyl substances: Processes, modeling, and implications. Sci. Total Environ. 947, 174644.

Brusseau, M.L., Khan, N., Wang, Y., Yan, N., Van Glubt, S., Carroll, K.C., 2019. Nonideal transport and extended elution tailing of PFOS in soil. Environ. Sci. Technol. 53 (18), 10654–10664.

Brusseau, M.L., Peng, S., Schnaar, G., Murao, A., 2007. Measuring air- water interfacial areas with x-ray microtomography and interfacial partitioning tracer tests. Environ. Sci. Technol. 41 (6), 1956–1961.

Brusseau, M.L., Van Glubt, S., 2021. The influence of molecular structure on PFAS adsorption at air-water interfaces in electrolyte solutions. Chemosphere 281, 130829.

Chen, S., Guo, B., 2023. Pore-scale modeling of PFAS transport in water-unsaturated porous media: Air–water interfacial adsorption and mass-transfer processes in thin water films. Water Resour. Res. 59 (8), e2023WR034664.

Chen, J.S., Ho, Y.C., Liang, C.P., Wang, S.W., Liu, C.W., 2019. Semi-analytical model for coupled multispecies advective-dispersive transport subject to rate-limited sorption. J. Hydrol. 579, 124164.

Chen, L., Kibbey, T.C., 2006. Measurement of air-water interfacial area for multiple hysteretic drainage curves in an unsaturated fine sand. Langmuir 22 (16), 6874–6880.

Chen, W., Wagenet, R.J., 1995. Solute transport in porous media with sorption-site heterogeneity. Environ. Sci. Technol. 29 (11), 2725–2734.

Chen, W., Wagenet, R., 1997. Description of atrazine transport in soil with heterogeneous nonequilibrium sorption. Soil Sci. Am. J. 61 (2), 360–371.

Choi, Y.J., Helbling, D.E., Liu, J., Olivares, C.I., Higgins, C.P., 2022. Microbial biotransformation of aqueous film-forming foam derived polyfluoroalkyl substances. Sci. Total Environ. 824, 153711.

Clay, D., Stott, K., 1973. The persistence and penetration of large doses of simazine in uncropped soil. Weed Res. 13 (1), 42–50.

Costanza, J., Arshadi, M., Abriola, L.M., Pennell, K.D., 2019. Accumulation of PFOA and PFOS at the air–water interface. Environ. Sci. Technol. Lett. 6 (8), 487–491.

Crump, K.S., 1976. Numerical inversion of Laplace transforms using a Fourier series approximation. J. ACM 23 (1), 89–96.

Culligan, K.A., Wildenschild, D., Christensen, B.S., Gray, W.G., Rivers, M.L., Tompson, A.F., 2004. Interfacial area measurements for unsaturated flow through a porous medium. Water Resour. Res. 40 (12).

Culver, T.B., Hallisey, S.P., Sahoo, D., Deitsch, J.J., Smith, J.A., 1997. Modeling the desorption of organic contaminants from long-term contaminated soil using distributed mass transfer rates. Environ. Sci. Technol. 31 (6), 1581–1588.

De Hoog, F.R., Knight, J., Stokes, A., 1982. An improved method for numerical inversion of Laplace transforms. SIAM J. Sci. Stat. Comput. 3 (3), 357–366.

Dong, S., Yan, P.F., Liu, C., Manz, K.E., Mezzari, M.P., Abriola, L.M., Pennell, K.D., Cápiro, N.L., 2023. Assessing aerobic biotransformation of 8: 2 fluorotelomer alcohol in aqueous film-forming foam (AFFF)-impacted soils: Pathways and microbial community dynamics. J. Hazard. Mater. 446, 130629.

Du, P., Barrio, R., Jiang, H., Cheng, L., 2017. Accurate quotient-difference algorithm: error analysis, improvements and applications. Appl. Math. Comput. 309, 245–271.

Durbin, F., 1974. Numerical inversion of Laplace transforms: an efficient improvement to dubner and abate's method. Comput. J. 17 (4), 371–376.

Flury, M., 1996. Experimental evidence of transport of pesticides through field soils—a review. J. Environ. Qual. 25 (1), 25–45.

Flury, M., Flühler, H., Jury, W.A., Leuenberger, J., 1994. Susceptibility of soils to preferential flow of water: A field study. Water Resour. Res. 30 (7), 1945–1954.

Gärdenäs, A.I., Šimůnek, J., Jarvis, N., van Genuchten, M.T., 2006. Two-dimensional modelling of preferential water flow and pesticide transport from a tile-drained field. J. Hydrol. 329 (3–4), 647–660.

van Genuchten, M.T., 1980. A closed-form equation for predicting the hydraulic conductivity of unsaturated soils. Soil Sci. Am. J. 44 (5), 892–898.

van Genuchten, M.T., Wierenga, P., 1976. Mass transfer studies in sorbing porous media I. Analytical solutions. Soil Sci. Am. J. 40 (4), 473–480.

van Genuchten, M.T., Wierenga, P., 1977. Mass transfer studies in sorbing porous media: II. Experimental evaluation with tritium (3H2O). Soil Sci. Am. J. 41 (2), 272–278.

Gerke, H.H., van Genuchten, M.T., 1993. A dual-porosity model for simulating the preferential movement of water and solutes in structured porous media. Water Resour. Res. 29 (2), 305–319.

Guo, B., Zeng, J., Brusseau, M.L., 2020. A mathematical model for the release, transport, and retention of per-and polyfluoroalkyl substances (PFAS) in the vadose zone. Water Resour. Res. 56 (2), e2019WR026667.

Guo, B., Zeng, J., Brusseau, M.L., Zhang, Y., 2022. A screening model for quantifying PFAS leaching in the vadose zone and mass discharge to groundwater. Adv. Water Resour. 160, 104102.

Higgins, C.P., Luthy, R.G., 2006. Sorption of perfluorinated surfactants on sediments. Environ. Sci. Technol. 40 (23), 7251–7256.

Hitzelberger, M., Khan, N.A., Mohamed, R.A., Brusseau, M.L., Carroll, K.C., 2022. PFOS mass flux reduction/mass removal: Impacts of a lower-permeability sand lens within otherwise homogeneous systems. Environ. Sci. Technol. 56 (19), 13675–13685.

Ho, Y.C., Suk, H., Liang, C.P., Liu, C.W., Nguyen, T.U., Chen, J.S., 2024. Recursive analytical solution for nonequilibrium multispecies transport of decaying contaminant simultaneously coupled in both the dissolved and sorbed phases. Adv. Water Resour. 192, 104777.

Honig, G., Hirdes, U., 1984. A method for the numerical inversion of Laplace transforms. J. Comput. Appl. Math. 10 (1), 113–132.

Jiang, H., Guo, B., Brusseau, M.L., 2020a. Pore-scale modeling of fluid-fluid interfacial area in variably saturated porous media containing microscale surface roughness. Water Resour. Res. 56 (1), e2019WR025876.

Jiang, H., Guo, B., Brusseau, M.L., 2020b. Characterization of the micro-scale surface roughness effect on immiscible fluids and interfacial areas in porous media using the measurements of interfacial partitioning tracer tests. Adv. Water Resour. 146, 103789.

Jury, W.A., Horton, R., 2004. Soil Physics. John Wiley & Sons.

Leij, F.J., Toride, N., Field, M.S., Sciortino, A., 2012. Solute transport in dual-permeability porous media. Water Resour. Res. 48 (4).

Leverett, M., 1941. Capillary behavior in porous solids. Trans. AIME 142 (01), 152–169.

Li, Z., Brusseau, M.L., 2000. Nonideal transport of reactive solutes in heterogeneous porous media: 6. Microscopic and macroscopic approaches for incorporating heterogeneous rate-limited mass transfer. Water Resour. Res. 36 (10), 2853–2867.

Lindstorm, F., Narasimham, M., 1973. Mathematical theory of a kinetic model for dispersion of previously distributed chemicals in a sorbing porous medium. SIAM J. Appl. Math. 24 (4), 496–510.

Liu, H., Guo, Z., Zhu, Y., Van Glubt, S., Brusseau, M.L., 2024. The influence of NAPL distribution on the transport of PFOS in co-contaminated media. J. Hazard. Mater. 462, 132794.

Liu, M., Munoz, G., Vo Duy, S., Sauvé, S., Liu, J., 2021. Stability of nitrogen-containing polyfluoroalkyl substances in aerobic soils. Environ. Sci. Technol. 55 (8), 4698–4708.

Lyu, Y., Brusseau, M.L., Chen, W., Yan, N., Fu, X., Lin, X., 2018. Adsorption of PFOA at the air–water interface during transport in unsaturated porous media. Environ. Sci. Technol. 52 (14), 7745–7753.

Ma, M., Smith, J., Brusseau, M.L., Guo, B., 2025. User Guide: Excel Tool for Tiers 3 and 4 models of PFAS-LEACH (PFAS-LEACH-Analytical and PFAS-LEACH-DAF). Technical Report, University of Arizona. Tucson, Arizona., https://github.com/GuoSFPLab/PFAS-LEACH-Tier-3-4.

Millington, R., Quirk, J., 1961. Permeability of porous solids. Trans. Faraday Soc. 57, 1200–1207.

Morrow, N.R., 1970. Physics and thermodynamics of capillary action in porous media. Ind. Eng. Chem. 62 (6), 32–56.

Mualem, Y., 1976. A new model for predicting the hydraulic conductivity of unsaturated porous media. Water Resour. Res. 12 (3), 513–522.

Nguyen, T.U., Ho, Y.C., Suk, H., Liang, C.P., Liao, Z.Y., Chen, J.S., 2024. Semi-analytical models for two-dimensional multispecies transport of sequentially degradation products influenced by rate-limited sorption subject to arbitrary time-dependent inlet boundary conditions. Adv. Water Resour. 184, 104612.

Oostrom, M., White, M.D., Brusseau, M., 2001. Theoretical estimation of free and entrapped nonwetting–wetting fluid interfacial areas in porous media. Adv. Water Resour. 24 (8), 887–898.

Pot, V., Šimůnek, J., Benoit, P., Coquet, Y., Yra, A., Martínez-Cordón, M.J., 2005. Impact of rainfall intensity on the transport of two herbicides in undisturbed grassed filter strip soil cores. J. Contam. Hydrol. 81 (1–4), 63–88.

Rao, P.S., Green, R.E., Balasubramanian, V., Kanehiro, Y., 1974. Field Study of Solute Movement in a Highly Aggregated Oxisol with Intermittent Flooding: II. Picloram. Technical Report, Wiley Online Library.

Reeves, P.C., Celia, M.A., 1996. A functional relationship between capillary pressure, saturation, and interfacial area as revealed by a pore-scale network model. Water Resour. Res. 32 (8), 2345–2358.

Russo, D., Fiori, A., 2008. Equivalent vadose zone steady state flow: An assessment of its capability to predict transport in a realistic combined vadose zone–groundwater flow system. Water Resour. Res. 44 (9).

Schaefer, C., DiCarlo, D., Blunt, M., 2000. Experimental measurement of air-water interfacial area during gravity drainage and secondary imbibition in porous media. Water Resour. Res. 36 (4), 885–890.

Sharma, A., Swami, D., Joshi, N., Chandel, A., Šimůnek, J., 2021. The semi-analytical solution for non-equilibrium solute transport in dual-permeability porous media. Water Resour. Res. 57 (5), e2020WR029370.

Silva, J.A.K., Šimůnek, J., McCray, J.E., 2020. A modified HYDRUS model for simulating PFAS transport in the vadose zone. Water 12 (10), 2758.

Silva, J.A., Šimůnek, J., McCray, J.E., 2022. Comparison of methods to estimate air-water interfacial areas for evaluating PFAS transport in the vadose zone. J. Contam. Hydrol. 247, 103984.

Skopp, J., Gardner, W.R., Tyler, E.J., 1981. Solute movement in structured soils: Two-region model with small interaction. Soil Sci. Am. J. 45 (5), 837–842.

Smith, J., Brusseau, M.L., Guo, B., 2024. An integrated analytical modeling framework for determining site-specific soil screening levels for PFAS. Water Res. 252, 121236.

Stults, J.F., Higgins, C.P., Illangasekare, T.H., Singha, K., 2024a. Non-fickian transport processes accelerate the movement of PFOS in unsaturated media: An experimental and modelling study. J. Contam. Hydrol. 267, 104424.

Stults, J.F., Schaefer, C.E., Fang, Y., Devon, J., Nguyen, D., Real, I., Hao, S., Guelfo, J.L., 2024b. Air-water interfacial collapse and rate-limited solid desorption control perfluoroalkyl acid leaching from the vadose zone. J. Contam. Hydrol. 265, 104382.

Toride, N., Leij, F.J., van Genuchten, M.T., 1993. A comprehensive set of analytical solutions for nonequilibrium solute transport with first-order decay and zero-order production. Water Resour. Res. 29 (7), 2167–2182.

Šimůnek, J., van Genuchten, M.T., 2008. Modeling nonequilibrium flow and transport processes using HYDRUS. Vadose Zone J. 7 (2), 782–797.

Valocchi, A.J., 1985. Validity of the local equilibrium assumption for modeling sorbing solute transport through homogeneous soils. Water Resour. Res. 21 (6), 808–820.

Van Glubt, S., Brusseau, M.L., Yan, N., Huang, D., Khan, N., Carroll, K.C., 2021. Column versus batch methods for measuring PFOS and PFOA sorption to geomedia. Environ. Pollut. 268, 115917.

Wallis, I., Hutson, J., Davis, G., Kookana, R., Rayner, J., Prommer, H., 2022. Model-based identification of vadose zone controls on PFAS mobility under semi-arid climate conditions. Water Res. 225, 119096.

Warren, J.E., Root, P.J., 1963. The behavior of naturally fractured reservoirs. Soc. Pet. Eng. J. 3 (03), 245–255.

Wei, C., Song, X., Wang, Q., Hu, Z., 2017. Sorption kinetics, isotherms and mechanisms of PFOS on soils with different physicochemical properties. Ecotoxicol. Environ. Safety 142, 40–50.

Zeng, J., Brusseau, M.L., Guo, B., 2021. Model validation and analyses of parameter sensitivity and uncertainty for modeling long-term retention and leaching of PFAS in the vadose zone. J. Hydrol. 603, 127172.

Zeng, J., Guo, B., 2021. Multidimensional simulation of PFAS transport and leaching in the vadose zone: Impact of surfactant-induced flow and subsurface heterogeneities. Adv. Water Resour. 155, 104015.

Zeng, J., Guo, B., 2023. Reduced accessible air–water interfacial area accelerates PFAS leaching in heterogeneous vadose zones. Geophys. Res. Lett. 50 (8), e2022GL102655.